EXCELENCIA
MARÍA
DE MAEZTU

IFISC

Universitat de les Illes Balears

CSIC

PROCEEDINGS OF THE 2024 SURF@IFISC FELLOWSHIPS

Proceedings of the 2024 SURF@IFISC Fellowships

The SURF (Summer Undergraduate Research Fellowships) Program is offered by IFISC since 2013 (only interrupted in 2020 due to the Covid-19 pandemic) with the goal of attracting excellent undergraduate students with majors compatible with IFISC research lines and offers Summer internships at IFISC, typically during the month of July, advised by members of IFISC Claustro.

SURF attracted for the Summer of 2024 a total of 37 candidates (28 male and 9 female), out of which 6 candidates were selected, 4 of them male and 2 female candidates. The candidates came from 20 different universities belonging to 7 different countries, while the candidates were citizens of 6 different countries. The universities with more candidates were the University of Valencia with 6 applicants. and the U. of Barcelona with 5 applicants. More than half of the applicants, 25, were Spanish citizens, and in second place comes China with 6 applicants.

These are the proceedings:

1. Irene López Larios (Supervisor: Tobias Galla), *A modified random generalised Lotka-Volterra model*
2. Adam César Maćkowiak Pellón, Massimiliano Zanin, *Using Deep Learning to outperform network science*
3. Sergio Arias Rangel, Rosa López, Mykhailo Moskalets, *Maxwell's demon at the nanoscale: Seebeck effects*
4. Agostina Iozzi Acosta, María Martínez-Barbeito, Pere Colet, *Power grid stability in scenarios of large VRES penetration*
5. Ernest Staffetti Cruañas, Gianluca Giorgi, Ricard Ravell, *Entanglement classification with quantum reservoir computing*
6. Andreu Fiol, Damià Gomila, Daniel Ruiz-Reynés, *Spatiotemporal Dynamics: Applications to vegetation population dynamics*

A modified random generalised Lotka-Volterra model

Student: Irene López Larios
Tutor: Tobias Galla
Instituto de Física Interdisciplinar y Sistemas Complejos, IFISC (CSIC-UIB)
Campus Universitat de les Illes Balears, E-07122 Palma de Mallorca, Spain

Abstract

In this project, a modified version of the well-known random generalised Lotka-Volterra (rGLV) model is studied. The rGLV model is revised and then modified by defining a threshold in population density below which the species are considered to become extinct. Our aim is to study the modified model both analytically and numerically. A new closed-form solution for the order parameter equations, analogous to that of the rGLV model, has been successfully imported to the modified model. Several numerical experiments have been carried out so as to assess the claim that the modifed rGLV model is more stable than the original one.

1 Introduction

In this work we are interested in studying a modified version of the generalised Lotka-Volterra model, usually employed in population dynamics to describe biodiversity and ecological communities. In the original rGLV model, it is possible for the population density of any of the coexisting species to take extremely low values and then grow again until taking rather unlikely high values. In order to prevent these unrealistic scenarios predicted by the original rGLV model, the following modification is considered.

A threshold is defined so that species whose population density goes below that critical threshold are automatically considered to become extinct. Not only might the study of this modified rGLV model help us prevent such undesired scenarios, but it also might provide relevant information about how ecosystems behave under constraints in the population density of the coexisting species.

The project's main goal has been understanding the existing analytical and numerical results for the original rGLV model (see [1]), as well as extending and adapting those results for the modified version of the rGLV model. Accordingly, Section 2.1 is devoted to revising the main theoretical results for the original rGLV model. In Section 2.2, analogous theoretical results are studied for the modified rGLV model. In Section 3, the results of several numerical experiments are discussed and compared against the analytical predictions derived in the previous Section 2.2.

2 Theoretical model

2.1 Random generalised Lotka-Volterra model

Governing equations

We consider a system of N coexisting species, indexed by $i = 1, ..., N$. The population density of species i is denoted by x_i and evolves continuously in time according to the Generalised Lotka-Volterra equations, which are given by the following set of coupled ordinary differential equations

$$\dot{x}_i = x_i\left(1 - x_i + \sum_{j\neq i} \alpha_{ij} x_i\right), \tag{2.1}$$

where $i = 1, 2, \ldots, N$ and the coefficients α_{ij} describe the interactions between the species, representing the influence that species j has on species i. Negative values of α_{ij} imply that the presence of species j is detrimental for species i. If α_{ij} and α_{ji} have opposite signs, the pair of species i and j constitutes a prey-predator pair. Self-interaction coefficients of the form α_{ii} have been set equal to $\alpha_{ii} = -1$, so that the existence of species i suppresses its own growth in population density.

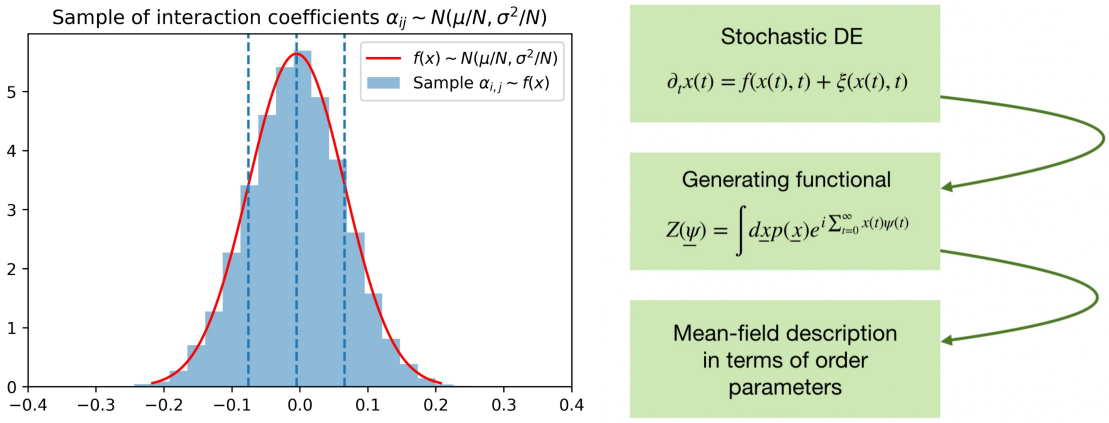

Figure 1: The random sampling approach used in the rGLV model captures the inherent uncertainty and natural variability of ecological systems. Sample of off-diagonal interaction coefficients for parameters $\mu = 0.1$, $\sigma^2 = 5$, $\Gamma = -0.5$ and $N = 10$ (left). Outline of the formalism used to analytically study the rGLV model (right).

The diagonally opposed interaction coefficients α_{ij} are chosen randomly from a random distribution at the beginning, and remain fixed along the dynamics. The random distribution considered is a Gaussian distribution with the following mean, variance and correlation

$$\begin{aligned} \overline{\alpha_{ij}} &= \frac{\mu}{N}, \\ \overline{\alpha_{ij}^2} - \frac{\mu^2}{N^2} &= \frac{\sigma^2}{N}, \\ \overline{\alpha_{ij}\alpha_{ji}} - \frac{\mu^2}{N^2} &= \Gamma\frac{\sigma^2}{N}, \end{aligned} \tag{2.2}$$

where the over-line denotes the average value. The parameter μ is called the *co-operation parameter* and it models the strength in the interactions between species. Negative values of μ imply competition between species, and tend to stabilise the ecosystem. The parameter σ^2 is the variance of the interactions and controls the diversity of the interactions. The parameter Γ is called the *symmetry parameter* and it modulates the correlation between the off-diagonal interaction coefficients, ranging between $-1 \leq \Gamma \leq 1$. When it comes to numerical experiment, the off-diagonal interaction coefficients are generated, for each pair $i < j$, as follows

1. Two independent random Gaussian variables u and v are generated, each with mean zero and variance one $u, v \sim N(0, 1)$. The variables u and v for one pair (i, j) are independent from those of any other pair.
2. The diagonally opposed coefficients are chosen to be

$$\begin{aligned} \alpha_{ij} &= \frac{\mu}{N} + \frac{\sigma}{\sqrt{N}}u, \\ \alpha_{ji} &= \frac{\mu}{N} + \frac{\sigma}{\sqrt{N}}\left(\Gamma u + \sqrt{1-\Gamma^2}v\right). \end{aligned}$$

It is straightforward to check that the coefficients resulting from this construction have the desired mean, variance and correlation indicated in (2.2), since

$$\overline{\left(\alpha_{ij} - \frac{\mu}{N}\right)^2} = \frac{\sigma^2}{N}\left[\Gamma^2 \underbrace{\overline{u^2}}_{=1} + (1-\Gamma^2)\underbrace{\overline{v^2}}_{=1} + \Gamma\sqrt{1-\Gamma^2}\underbrace{\overline{uv}}_{=0}\right] = \frac{\sigma^2}{N}.$$

Fixed point ansatz and order parameter equations

The rGLV model can be characterised following an analytical approach. Such an approach is beyond the scope of our project, so in this section we only include a brief and shallow discussion of it and focus on the final results that it entails. The final theoretical results, whose derivation is widely discussed in [1], will be compared against numerical experiment.

The analytical approach that can be used to study the rGLV model is based on the Martin-Siggia-Rose (MSR) formalism, as well as dynamic mean-field theory. The MSR formalism is a generating-functional method to derive a dynamic mean-field description for a system of stochastic differential equations (SDEs). This formalism is formulated via path integrals. The goal is to find a mean-field description that captures the typical behaviour of the model.

In order to do that, a perturbation field is added to the Lotka-Volterra equations (2.1) to generate dynamical response functions. Then, a moment generating functional is defined over all possible trajectories of the Lotka-Volterra dynamics. After averaging over all possible realizations and taking the thermodynamic limit, an effective process is obtained showing what a typical representative species experiences. In turn, the effective process allows one to obtain the order parameters that account for the dynamics of the model (Figure 1).

It is then assumed that the system reaches a stationary state and that this stationary state does not depend on the initial condition. It is further assumed that the dynamics reaches a fixed point. In the original system this means that all x_i tend to fixed-point values x_i^* at long times. Under these stronger assumptions (*fixed-point ansatz*), the dynamical mean-field description can be further simplified to

$$x(z) = \max\left\{0, \frac{1+\mu M^* + \sqrt{q}\sigma z + h}{1-\Gamma\sigma^2\chi}\right\}. \tag{2.3}$$

It should be noted that only $x \geq 0$ is physically meaningful. In the final simplified description of population density (2.3), three new parameters M^*, χ and q have been introduced. These are the so-called *order parameters* and they are related to the successive moments of x, according to the following definitions

$$M^* := \langle x(z)\rangle_*\big|_{h=0}, \tag{2.4}$$

$$q := \langle x(z)^2\rangle_*\big|_{h=0}, \tag{2.5}$$

$$\chi := \frac{d}{dh}\Big(\langle x(z)\rangle_*\Big)\Big|_{h=0}. \tag{2.6}$$

Thus, M^* is the average species concentration and χ is the dynamic susceptibility, which measures the dynamic response of the system to perturbations. Finally, z is a static Gaussian random variable of mean zero and unit variance. This *ansatz* implies that a fraction of the N initial species dies out during the Lotka-Volterra dynamics. The fraction of surviving species will be denoted ϕ and is given by

$$\phi := \int_{-\infty}^{\Delta} Dz, \tag{2.7}$$

where $Dz := \frac{e^{-z^2/2}}{\sqrt{2\pi}}dz$. By means of substituting equation (2.3) into definitions (2.4)-(2.6), one can obtain the following *order parameter equations*

$$M^* = \frac{\sqrt{q}\sigma}{1-\Gamma\sigma^2\chi}\int_{-\Delta}^{+\infty}(\Delta+z)Dz, \tag{2.8}$$

$$1 = \frac{\sigma^2}{(1-\Gamma\sigma^2\chi)^2}\int_{-\Delta}^{+\infty}(\Delta+z)^2Dz, \tag{2.9}$$

$$\chi = \frac{1}{1-\Gamma\sigma^2\chi}\int_{-\Delta}^{+\infty}Dz, \tag{2.10}$$

$$\Delta = \frac{1+\mu M^*}{\sqrt{q}\sigma}. \tag{2.11}$$

It is worth noting that the integrals in the parameter equations only depend on Δ and can be computed in terms of the error function. It is convenient to define the following functions of Δ

$$w_0(\Delta) := \int_{-\Delta}^{+\infty}Dz = \frac{1}{2}\left[1+\mathrm{erf}\left(\frac{\Delta}{\sqrt{2}}\right)\right], \tag{2.12}$$

$$w_1(\Delta) := \int_{-\Delta}^{+\infty}(\Delta+z)Dz = \frac{1}{2}\left[e^{-\Delta^2/2}\sqrt{\frac{2}{\pi}} + \Delta\left(1+\mathrm{erf}\left(\frac{\Delta}{\sqrt{2}}\right)\right)\right], \tag{2.13}$$

$$w_2(\Delta) := \int_{-\Delta}^{+\infty}(\Delta+z)^2Dz = w_0 + \Delta w_1. \tag{2.14}$$

We can rewrite the order parameter equations (2.8)-(2.11) in a more compact form using the new notation (2.12)-(2.14) as follows

$$M^* = \frac{\sqrt{q}\sigma}{1-\Gamma\sigma^2\chi} w_1(\Delta), \tag{2.15}$$

$$1 = \frac{\sigma^2}{(1-\Gamma\sigma^2\chi)^2} w_2(\Delta), \tag{2.16}$$

$$\chi = \frac{1}{1-\Gamma\sigma^2\chi} w_0(\Delta), \tag{2.17}$$

$$\Delta = \frac{1+\mu M^*}{\sqrt{q}\sigma}. \tag{2.18}$$

Henceforth, the functional dependence on Δ of the functions defined in equations (2.14)-(2.16) will be omitted. In the next subsection, a closed-form solution of the system of order parameter equations (2.15)-(2.18) is described, so that the three order parameters of interest M^*, χ and q can be obtained.

Closed-form solution of the order parameter equations

The parameter equations (2.15)-(2.18) can be solved parametrically. This set of equations can be thought of as a system of 4 equations with 4 unknowns, namely M^*, q, σ^2 and χ. The remaining quantities μ and Γ are known constants that are already fixed for the system. Lastly, Δ is the solution parameter, so it can be seen as known quantity.

What we mean when we say that this system of equations can be solved parametrically is that all 4 unknowns can be rewritten only as a function of a certain parameter Δ i.e. one can arrive at a parametric solution of the form $M^* = M^*(\Delta)$, $q = q(\Delta)$, $\sigma^2 = \sigma^2(\Delta)$ and $\chi = \chi(\Delta)$. Each time the parametric solution is evaluated at a certain Δ value, all unknowns can be calculated for a different rGLV system as follows

1. Values for μ and Γ are fixed.
2. One Δ value is substituted into the parametric solution $M^* = M^*(\Delta)$, $q = q(\Delta)$, $\sigma^2 = \sigma^2(\Delta)$ and $\chi = \chi(\Delta)$. Thus, values for all 4 unknowns of the system M^*, q, σ^2 and χ are obtained.
3. A complete description of the order parameters M^*, q and χ is obtained for the system whose defining properties are given by μ, Γ and σ^2.

Numerical evaluation shows that the substitution of Δ values between $-10 \leq \Delta \leq 10$ into the parametric solution $M^* = M^*(\Delta), q = q(\Delta), \sigma^2 = \sigma^2(\Delta)$ and $\chi = \chi(\Delta)$, is enough to retrieve the order parameters of a wide range of systems with different properties μ, Γ and σ^2. We include the detailed procedure to solve the system parametrically now, since the generalised procedure in Section 2.2 will be analogous.

We will solve for the 4 unknowns M^*, q, σ^2 and χ in terms of the parameter Δ. We start by using equation (2.16) along with the square of (2.17) divided by (2.16), that is

$$\begin{cases} 1 = \frac{\sigma^2 w_2}{(1-\Gamma\sigma^2\chi)^2} \\ \chi^2 = \frac{w_0^2}{(1-\Gamma\sigma^2\chi)^2} \frac{(1-\Gamma\sigma^2\chi)^2}{\sigma^2 w_2} \end{cases} \Leftrightarrow \begin{cases} \sigma^2\chi^2 = \frac{w_0^2}{w_2} \\ \chi - \Gamma\sigma^2\chi^2 = w_0 \end{cases} \Leftrightarrow \begin{cases} \chi = w_0 + \Gamma\frac{w_0^2}{w_2} \\ \sigma^2 = \frac{w_2}{(w_2+\Gamma w_0)^2} \end{cases}.$$

This gives us χ and σ^2 as a function of Δ. It only remains to study the unknowns M^* and q. Since we already know χ and σ^2 as a function of Δ, it will be enough to rewrite M^* and q in terms of Δ, χ or σ^2. On the one hand, equation (2.15) yields q as a function of known quantities and M^*

$$M^* = \frac{\sqrt{q}\sigma w_1}{1-\Gamma\sigma^2\chi} \quad \Leftrightarrow \quad q\sigma^2 = \frac{(1-\Gamma\sigma^2\chi)^2 M^{*2}}{w_1^2} \quad \Leftrightarrow \quad q = \left(\frac{(1-\Gamma\sigma^2\chi)M^*}{\sigma w_1}\right)^2.$$

If we find M^* as a function of known quantities, we will have solved the system. Combining equations (2.18) and (2.15) gives us the desired result

$$\Delta = \frac{1+\mu M^*}{\sqrt{q}\sigma} = \frac{1+\mu M^*}{(1-\Gamma\sigma^2\chi)M^*} w_1 \quad \Leftrightarrow \quad \frac{\Delta}{w_1} = \frac{1}{(1-\Gamma\sigma^2\chi)M^*} + \frac{\mu}{1-\Gamma\sigma^2\chi}$$

$$\frac{1}{M^*} = \frac{\Delta(1-\Gamma\sigma^2\chi)}{w_1} - \mu$$

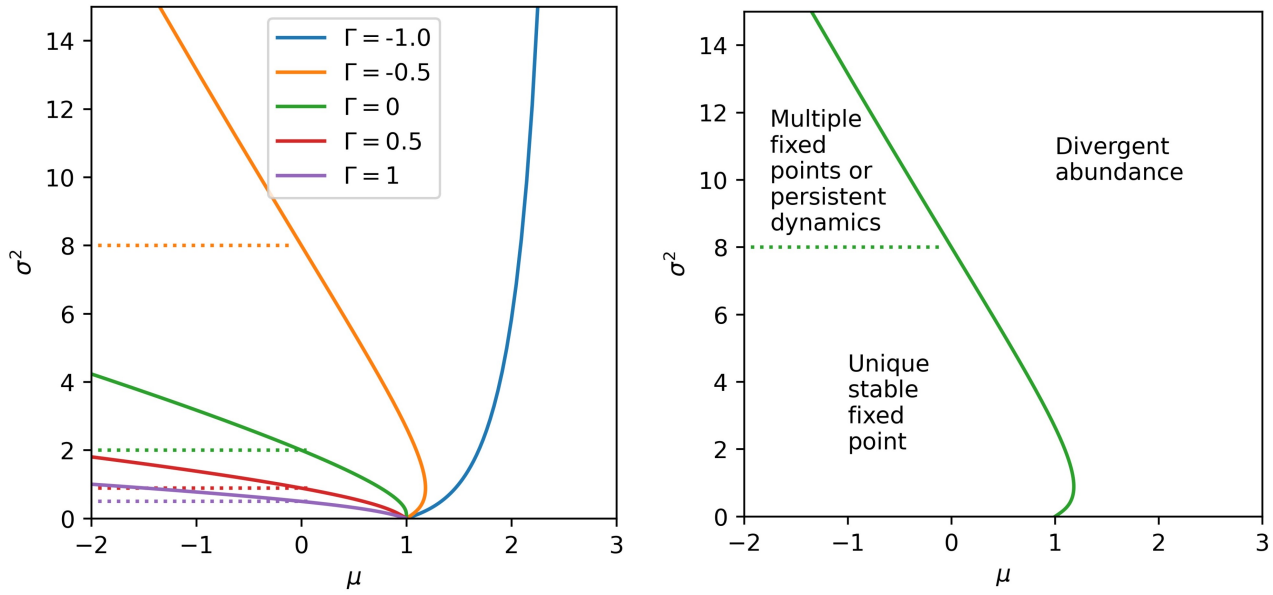

Figure 2: Stability diagrams for the rGLV model in the (μ, σ^2) plane. Lines mark the onset of diverging abundances, dashed lines are the onset of linear instability. The fixed-point equations are not valid in this part of the phase diagram. On the left, the phase diagram for different values of correlation Γ. On the right, we fix $\Gamma = -0.5$ [1].

To sum up, the parametric solution of equations (2.15)-(2.18) is given in terms of the parameter Δ by the following relations

$$\chi = w_0 + \Gamma \frac{w_0^2}{w_2}, \tag{2.19}$$

$$\sigma^2 = \frac{w_2}{(w_2 + \Gamma w_0)^2}, \tag{2.20}$$

$$\frac{1}{M^*} = \frac{\Delta(1 - \Gamma\sigma^2\chi)}{w_1} - \mu, \tag{2.21}$$

$$q = \left(\frac{(1 - \Gamma\sigma^2\chi)M^*}{\sigma w_1}\right)^2. \tag{2.22}$$

Stability analysis

For a given value of Γ, the rGLV model shows two different types of instability in the (μ, σ^2) plane, as depicted in Figure 2. The values for the critical points in the plane can be predicted by the theoretical model, as follows

- **Instability due to divergent abundances**. The onset of divergent abundances is signalled by a divergent mean abundance M^*. Setting $1/M^* = 0$ in equations (2.21) and (2.20) we find that this occurs when

$$(\mu, \sigma^2) = \left(\frac{\Delta}{w_1}\frac{w_2}{w_2 + \Gamma w_0}, \frac{w_2}{(w_2 + \Gamma w_0)^2}\right).$$

  For a fixed value of Γ, the above equation provides a parametric description of a line in the (μ, σ^2) plane in terms of the parameter Δ.

- **Linear instability**. The Lotka–Volterra system also shows a linear instability, which can be predicted via the formalism briefly described in Section 2.1. It can be proved (see [1]) that the linear instability is signalled by the condition $\phi\sigma^2 = (1 - \Gamma\sigma^2\chi)^2$, which leads to $\Delta = 0$ and $\phi = 1/2$ when substituted into (2.8). If these values are again substituted into (2.9) and (2.10), a system of two equations and two unknowns χ and σ^2 is obtained. The solution yields the critical constant value of σ_c^2 signalling the linear instability

$$\sigma_c^2 = \frac{2}{(1 + \Gamma)^2}.$$

2.2 Modified random generalised Lotka-Volterra model

Governing equations

As in Section 2.1, we consider a system of N coexisting species, indexed by $i = 1, ..., N$. The population density of species i is denoted by x_i but now it doesn't evolve according to (2.1), but rather according to a modified version of (2.1). Since a rigorous description of the governing equations is beyond the scope of the project, the following sloppy but practical description in the limit of continuous time will be accepted

$$\begin{cases} \dot{x}_i = x_i\Big(1 - x_i + \sum_{i\neq j} \alpha_{ij} x_i\Big) & \text{if } x_i > \theta \\ x_i = 0 & \text{otherwise} \end{cases}, \tag{2.23}$$

where the new parameter θ represents a critical threshold in population density, below which species are forced to become extinct. The rest of parameters have already been described in Section 2.1 and remain having the same definition and properties as before.

Fixed point ansatz and order parameter equations

Following an analogous analytical approach as that of the fixed point *ansatz* described in Section 2.2, one obtains the following dynamical mean-field description

$$x(z) = \begin{cases} \frac{1+\mu M^* + \sqrt{q}\sigma z + h}{1-\Gamma\sigma^2\chi} & \text{if } \frac{1+\mu M^* + \sqrt{q}\sigma z + h}{1-\Gamma\sigma^2\chi} > \theta \\ 0 & \text{otherwise} \end{cases}. \tag{2.24}$$

This order parameters M^*, χ and q present in the above equation (2.24) are defined by equations (2.4)-(2.6). By substituting equation (2.24) into equations (2.4)-(2.6), the modified parameter equations can be obtained as follows

$$M^* = \frac{\sqrt{q}\sigma}{1-\Gamma\sigma^2\chi}\int_u^{+\infty} (\Delta + z) Dz, \tag{2.25}$$

$$1 = \frac{\sigma^2}{(1-\Gamma\sigma^2\chi)^2}\int_u^{+\infty} (\Delta + z)^2 Dz, \tag{2.26}$$

$$\chi = \frac{1}{1-\Gamma\sigma^2\chi}\int_u^{+\infty} Dz + \frac{e^{-u^2/2}}{\sqrt{2\pi}}\frac{\theta}{\sqrt{q}\sigma} \tag{2.27}$$

$$u = \theta\beta - \Delta, \tag{2.28}$$

$$\beta = \frac{1-\Gamma\sigma^2\chi}{\sqrt{q}\sigma}, \tag{2.29}$$

$$\Delta = \frac{1+\mu M^*}{\sqrt{q}\sigma}. \tag{2.30}$$

We can rewrite the parameter equations (2.25)-(2.30) in a more compact form using the functions previously defined in equations (2.12)-(2.14), but evaluated at u instead

$$M^* = \frac{1}{\beta}\Big(\Delta w_0(u) + w_1(u)\Big), \tag{2.31}$$

$$q = \frac{1}{\beta^2}\Big(\Delta^2 w_0(u) + 2\Delta w_1(u) + w_2(u)\Big), \tag{2.32}$$

$$\sqrt{q}\sigma\chi = \frac{\theta}{\sqrt{2\pi}}e^{-u^2/2} + \frac{w_0(u)}{\beta}, \tag{2.33}$$

$$u = \theta\beta - \Delta, \tag{2.34}$$

$$\beta = \frac{1-\Gamma\sigma^2\chi}{\sqrt{q}\sigma}, \tag{2.35}$$

$$\Delta = \frac{1+\mu M^*}{\sqrt{q}\sigma}. \tag{2.36}$$

Henceforth, the functional dependence on u of the functions defined in equations (2.12)-(2.14) will be omitted.

Closed-form solution of the order parameter equations

The parameter equations (2.31)-(2.36) can be solved parametrically. This set of equations can be thought of as a system of 6 equations with 6 unknowns, namely M^*, q, σ^2, χ, Δ and β. The remaining quantities μ and Γ are known constants describing the system. Finally, u is to be regarded as a known parameter which will range from -10 to 10. The goal is to substitute all equations (2.31),(2.32) and (2.34)-(2.36) into equation (2.33) until it is reduced to a cubic equation in Δ, with coefficients only depending on u and on the above-mentioned known quantities μ and Γ. After this is done, the cubic equation is solved and a value for Δ is found. This is enough to retrieve the values of all other 5 unknowns, as we will show now.

We will use equations (2.31),(2.32) and (2.34)-(2.36) to reduce equation (2.33) to a cubic equation in Δ. For clarity, we define the constant K this way

$$K := \frac{\theta}{\sqrt{2\pi}} e^{-u^2/2},$$

which allows us to rewrite (2.33) in the compact form

$$\sqrt{q}\sigma\chi - \frac{w_0}{\beta} = K.$$

First we will rewrite the LHS of the above equation. The first step is to elminate the unknowns χ and σ^2 by using equations (2.35) and (2.36) respectively

$$\begin{aligned}\sqrt{q}\sigma\chi - \frac{w_0}{\beta} &= \sqrt{q}\sigma\frac{\beta\sqrt{q}\sigma - 1}{-\Gamma\sigma^2} - \frac{w_0}{\beta} = -\frac{\beta q}{\Gamma} + \frac{\sqrt{q}}{\Gamma\sigma} - \frac{w_0}{\beta} \\ &= -\frac{\beta q}{\Gamma} + \frac{\sqrt{q}}{\Gamma}\frac{\Delta\sqrt{q}}{1+\mu M^*} - \frac{w_0}{\beta} = -\frac{\beta q}{\Gamma} + \frac{\Delta q}{\Gamma(1+\mu M^*)} - \frac{w_0}{\beta}.\end{aligned}$$

Equating the rewritten LHS and the RHS we find

$$-\frac{\beta q}{\Gamma} + \frac{\Delta q}{\Gamma(1+\mu M^*)} - \frac{w_0}{\beta} = K.$$

Multiplying the above equation by the factor $\beta^2\Gamma(1+\mu M^*)$ yields

$$\Delta q\beta^2 - \beta^3 q(1+\mu M^*) - w_0\Gamma\beta(1+\mu M^*) - \beta^2 K\Gamma(1+\mu M^*) = 0.$$

Now we will use equations (2.31), (2.32) and (2.34) to eliminate the unknowns M^*, q and β respectively in the above equation. We will study each of the 4 addends in the above equation separately. The goal is to express each of them only in terms of the unknown Δ and/or known quantities. The terms will be rearranged by powers of Δ, as follows

$$\Delta q\beta^2 = \Delta(\Delta^2 w_0 + 2\Delta w_1 + w_2) = w_0\Delta^3 + 2w_1\Delta^2 + w_2\Delta,$$

$$\begin{aligned}\beta^3 q(1+\mu M^*) &= \beta(\Delta^2 w_0 + 2\Delta w_1 + w_2)\left(1 + \frac{\mu}{\beta}(\Delta w_0 + w_1)\right) \\ &= (\Delta^2 w_0 + 2\Delta w_1 + w_2)\left[\left(\frac{u}{\theta} + \mu w_1\right) + \left(\frac{1}{\theta} + \mu w_0\right)\Delta\right] \\ &= w_0\left(\frac{1}{\theta} + \mu w_0\right)\Delta^3 + \left[2w_1\left(\frac{1}{\theta} + \mu w_0\right) + w_0\left(\frac{u}{\theta} + \mu w_1\right)\right]\Delta^2 + \\ &\quad + \left[w_2\left(\frac{1}{\theta} + \mu w_0\right) + 2w_1\left(\frac{u}{\theta} + \mu w_1\right)\right]\Delta + w_2\left(\frac{u}{\theta} + \mu w_1\right),\end{aligned}$$

$$w_0\Gamma\beta(1+\mu M^*) = w_0\Gamma\big(\beta + \mu(\Delta w_0 + w_1)\big) = w_0\Gamma\left(\frac{1}{\theta} + \mu w_0\right)\Delta + w_0\Gamma\left(\frac{u}{\theta} + \mu w_1\right),$$

$$\begin{aligned}\beta^2 K\Gamma(1+\mu M^*) &= \beta^2 K\Gamma + \beta^2 K\Gamma\mu M^* = \frac{u^2 + 2u\Delta + \Delta^2}{\theta^2} K\Gamma + K\Gamma\mu\frac{u+\Delta}{\theta}(\Delta w_0 + w_1) \\ &= \frac{K\Gamma}{\theta}\left(\frac{1}{\theta} + \mu w_0\right)\Delta^2 + \frac{K\Gamma}{\theta}\left[\frac{2u}{\theta} + \mu(uw_0 + w_1)\right]\Delta + \frac{K\Gamma}{\theta}\left(\frac{u^2}{\theta} + \mu u w_1\right).\end{aligned}$$

Now we can rearrange the equations by powers of Δ and define the coefficients of a cubic equation in Δ. We recall that the cubic equation comes from eliminating all unknowns except for Δ in equation (2.33)

$$a\Delta^3 + b\Delta^2 + c\Delta + d = 0, \tag{2.37}$$

$$\begin{aligned}
a &:= w_0\left(1 - \frac{1}{\theta} - \mu w_0\right),\\
b &:= 2w_1\left(1 - \frac{1}{\theta} - \mu w_0\right) - w_0\left(\frac{u}{\theta} + \mu w_1\right) - \frac{K\Gamma}{\theta}\left(\frac{1}{\theta} + \mu w_0\right),\\
c &:= w_2\left(1 - \frac{1}{\theta} - \mu w_0\right) - 2w_1\left(\frac{u}{\theta} + \mu w_1\right) - w_0\Gamma\left(\frac{1}{\theta} + \mu w_0\right) - \frac{K\Gamma}{\theta}\left[\frac{2u}{\theta} + \mu(uw_0 + w_1)\right],\\
d &:= -w_2\left(\frac{u}{\theta} + \mu w_1\right) - w_0\Gamma\left(\frac{u}{\theta} + \mu w_1\right) - \frac{K\Gamma}{\theta}\left(\frac{u^2}{\theta} + \mu u w_1\right).
\end{aligned}$$

This means that the modified parameter equations have been solved. The parameter u will range between -10 and 10. For each value of u, the coefficients a, b, c and d of a cubic polynomial must be computed according to the above relations. Then the cubic equation is solved, and a value for Δ is found. We can obtain the value of β by using (2.37)

$$\beta = \frac{u + \Delta}{\theta}.$$

Then equations (2.31) and (2.32) can be used to calculate M^* and q respectively. The value of σ^2 can be obtained via equation (2.36) as follows

$$\sigma^2 = \left(\frac{1 + \mu M^*}{\sqrt{q}\Delta}\right)^2.$$

Finally, the value of χ can be computed from equation (2.33) this way

$$\chi = \frac{1}{\sqrt{q}\sigma}\frac{\theta}{\sqrt{2\pi}}e^{-u^2/2} + \frac{1}{\sqrt{q}\sigma}\frac{w_0}{\beta}.$$

Stability analysis

For a given value of Γ, a complete study of the instabilities of the modified rGLV model is still lacking. What is clear is that the instability due to divergent abundances, analogous to that in the original rGLV model (see Section 2.1), is present in the modified rGLV model as well. The values for the critical points in the plane can be predicted by the theoretical model, as follows

- **Instability due to divergent abundances**. The onset of divergent abundances is signalled by a divergent mean abundance M^*. First observe that, for the critical pairs (ν, σ^2) such that $M^* \longrightarrow \infty$, one has $\Delta \longrightarrow -u$. This is because equations (2.34) and (2.37) imply

  $$\Delta = \frac{\theta w_1 - uM^*}{M^* - \theta w_0} \longrightarrow -u.$$

  Setting $\Delta = -u$ in the cubic equation (**??**), a linear equation in the unknown μ is obtained. This allows us to find the μ_c value of the critical pair as follows

  $$\mu_c = -\frac{\mu^0}{\mu^1},$$

  where μ^0 and μ^1 are given by

  $$\begin{aligned}
  \mu^0 &:= -w_0u^3 + 2w_1u^2 - w_2u,\\
  \mu^1 &:= w_0^2u^3 - 3w_0w_1u^2 + (w_0w_2 + 2w_1^2 + w_0^2\Gamma)u - w_1w_2 - w_0w_1\Gamma.
  \end{aligned}$$

  Once μ_c has been computed, it must be substituted into the original cubic equation (2.37). Then the original cubic equation is solved for Δ as usual, which will in turn give some value for σ_c^2. Thus, the critical pair (μ_c, σ_c^2) is computed as a curve parametrized by u. Another procedure to find the critical lines of divergent abundance is the following. Consider equations (2.25)-(2.30). They are formally identical to equations (2.8)-(2.11), except for two facts: in the lower limits of the integrals involved one finds u instead of $-\Delta$, and there is an additional term in equation (2.27) compared to its counterpart (2.9). We wil see now that, in the limit

$M^* \longrightarrow \infty$, the set of equations (2.25)-(2.30) reduces to the set of equations (2.8)-(2.11). The first difference regarding the integration limits disappears when $M^* \longrightarrow \infty$ because $\Delta \longrightarrow -u$. The second difference regarding the additional term disappears as well when $M^* \longrightarrow \infty$ because it approaches zero when $^* \longrightarrow \infty$, as we will see now. First of all, note that the only way for M^* to diverge is that $\beta \longrightarrow 0$ since equation (2.31) implies M^* is the quotient of a bounded constant quantity divided by β. By (2.32), this implies $q \longrightarrow \infty$ and therefore the additional term $e^{-u^2/2}\theta/\sqrt{2\pi q\sigma^2} \longrightarrow 0$. The fact that the set of equations (2.25)-(2.30) reduces to the set of equations (2.8)-(2.11) when $M^* \longrightarrow \infty$ implies that the lines of divergent abundance must be the same for both the modified and original rGLV models.

- **Other types of instability**. The study of other types of instability, analogous to the linear instability in the original rGLV model (see Section 2.1), is beyond the scope of this project since an analysis based on the path integral formalism would be needed.

3 Results and discussion

In this section, we describe and discuss the results obtained in four numerical experiments related to species abundances and the ratio of survivors, stability indicators, stability diagrams and abundance distributions, respectively. Before that, a note on the numerical simulation of the order parameters and stability indicators must be made.

The way in which order parameters are numerically simulated is the following

- The fraction of surviving species can be simulated by the alternative expression

$$\phi = \lim_{N\to\infty} \frac{1}{N} \sum_i^N \overline{\Theta(x_i^*)},$$

where $\Theta(\cdot)$ denotes the Heaviside function, i.e. $\Theta(x) = 1$ for $x > 0$ and $\Theta(x) = 0$ for $x \leq 0$. The notation x_i^* indicates abundances at stable fixed points.

- The mean abundance M^* per species is simulated according to the formula

$$M^* = \lim_{N\to\infty} \frac{1}{N} \sum_i^N \overline{x_i^*},$$

which is the first moment of abundances.

It is also important to define the following pair of stability indicators

- One possible indicator to characterize whether the system has reached a fixed point or not, is to calculate the relative variation of species abundances (i.e. the fluctuations), which is defined as

$$h^2 = \frac{\frac{1}{N}\sum_i^N \left(\overline{x_i(t)^2} - \overline{x_i(t)}^2\right)}{\frac{1}{N}\sum_i^N \overline{x_i(t)^2}},$$

where the overline denotes averages over time in the stationary state. If $h^2 \sim 0$, the system has converged to a fixed point, while a positive h^2 indicates volatile dynamics or unbounded growth if it diverges. When performing numerical simulations, we will say that a fixed point has been reached if $h^2 < 0.001$.

- Another relevant indicator is given by

$$d^2 = \frac{\overline{\frac{1}{N}\sum_i^N \left(x_i(t) - x_i'(t)\right)^2}}{\frac{1}{N}\sum_i^N x_i'(t)^2},$$

which allows us to study the phase with multiple fixed points by performing two simulations for the same interaction matrix with different initial conditions, generated randomly. If $d^2 < 0.001$ and $h^2 \sim 0$, the system reaches a unique fixed point independent of initial conditions. If $d^2 > 0$ and $h^2 \sim 0$, a fixed point is reached but it depends on initial conditions. If $h^2 > 0$, the system has not converged to a fixed point, regardless of d^2.

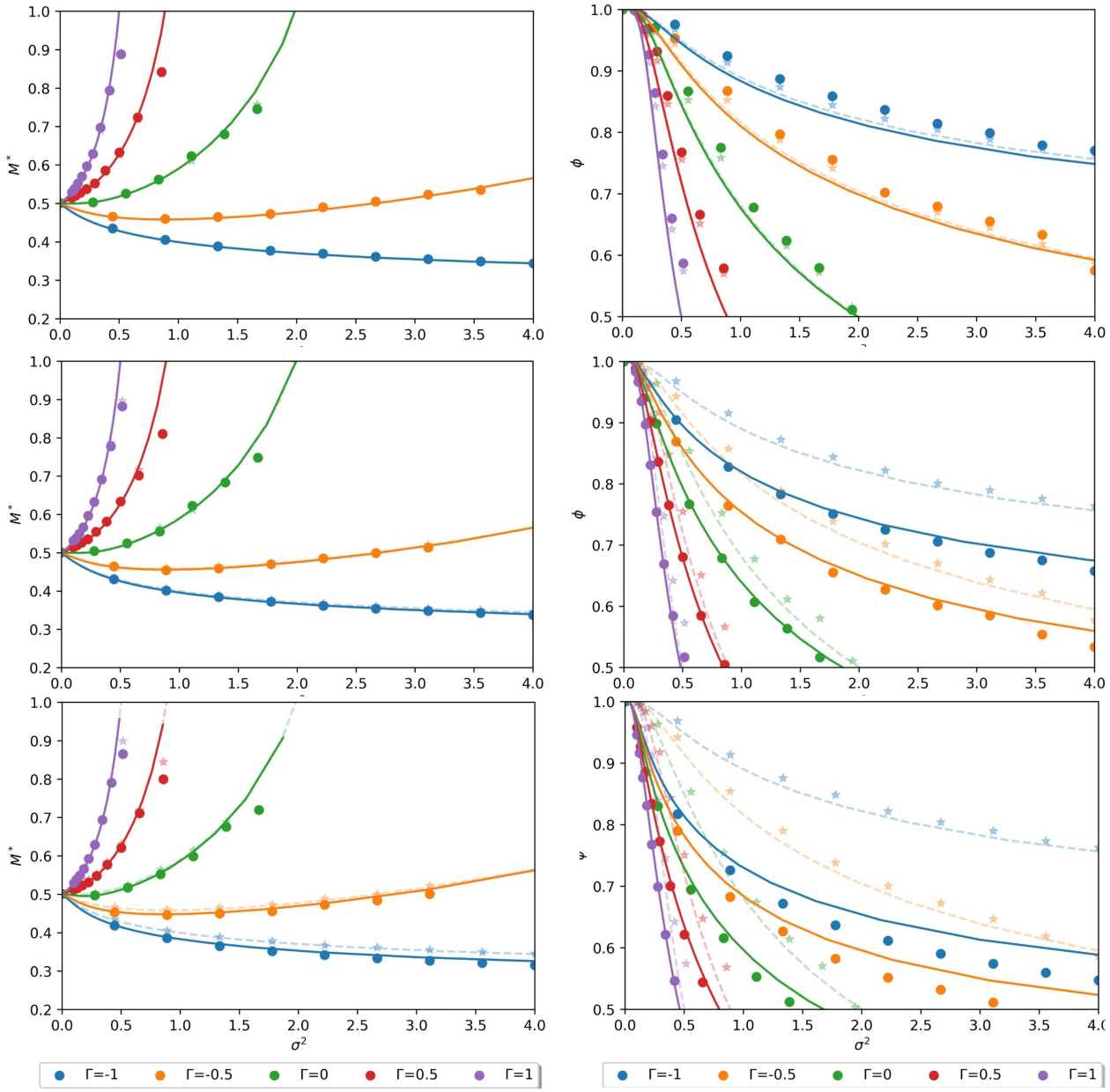

Figure 3: Left column shows mean abundance M^* as a function of σ^2. Right column shows the fraction of surviving species ϕ as a function of σ^2. First row shows the results for a threshold $\theta = 0.01$, second row for $\theta = 0.1$ and third row for $\theta = 0.2$. Light colors show the results for the original rGLV model, whereas darker colors show the results for the modified rGLV model. Solid and dashed lines represent theoretical results for the modified and original rGLV models respectively. Point and star markers represent numerical results for the modified and original rGLV models respectively. The study has been performed for five different values of Γ, which correspond to the five different colors used in the plots according to the legends on the bottom.

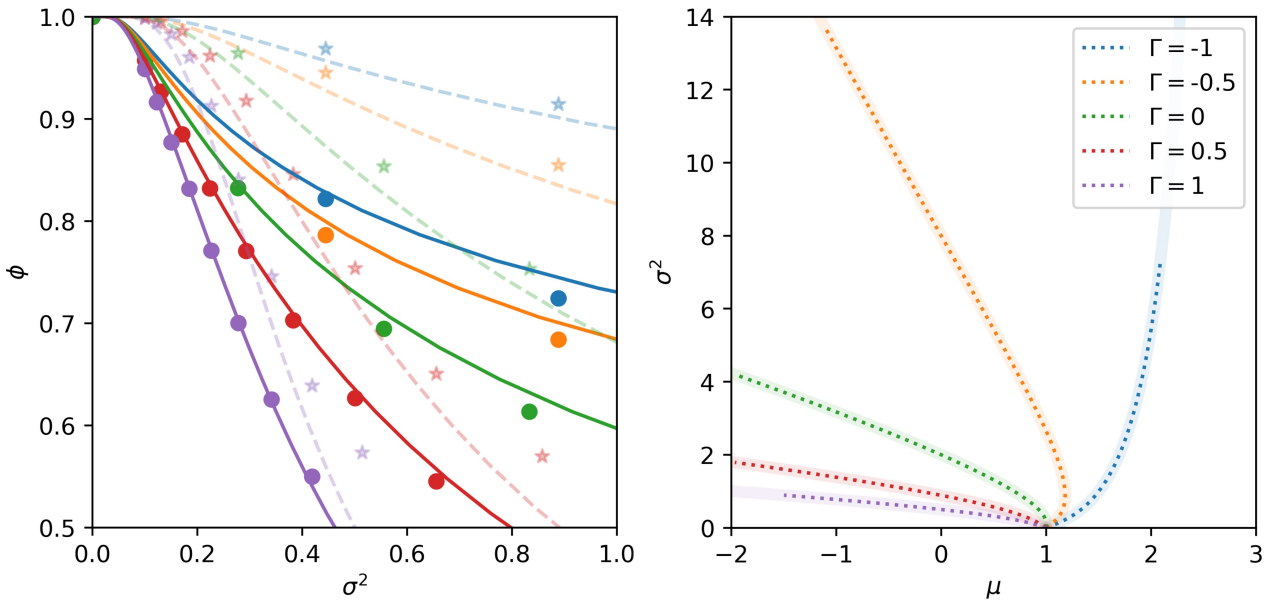

Figure 4: Zoom view of subfigure in lower right corner of Figure 3 (left). Lines of divergent abundance instability for both the original rGLV model (solid lines, light colors) and the modified rGLV model with $\theta = 0.1$ (dotted lines, dark colors). The results describe five different Γ values, color-coded as indicated in the legend (right).

Species abundance and ratio of survivors

The goal of the first experiment was to test the closed-form solution of the order parameter equations that has been extended for the modified rGLV model in Section 2.2, and see whether it agrees with numerical experiment. Results for the original rGLV model have also been included for comparison in lighter colors, as can be seen in Figure 3.

When a negligible threshold $\theta = 0.01$ is chosen, the modified rGLV model matches the results of the original rGLV model as expected (first row in Figure 3). For higher values of the threshold $\theta = 0.1$ (second row in Figure 3), no changes are noticed in mean abundance. The fraction of survivors, however, does become lower in the modified case compared to the original rGLV model. The difference is especially noticeable for positive values of the correlation parameter Γ.

It should be noted that the closed-form solution in the modified case successfully reproduces numerical simulations, for low thresholds ranging between $0.01 \leq \theta \leq 0.1$ (see dark color lines and points in the first and second rows of Figure 3). However, for higher $\theta = 0.2$, theoretical predictions deviate considerably from numerical simulations in the modified rGLV model (third row in Figure 3). It is still unclear whether these deviations are due to a lack of numerical precision or to the fact that the theoretical lines are only expected to match numerical experiment in the stable phase i.e. the theoretical lines are only valid for unique stable fixed points.

It is important to take into account that this experiment has been performed with no less than $N = 200$ species (in some cases $N = 250$), no less than $m = 100$ realisations (in some cases $m = 150$) and the dynamics has been allowed to evolve during no less than $M = 7000$ timesteps (in some cases $M = 10000$) of length $dt = 0.12$.

Stability diagram

Finally, Figure 4 shows the divergent abundance lines of instability as theoretically predicted in Section 2.2 for the modified rGLV model. Lighter colors show the same instability lines for the original rGLV model. We clearly see that the lines of instability due to divergent abundances are the same in both models, as predicted by theory in Section 2.2. In this case, numerical experiments to test the theoretical predictions haven't been performed because they are too computationally expensive.

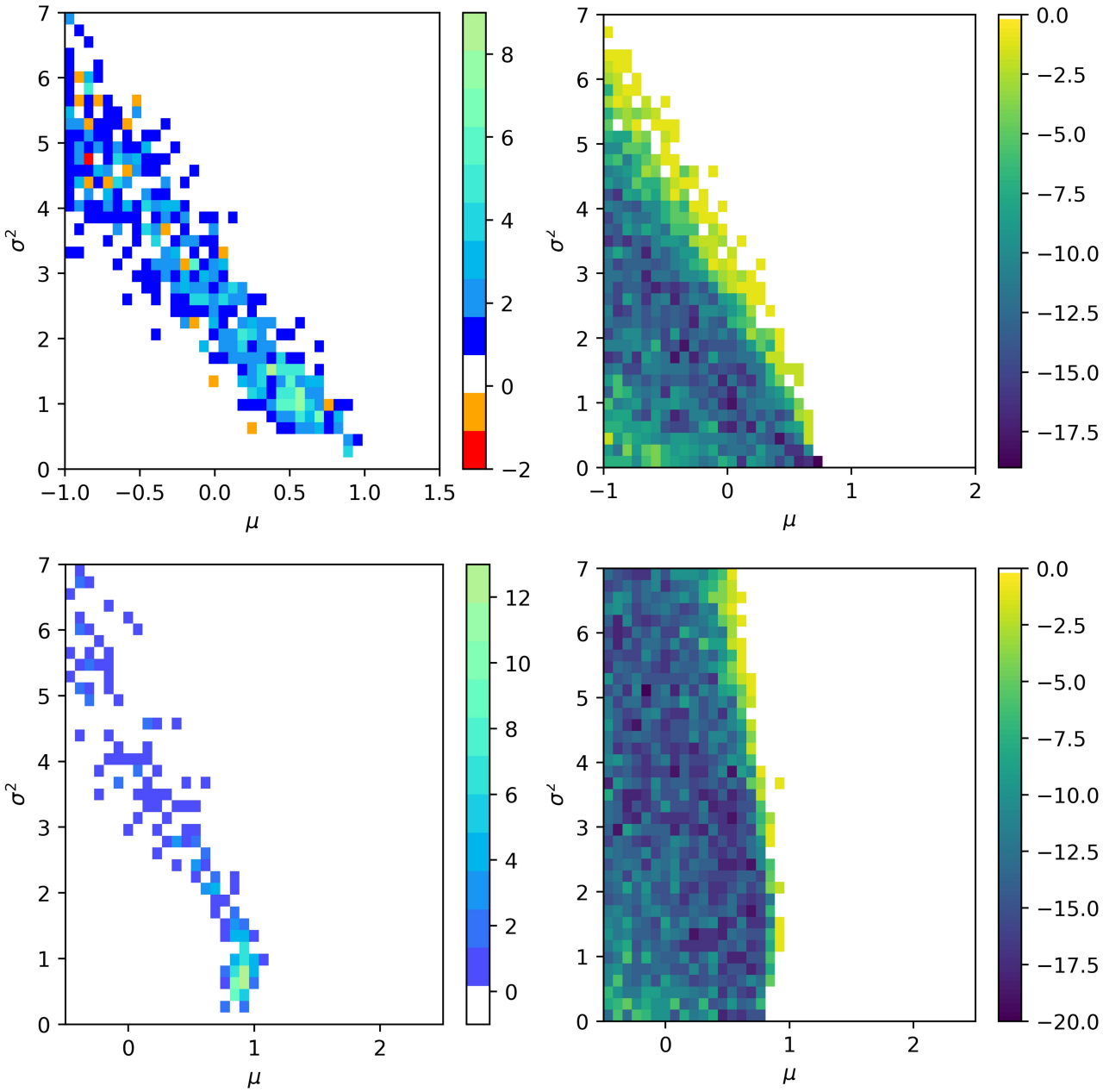

Figure 5: Left column shows stability indicator h^2. Right column shows stability indicator d^2. First row shows the results for $\Gamma = -0.5$, second row for $\Gamma = -1$. According to each color-bar, colours indicate the difference between the number of realisations in which $h^2 < 0.001$ or $d^2 < 0.001$ out of 20 realisations at each point, when the original and modified methods are used. Exactly 20 realisations were computed at each point. For a first example, consider the point $(-1, 7)$ in the upper left diagram. Its blue color signifies that there were 4 realisations out of 20 in which the modified model showed $h^2 < 0.001$ and the original model didn't. For another example, take the point $(0, 7)$ in the lower right diagram. Its dark blue color signifies that there were 20 out of 20 realisations in which the modified model showed $d^2 > 0.001$ and the original model showed $d^2 < 0.001$. The threshold parameter was $\theta = 0.1$ in all cases.

Stability indicators h^2 and d^2 in the (μ, σ^2) plane

In order to assess the claim that the modified rGLV model is somewhat more stable than the original rGLV model, a numerical experiment whose results are shown in Figure 5 has been performed. A value for Γ is chosen (see the first row in Figure 5 to see results in the case $\Gamma = -0.5$). We will now explain how the h^2 indicator has been studied. The following procedure must be repeated a total of 20 times

1. Define two matrices of size (U, V), U being the number of studied values for μ and V being the number of studied values for σ^2. Fill these matrices with zeros. In one of the matrices, values related to the original rGLV model will be stored. In the other, values related to the modified rGLV model will be stored.
2. Fix a point in the (μ, σ^2) plane, as well as a set of initial conditions and a random matrix of coefficients.
3. Numerically integrate the associated equations of both the original rGLV model and the modified rGLV model for a threshold $\theta = 0.1$.
4. Compute parameter h^2 for both the original rGLV model and the modified rGLV model. If $h^2 < 0.001$, sum a unit in the matrix entry corresponding to that point of the plane, in the matrix associated to the corresponding model.
5. Repeat this process for all other points in the (μ, σ^2) plane.

Thus, one obtains two matrices whose entries range between 0 and 20. One of the matrices $M_{original}$ describes, at each point of the plane, the number of realisations (out of 20) in which the original rGLV model reached a value $h^2 < 0.001$. The remaining matrix $M_{modifed}$ offers an analogous description of the indicator h^2 for the modified rGLV model. Finally, the difference between both matrices $M_{modified} - M_{original}$ is represented in Figure 5 (see upper left corner).

The results shown in Figure 5 are inconclusive. For $\Gamma = -0.5$ (upper row of Figure 5), we see that there is a region in which the modified rGLV model does show plenty of points in which $h^2 < 0.001$. This means that, in that predominantly blue region, it is more common for the system to reach a fixed point when the modified rGLV model is used, compared to the original model. When d^2 is computed in all the plane using the modified model, it always happens that $d^2 > 0.001$. Hence, what we see in the upper right corner of Figure 5 is actually $M_{modified} - M_{original} = -M_{original}$. In other words, in the original model unique fixed points are reached regardless of initial conditions in the colored region with $d^2 < 0.001$. However, in the modified model, $d^2 > 0.001$ is positive in all regions, meaning that there is a dependence on initial conditions.

4 Conclusions

Generalized equations describing the order parameters of the dynamical system have been derived for the modified rGLV model. A new closed form solution for the order parameter equations has been found for the modified rGLV model. This has allowed to theoretically predict relevant order parameters, which have been successfully tested against numerical experiment. The instability lines due to divergent abundances have also been analytically studied, turning out to be analogous to those of the original rGLV model. It remains to be numerically checked whether these instability lines predicted by theory for the modified model are correct.

Little numerical evidence has been found in order to support the initial claim that the stability is in some sense higher in the modified rGLV model for some regions of the (μ, σ^2) plane, compared to the original rGLV model. A deeper understanding of the MSR formalism and dynamic mean-field theory are necessary in order to make significant progress in the analytical study of the modified rGLV model.

Acknowledgments

Acknowledge support and useful discussions:

This work was supported by the SURF@IFISC fellowship. I would like to thank my tutor Tobias Galla for his insightful advice and for dedicating generously a lot of time to help me with this work. I would also like to thank Carlotta Nunzi and Adrián Roig for helping me with this work so kindly and welcomingly.

References

[1] Galla, Tobias. (2024) *Generating-functional analysis of random Lotka–Volterra systems: A step-by-step guide*, preprint arXiv:2405.14289.

[2] Larroya Paixà, Ferran. (2020) *Stochastic and Deterministic approaches to the Generalised Random Lotka-Volterra Communities* , Master's Thesis, URI: http://hdl.handle.net/11201/156952.

[3] Allesina, S., Tang, S. The stability–complexity relationship at age 40: a random matrix perspective. Popul Ecol 57, 63–75 (2015). https://doi.org/10.1007/s10144-014-0471-0.

[4] Inordinatum (2012) An introduction to the Martin-Siggia-Rose formalism. Available at https://inordinatum.wordpress.com/2012/09/27/a-quick-introduction-to-the-martin-siggia-rose-formalism/.

Using Deep Learning to outperform network science

Adam César Maćkowiak Pellón, Massimiliano Zanin
Instituto de Física Interdisciplinar y Sistemas Complejos, IFISC (CSIC-UIB)
Campus Universitat de les Illes Balears, E-07122 Palma de Mallorca, Spain

Abstract

The problem of group-level comparison of sets of complex networks is usually tackled through two, prima facie orthogonal, approaches: the analysis of topological properties, as customary in statistical physics, and the training and evaluation of Deep Learning models in computer science. A fundamental and hitherto unanswered question is, which one is better? We here sketch an answer by comparing the performance of both viewpoints on undirected unweighted networks generated using a suite of synthetic models. We show that topological metrics outperform Deep Learning whenever the differences between the networks are structural; the latter can nevertheless go further and discriminate networks that are different but topologically equivalent. We further propose a minimal way of merging both approaches, i.e. using the output of a Deep Learning model as a topological feature, to achieve outstanding results in both situations.

1 Introduction

A fundamental problem arising in many scientific endeavours is the quantification, and eventually description, of the differences between sets of systems, i.e. what is known as group-level comparison. A clear example involving complex network theory is the study of the differences between brain connectivity of patients and control subjects [1, 2, 3], both at structural and functional levels [4, 5]. The researcher aims at knowing whether the reconstructed network representations are dissimilar in both groups, or in other words, whether they are identifiable [6]; for then proceeding to extract quantitative descriptions of such dissimilarities, towards validating hypotheses about the pathogenesis, endophenotypes, or diagnostic markers of the disorder. Finding no differences between groups can also be relevant, as it may either suggest that they are equivalent, or that the reconstructed network representations are not optimal.

Among the many approaches for group-level network comparison [2], statistical physics has traditionally focused on topological metrics [7], i.e. the quantification of specific structural patterns or features. This simply requires comparing the probability distributions of a given metric for both groups, leveraging suitable statistical tests when a p-value is needed; but is nevertheless limited by its reliance on a pre-hoc hypothesis about which topological feature is actually relevant. An alternative has recently started to emerge, based on Deep Learning (DL): roughly speaking, computational models inspired by the structure of neurons in the human brain and trained to perform specific tasks [8, 9]. Such models can be trained to distinguish between two sets of networks in a hypothesis-free way, thanks to their capacity of internally synthesising relevant features from data; yet, the black-box nature of this process makes it difficult to extract what is represented by these features, and hence, which topological properties are affected.

If DL models are able to recover standard topological metrics [10], it stands to reason to expect the former one to be able to discriminate groups of networks with a similar (if not higher) efficiency than the latter ones. Whether and under which conditions this is actually true, is nevertheless a question that has hitherto not been tackled. We here provide a first answer by resorting to a set of generative algorithms, creating (undirected and unweighted) networks of known (and tuneable) topological characteristics; for then evaluating the results yielded by both methodologies as a function of the programmed dissimilarity.

2 Theoretical model

We consider the following sets of unweighted and undirected networks, created using well-known generative models:

- Erdős-Rényi (ER) random networks with fixed number of nodes and tuneable probability of edge creation, i.e. of tuneable link density.
- Watts–Strogatz (WS) small-world networks [11] with fixed number of nodes and of nearest neighbours ($k = 4$), and with tuneable rewiring probability. The latter parameter allows to change two characteristics of the resulting networks, namely the efficiency [12] and the transitivity [13].
- Random networks of known degree distribution, created using a configuration model [14]. The considered distribution corresponds to a power law, which is defined by its exponent; the resulting networks thus have a tuneable α, calculated through the method proposed by Clauset et al. [15].
- Modular networks created using a stochastic block model, composed of two communities of equal size and equal inter- and intra-community link density. The tuneable parameter is the latter, while the former is varied to maintain a constant overall link density. The resulting measured property is the modularity of the network, estimated through the metric Q [16] calculated over the best partition obtained by the Louvain community detection algorithm [17].
- Networks of tuneable assortativity, obtained by starting from a Dorogovtsev-Goltsev-Mendes graph [18] that undergoes a Spectral Graph Forge (SGF) [19] randomisation process with a user-defined ratio of preserved eigenvectors of the initial adjacency matrix.

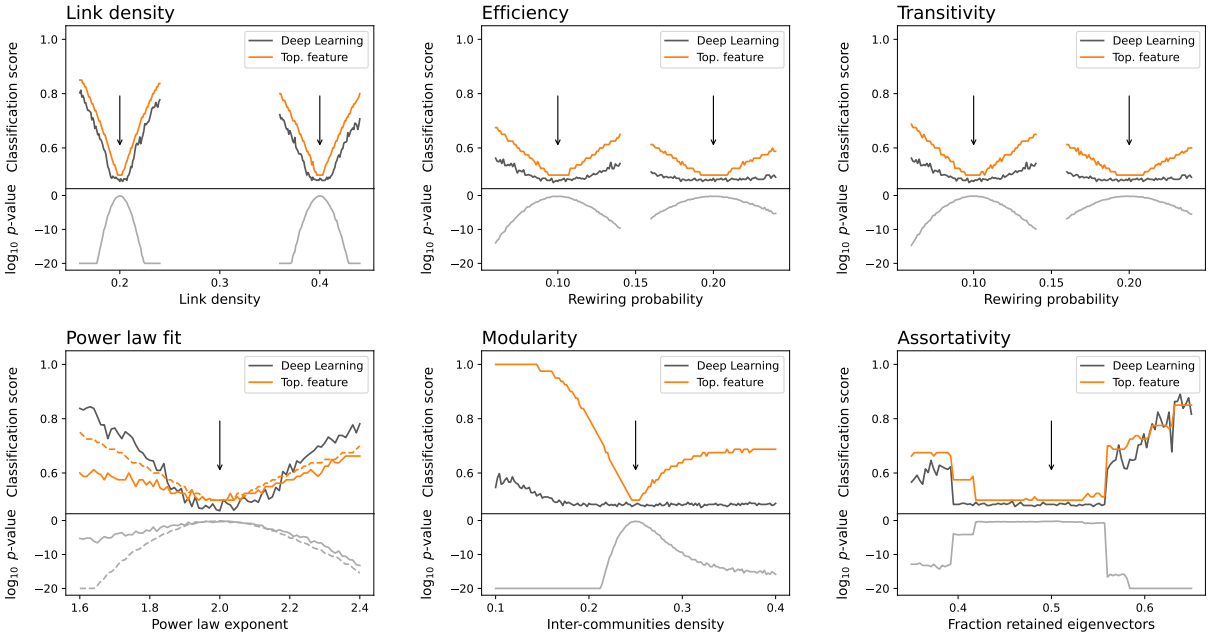

Figure 1: Classification of synthetic networks of known properties. Each panel reports the results obtained when comparing two groups of $n = 200$ networks created with synthetic models - see main text for definitions. Dark grey and orange lines respectively correspond to the classification score obtained by the DL model, and by the DT trained with the extracted topological metric (see title of each panel). For each set of lines, the vertical arrow indicates the value of the tuneable parameter for one set of networks, while the abscissa the parameter for the second set. Light grey lines in bottom graphs report the $\log_{10}$ of the p-value of a K-S test between the observed topological metrics in both groups; note that values smaller than 10^{-20} are not reported. The dashed lines in the bottom left panel correspond to the use of the maximum degree. In all cases, results correspond to the median calculated over 200 independent realisations.

To illustrate the approach underpinning the numerical experiments, let us suppose that two equal-size sets a and b of ER networks are created with slightly different values of the link densities, i.e. d_l^a and d_l^b. Firstly, these can be compared by extracting the corresponding topological metric (in this example, the sample link density $\hat{d}_l$) from each network, thus obtaining a probability distribution for each of the two sets; and by comparing these using a two-sample Kolmogorov-Smirnov (K-S) test. Note that in general $\hat{d}_l \neq d_l$, and that the latter is usually not known; hence the need to resort to the sample estimation of the metric. Secondly, $\hat{d}_l$ can be used to train a classical machine learning model - we here consider a simple Decision Tree (DT) [20] of one single level and a ten-fold cross-validation. Thirdly, the raw adjacency matrices can be used to train and

evaluate a DL model, using a random half of the network in each case. The DL model here used in an extended version [21] of the Graph Isomorphism Neural Network (GIN) paradigm [22], i.e. artificial neural networks designed to learn over graph data, and leveraging recursive neighbourhood aggregations to detect isomorphic structures [23] [1]. In short, given two sets of networks differing in a known topological feature, we compare three analysis methods: the statistical significance of the difference between the observed feature; the usefulness of the observed feature to distinguish both groups, leveraging classical machine learning; and the capacity of DL to recover similar information only using the raw structure of the network.

3 Results and discussion

Fig. 1 reports a synthesis of the main results for networks of $N = 30$ nodes - this initial network size has been chosen for being the number of sensors typically available in EEG setups. As expected, the farther away are the parameters driving the creation of the two sets of networks, the smaller the p-value yielded by the K-S test - see light grey lines in the bottom graph of each panel. The behaviours of the two remainder approaches are nevertheless more complex. DL (dark grey lines) clearly outperforms the direct use of the topological metric (orange lines) only in the case of the power law model (bottom left panel). Note that this may be caused by the fact that the estimation of this topological metric is very unreliable and noisy due to the very small network size, as confirmed by the improvements in the results when considering the maximum degree, see dashed lines. In all other cases, the use of the topological feature yields generally better results than DL.

In order to understand the effect of the network size, the top panel of Fig. 2 reports the evolution of the classification score obtained by the DL approach as a function of the number of nodes in the network. To simplify the analysis, networks correspond to the left-most value of each graph in Fig. 1 - i.e. to the maximum difference between the two network sets. The evolution is quite clear, and suggests that large networks are beneficial for DL, provided the difference is one that the model can distinguish. Note that this result is not trivial: large networks contain more information, and should therefore be more difficult to analyse. As previously suggested in the literature, our understanding of the capacity of DL to avoid overfitting in the case of very high dimensional input data is still quite limited [24, 20].

As a final point, we analyse whether the poor results obtained by DL for some network structures could be due to the limited size of the data sets here considered - as it is well known that this framework requires very large number of training examples in order to converge to a reliable result. The bottom panel of Fig. 2 reports the evolution of the classification score as a function of the number of networks available in the training phase. As in the previous case, each line corresponds to the left-most value of each graph in Fig. 1. While a weak increasing trend can be observed, no substantial benefit is obtained by using more than 400 networks; and, most notably, a larger number of networks does not impact results for assortative, modular, and WS structures. In short, the topological features to be detected are basic enough to require few examples to be described; the low performance of DL in these three cases is thus due to structural limitations.

The above results seem to indicate that the DL model is detecting differences between networks that are not necessarily linked to standard topological metrics used in the literature. We test this by resorting to a synthetic model, based on two reference networks $\mathcal{G}_1$ and $\mathcal{G}_2$, both corresponding to Erdős-Rényi graphs of equal number of nodes and link probability. We then create two sets of networks, starting with ER graphs (also with the same number of nodes and links), but whose links are copied from the corresponding reference network with an overlap probability p_o. In other words, for $p_o \approx 0$, the two sets are composed of completely random graphs - they are hence not identifiable. Increasing p_o makes the networks in each set more similar to the corresponding reference, hence more identifiable; up to the point that, for $p_o = 1$, all networks in a set are equal to the reference. Note that both $\mathcal{G}_1$, $\mathcal{G}_2$, and all individual networks are random ones, i.e. they have no characteristic structure; topological metrics yield values as expected in ER graphs, independently on p_o; and a topological analysis would thus be useless.

As can be seen in the top panel of Fig. 3, depicting the median classification score as a function of the overlap probability p_o, the DL model is able to successfully discriminate between the two groups. Results are further stable independently on the number of networks used in the training (bottom panel of the same figure), but worsen with larger networks (middle panel).

[1] The DL model is composed of three convolutional layers of dimension (h, h) and two fully connected layers of size $3h$, where $h = 32$. Unless otherwise stated, training has been performed over $2,000$ epochs and with a batch size of 64; and all results are the median over 200 independent realisations.

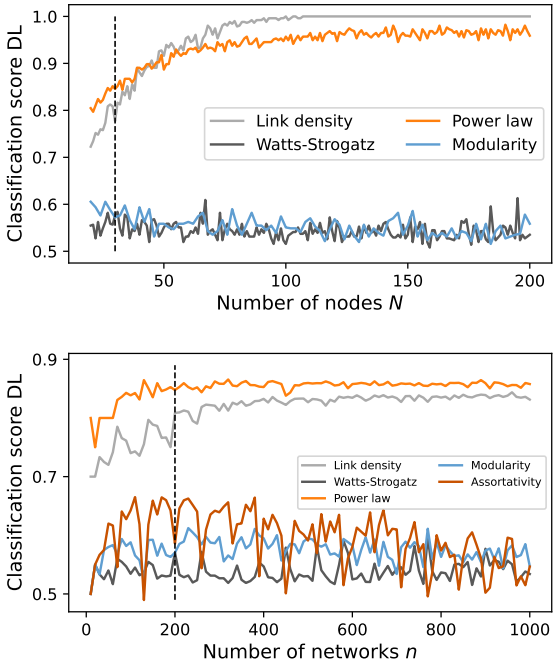

Figure 2: Characteristics of the networks. (Top) Evolution of the classification score obtained by the DL model as a function of the number of nodes N in each network. (Bottom) Evolution of the classification score as a function of the number of networks n used in the training phase. Networks correspond to the left-most value of each graph in Fig. 1. The vertical dashed lines indicate the number of nodes (top) and networks (bottom) used in Fig. 1, i.e. $N = 30$ and $n = 200$. In all cases, results correspond to the median calculated over 200 independent realisations.

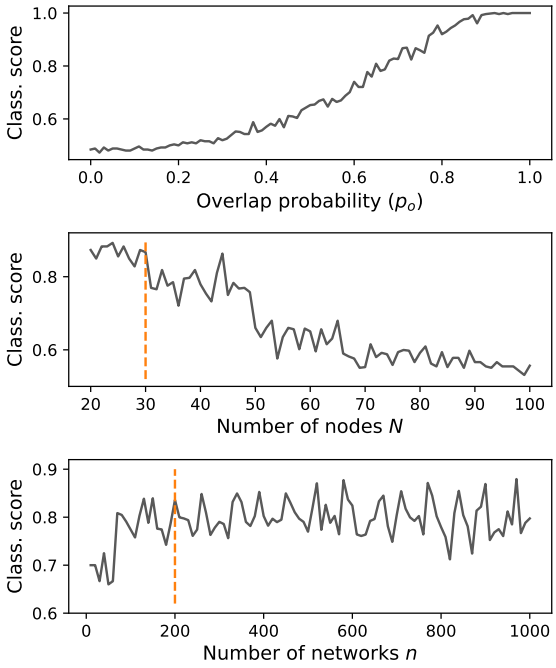

Figure 3: Evolution of the classification score obtained by the DL model over synthetic networks with random topological features - see main text for definition. Top, middle and bottom panels respectively report the results as a function of the overlap probability p_o, the number of nodes N in each network, and the number of networks n used in the training. In the two latter panels, p_o is set to 0.7; the orange dashed vertical lines further report the values used in the top one, i.e. $N = 30$ and $n = 200$. In all cases, results correspond to the median calculated over 200 independent realisations.

The attentive reader will have by now noticed an interesting behaviour in the bottom panels of Figs. 2 and 3, i.e. a regular oscillation in the classification score when the number of networks n used in the training is changed. This oscillation is the result of the interaction between n and the batch size, i.e. the number of networks fed into the DL model at each iteration of the training process, see Fig. 4. While no satisfactory answer can be given at this time, such interaction can be the result of the destabilising effect that small batches can have, which allow escaping poor local minima in the parameter space. Independently on the cause, the practitioner must be aware of these potential problems.

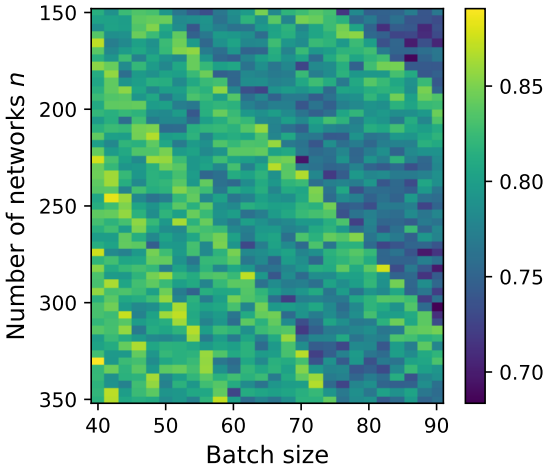

Figure 4: Evolution of the classification score, for the synthetic model of Fig. 3 and $p_o = 0.7$, as a function of the number of networks n used in the training, and the batch size. Results correspond to the median calculated over 500 independent realisations.

As previously shown, topological metrics and Deep Learning seem to be complementary in the way they describe networks. Notably, tertium datur: joining these two approaches is the natural next step, by designing a model to estimate the identifiability of sets of networks, internally combining both contributions. For the sake of simplicity, we here consider a minimal solution based on a Random Forest model [25] trained on features comprising both standard topological metrics and the output of a GINE model. The output of the DL model is thus considered as an additional feature, at the same level of all topological metrics [2].

When comparing the classification score obtained with this hybrid model and that obtained through DL alone (see Fig. 5), the former consistently outperforms the latter. Not only it recovers the score obtained with topological metrics, but it even improves what obtained in the case of the synthetic model presented in Fig. 3 - see light grey diamonds in Fig. 5. Even though the networks composing both sets are random, the hybrid model is able to leverage the small differences in the topological properties of the reference networks $\mathcal{G}_1$ and $\mathcal{G}_2$.

4 Conclusions

While it may be tempting to assume that DL models, being the state of the art in machine learning, should outperform a more classical approach based on evaluating topological features on graphs, we have here shown that the truth is much more complex. When the objective is to assess the difference between two groups of networks, and when such difference is associated to a topological feature that can be measured using a standard metric available in the literature, resorting to DL is generally sub-optimal - see Fig. 1. On the other hand, when such differences are not of a topological nature, and therefore these metrics become useless, the GINE model yields interesting results - see Fig. 3. Still, the practitioner has to be aware of the mixed effect of increasing the size of the analysed networks - see Figs. 2 (top) and 3 (middle). On the positive side, DL models seem to be less sensitive than expected to the number of instances available for training, allowing their application in problems of limited size - see Figs. 2 (bottom) and 3 (bottom). Not completely surprising, the best solution involves merging both approached into a single classification algorithm,

[2] Note that more complex solutions could be envisioned, for instance by introducing topological metrics in intermediate layers of the GINE network.

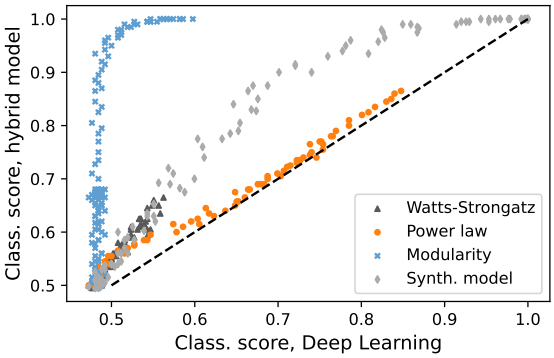

Figure 5: Analysis of an hybrid model combining topological metrics and DL. Each point reports the classification score obtained by the hybrid model, as a function of the score of the original DL model. Points correspond to the network characteristics of Figs. 1 and 3, with symbol colours and shapes defined in the legend.

combining classical topological metrics with the output of the DL model - see Fig. 5. The best way of creating such hybrid model, and the synergies that can emerge, may provide a fertile ground for future research efforts.

References

[1] Ed Bullmore and Olaf Sporns. "Complex brain networks: graph theoretical analysis of structural and functional systems". In: *Nature reviews neuroscience* 10.3 (2009), pp. 186–198.

[2] Junghi Kim, Jeffrey R Wozniak, Bryon A Mueller, Xiaotong Shen, and Wei Pan. "Comparison of statistical tests for group differences in brain functional networks". In: *NeuroImage* 101 (2014), pp. 681–694.

[3] Danielle S Bassett and Olaf Sporns. "Network neuroscience". In: *Nature neuroscience* 20.3 (2017), pp. 353–364.

[4] Christopher J Honey, Olaf Sporns, Leila Cammoun, Xavier Gigandet, Jean-Philippe Thiran, Reto Meuli, and Patric Hagmann. "Predicting human resting-state functional connectivity from structural connectivity". In: *Proceedings of the National Academy of Sciences* 106.6 (2009), pp. 2035–2040.

[5] Hae-Jeong Park and Karl Friston. "Structural and functional brain networks: from connections to cognition". In: *Science* 342.6158 (2013), p. 1238411.

[6] Massimiliano Zanin and Javier M Buldú. "Identifiability of complex networks". In: *Frontiers in Physics* 11 (2023), p. 1290647.

[7] L da F Costa, Francisco A Rodrigues, Gonzalo Travieso, and Paulino Ribeiro Villas Boas. "Characterization of complex networks: A survey of measurements". In: *Advances in physics* 56.1 (2007), pp. 167–242.

[8] Yann LeCun, Yoshua Bengio, and Geoffrey Hinton. "Deep learning". In: *nature* 521.7553 (2015), pp. 436–444.

[9] Ian Goodfellow, Yoshua Bengio, and Aaron Courville. *Deep learning*. MIT press, 2016.

[10] Sebastian Wandelt, Xing Shi, and Xiaoqian Sun. "Complex network metrics: Can deep learning keep up with tailor-made reference algorithms?" In: *IEEE Access* 8 (2020), pp. 68114–68123.

[11] Duncan J Watts and Steven H Strogatz. "Collective dynamics of 'small-world'networks". In: *nature* 393.6684 (1998), pp. 440–442.

[12] Vito Latora and Massimo Marchiori. "Efficient behavior of small-world networks". In: *Physical review letters* 87.19 (2001), p. 198701.

[13] M Ángeles Serrano and Marian Boguna. "Clustering in complex networks. I. General formalism". In: *Physical Review E—Statistical, Nonlinear, and Soft Matter Physics* 74.5 (2006), p. 056114.

[14] Mark EJ Newman. "The structure and function of complex networks". In: *SIAM review* 45.2 (2003), pp. 167–256.

[15] Aaron Clauset, Cosma Rohilla Shalizi, and Mark EJ Newman. "Power-law distributions in empirical data". In: *SIAM review* 51.4 (2009), pp. 661–703.

[16] Michelle Girvan and Mark EJ Newman. "Community structure in social and biological networks". In: *Proceedings of the national academy of sciences* 99.12 (2002), pp. 7821–7826.

[17] Vincent D Blondel, Jean-Loup Guillaume, Renaud Lambiotte, and Etienne Lefebvre. "Fast unfolding of communities in large networks". In: *Journal of statistical mechanics: theory and experiment* 2008.10 (2008), P10008.

[18] Sergey N Dorogovtsev, Alexander V Goltsev, and José Ferreira F Mendes. "Pseudofractal scale-free web". In: *Physical review E* 65.6 (2002), p. 066122.

[19] Luca Baldesi, Carter T Butts, and Athina Markopoulou. "Spectral graph forge: graph generation targeting modularity". In: *IEEE INFOCOM 2018-IEEE Conference on Computer Communications*. IEEE. 2018, pp. 1727–1735.

[20] Oded Z Maimon and Lior Rokach. *Data mining with decision trees: theory and applications*. Vol. 81. World scientific, 2014.

[21] Weihua Hu, Bowen Liu, Joseph Gomes, Marinka Zitnik, Percy Liang, Vijay Pande, and Jure Leskovec. "Strategies for pre-training graph neural networks". In: *arXiv preprint arXiv:1905.12265* (2019).

[22] Zonghan Wu, Shirui Pan, Fengwen Chen, Guodong Long, Chengqi Zhang, and S Yu Philip. "A comprehensive survey on graph neural networks". In: *IEEE transactions on neural networks and learning systems* 32.1 (2020), pp. 4–24.

[23] Keyulu Xu, Weihua Hu, Jure Leskovec, and Stefanie Jegelka. "How powerful are graph neural networks?" In: *arXiv preprint arXiv:1810.00826* (2018).

[24] Tomaso Poggio, Hrushikesh Mhaskar, Lorenzo Rosasco, Brando Miranda, and Qianli Liao. "Why and when can deep-but not shallow-networks avoid the curse of dimensionality: a review". In: *International Journal of Automation and Computing* 14.5 (2017), pp. 503–519.

[25] Leo Breiman. "Random forests". In: *Machine learning* 45 (2001), pp. 5–32.

Maxwell's demon at the nanoscale: Seebeck effects

Sergio Arias Rangel, María Rosa López Gonzalo, Mykhailo Moskalets
Instituto de Física Interdisciplinar y Sistemas Complejos, IFISC (CSIC-UIB)
Campus Universitat de les Illes Balears, E-07122 Palma de Mallorca, Spain

Abstract

We propose a quantum heat engine based on an Aharonov-Bohm interferometer with Rashba Spin Orbit Coupling in a two-terminal geometry and investigate its thermoelectric performances in the linear response regime. Sizeable thermopower (up to 0.5 mV/K) as well as spin seebeck coefficients (up to 0.4 mV/K) can be achieved by simply adjusting parameters of the setup. Changing the magnetic flux, the asymmetry of the structure, a side-gate bias voltage through a capacitively coupled electrode, the average electric field along the axial direction and the transmission of the T junctions connecting the AB ring to the contacts allows us to finely tune the operation of the quantum heat engine.

1 Introduction

The study of thermal properties and heat transport at the nanoscale has received significant attention in recent years [1, 2]. The substantial progress made so far has led to a deeper understanding of the fundamental processes that govern thermal transport and dynamics in solid-state nanosystems, from both theoretical and experimental perspectives. A particularly important question is whether, and to what extent, quantum effects play a role in determining and controlling the performance of nanoscale heat engines, such as their conversion efficiency and output power [4, 5].

While classical thermodynamics remains applicable at the microscale, it is well established that quantum effects and phase coherence can significantly influence the behavior of nanoscopic heat engines. In this context, the well-known Aharonov-Bohm effect [6], which describes the quantum-mechanical phenomenon where a charged particle is affected by electric or magnetic potentials, could serve as a foundational element for the development of efficient quantum heat engines.

Besides quantum mechanics describes particles possessing an intrinsic degree of freedom that is not present in classical mechanics, this is spin. Then, a new field emerges when elements of spintronics [8] and thermoelectrics [3] are combined, focusing on the study of the interplay between spin, charge, and heat currents in materials. In spin caloritronics, it is explored how thermal gradients (differences in temperature) can influence the spin and charge transport properties of materials, and conversely, how spin currents can generate or manipulate thermal effects.

The Rashba interaction, a specific type of spin-orbit interaction, occurs in systems lacking structural inversion symmetry, such as surfaces, interfaces, or certain types of semiconductor heterostructures. In the Rashba effect, the spin degeneracy of electronic states is lifted due to the presence of an external electric field (or an effective field created by the asymmetry), causing a momentum-dependent splitting of the different spin orientations. The strength of the Rashba [7] interaction depends on the magnitude of the electric field and the material's intrinsic properties. This interaction is significant in spintronics, as it enables electric field control of spin states, which is useful for designing spin-based devices like spin transistors. The emergent interdisciplinary field, spin coherent caloritronics, benefits from the quantum coherence and the spin degree of freedom, features that are intrinsic of quantum systems in the context of transport of charge, heat and spin when thermal and electrical gradients are considered. In this context, "spin-coherent" refers to the preservation of the quantum phase relationship between spin states as they propagate through a material or device. This coherence allows for the precise control of spin and heat currents at the quantum level, leading to potentially novel thermoelectric effects and functionalities.

Here we envision and analyze a solid-state phase-coherent heat engine based on a mesoscopic Aharonov-Bohm (AB) ring connected to two fermionic reservoirs. Indeed we consider a non-reciprocal quantum ring [9], where one arm of the ring contains the Rashba spin-orbit interaction but not in the other arm. This set-up is found to posses very unique electronic properties that are reflected in the spin caloritronic transport. One of the key phenomena studied in spin caloritronics

include the spin Seebeck effect [10], where a temperature gradient generates a spin current, and the spin Peltier effect, where a spin current can cause a temperature change. These effects have potential applications in energy conversion, such as developing new types of thermoelectric devices that convert waste heat into electricity, as well as in spin-based information processing and storage technologies.

2 Theoretical model

2.1 Aharonov-Bohm Effect in a 1D Quantum Ring

The set-up under study is that of a particle confined in a circular ring of radius b in the XY plane. Inside the ring there is a magnetic field pointing in the axial direction creating a magnetic flux Φ, which is assumed to be a tunable quantity. Under no other considerations the Hamiltonian of the ring is [11]:

$$\hat{H}_{AB} = \frac{\hbar^2}{2mb^2}\left(-i\frac{\partial}{\partial\phi} + \frac{\Phi}{\Phi_L}\right)^2 \tag{2.1}$$

Following the considerations outlined in Appendix A, the unnormalized eigenstates of this Hamiltonian are planewaves of the form $\psi(\phi) = e^{ik\phi}$ with wavenumbers and energies taking the form:

$$k = -\frac{\Phi}{\Phi_L} \pm \sqrt{\frac{E}{E_{rot}}} \tag{2.2}$$

$$E = E_{rot}\left(k + \frac{\Phi}{\Phi_L}\right)^2 = \frac{\hbar^2}{2mb^2}\left(k + \frac{\Phi}{\Phi_L}\right)^2 \tag{2.3}$$

where we have introduced the quantum flux $\Phi_L = \frac{2\pi\hbar c}{e}$ and the energy corresponding to the first rotational mode $E_{rot} = \frac{\hbar^2}{2mb^2}$.

The additional term found in the expression of the wavevector(2.2) has the interpretation of an accumulated phase that the electron will acquire as it travels through the ring. This phase can be used to build interferometers through quantum coherence, which is especially relevant when considering transmission problems.

2.2 Aharonov Bohm effect in a 1D Quantum Ring with Rashba Spin-Orbit Interaction

If we now include Spin-Orbit Interaction, the Hamiltonian of a one-dimensional ring of radius b is given by:

$$\hat{H} = \frac{\hbar^2}{2mb^2}\left(-i\frac{\partial}{\partial\phi} + \frac{\Phi}{\Phi_L}\right)^2 + \frac{\alpha}{b}\left(\sigma_x cos(\phi) + \sigma_y sin(\phi)\right)\left(-i\frac{\partial}{\partial\phi} + \frac{\Phi}{\Phi_L}\right) - i\frac{\alpha}{2b}\left(\sigma_y cos(\phi) - \sigma_x sin(\phi)\right) \tag{2.4}$$

where Φ is the magnetic flux , $\Phi_L = \frac{2\pi\hbar c}{e}$ is the quantum flux, α is the Rashba SO constant and σ_x and σ_y are the Pauli matrices.

The expression can be simplified by introducing the parameters $E_{rot} = \frac{\hbar^2}{2mb^2}$, $\Omega = E_{rot}/\hbar$ and $\omega_{so} = \frac{\alpha}{\hbar b}$ and the Pauli matrices in cylindrical coordinates $\sigma_r = \sigma_x cos(\phi) + \sigma_y sin(\phi)$ and $\sigma_\phi = \sigma_y cos(\phi) - \sigma_x sin(\phi)$, together with some manipulations that are specified in Appendix B.

$$\hat{H} = E_{rot}\left(-i\frac{\partial}{\partial\phi} + \frac{\Phi}{\Phi_L} + \frac{\omega_{so}}{2\Omega}\sigma_r\right)^2 \tag{2.5}$$

Given our Hamiltonian (2.5), we can find the energies and eigenstates by diagonalizing the corresponding matrix problem. As earlier, the full solution can be found in Appendix B. The relationship between wavenumber and energy and the unnormalized eigenstates are found to be

$$k^{(\mu)} = -\frac{\Phi}{\Phi_L} + \frac{\Phi_{AC}^{(\mu)}}{2\pi} \pm \sqrt{\frac{E}{E_{rot}}} \tag{2.6}$$

$$\psi^{(\mu)}(\phi) = e^{ik\phi}\chi^{(\mu)}(\phi) \tag{2.7}$$

with $\mu = 1, 2$, $\Phi_{AC}^{(\mu)} = -2\pi\left(\frac{1}{2} + (-1)^{\mu}\sqrt{\frac{1}{4} + \frac{\omega_{so}^2}{4\Omega^2}}\right)$ being the Aharanov-Casher phase and $\chi^{(\mu)}(\phi)$ the mutually orthogonal spinors that in the S_z basis take the form:

$$\chi^{(1)}(\phi) = \frac{1}{\sqrt{2\left(\omega_{so}/2\Omega\right)^2 - \Phi_{AC}^{(2)}/2\pi}} \begin{pmatrix} -\Phi_{AC}^{(2)}/2\pi \\ -\omega_{so}/2\Omega \cdot e^{i\phi} \end{pmatrix} \tag{2.8}$$

$$\chi^{(2)}(\phi) = \frac{1}{\sqrt{2\left(\omega_{so}/2\Omega\right)^2 - \Phi_{AC}^{(2)}/2\pi}} \begin{pmatrix} \omega_{so}/2\Omega \\ -\Phi_{AC}^{(2)}/2\pi \cdot e^{i\phi} \end{pmatrix}. \tag{2.9}$$

With the above results we can see that due to the presence of Spin Orbit Interaction, electrons acquire an additional phase as they travel through the ring, with each spin state in the ring having different phases.

2.2.1 Spin Flip

It is a well known result that spin-orbit interaction changes the probability of finding the particle in a certain spin state as it moves.

First we will mention that diagonalization of the Hamiltonian 2.5 for the case of no SOI ($\omega_{so} = 0$), yields as eigenvectors $\begin{pmatrix} 1 \\ 0 \end{pmatrix}$ and $\begin{pmatrix} 0 \\ 1 \end{pmatrix}$, which are the eigenvectors of the σ_z Pauli Matrix. This means that SOI changes the possible spin states, which will have an effect on the measurement of spin in the $\begin{pmatrix} 1 \\ 0 \end{pmatrix}$ and $\begin{pmatrix} 0 \\ 1 \end{pmatrix}$ basis.

To further study this effect we will consider a particle that is at position $\phi = 0$ with spin-up (i.e. its spin state is described by $\begin{pmatrix} 1 \\ 0 \end{pmatrix}$). We will now project this state into the basis of spin in the ring given by the eigenvectors of the Hamiltonian.

$$\begin{pmatrix} 1 \\ 0 \end{pmatrix} = \frac{c_1}{\sqrt{2\left(\omega_{so}/2\Omega\right)^2 - \Phi_{AC}^{(2)}/2\pi}} \begin{pmatrix} -\Phi_{AC}^{(2)}/2\pi \\ -\omega_{so}/2\Omega \end{pmatrix} + \frac{c_2}{\sqrt{2\left(\omega_{so}/2\Omega\right)^2 - \Phi_{AC}^{(2)}/2\pi}} \begin{pmatrix} \omega_{so}/2\Omega \\ -\Phi_{AC}^{(2)}/2\pi \end{pmatrix}. \tag{2.10}$$

We can find the coefficients c_1 and c_2 by solving a linear system of equations. The solution of such system yields the result:

$$c_1 = \frac{\beta}{\alpha^2 + \beta^2}\sqrt{2\alpha^2 + \beta}, c_2 = \frac{\alpha}{\alpha^2 + \beta^2}\sqrt{2\alpha^2 + \beta} \tag{2.11}$$

where we have introduced the parameters $\alpha = \omega_{so}/2\Omega$ and $\beta = 1/2 - \sqrt{1/4 + \omega_{so}^2/4\Omega^2}$.
With the above result we can now write the state of a particle with a certain fixed energy.

$$\begin{aligned} \psi &= \frac{c_1}{\sqrt{2\alpha^2 + \beta}} e^{ik^{(1)}\phi}\chi^{(1)}(\phi) + \frac{c_2}{\sqrt{2\alpha^2 + \beta}} e^{ik^{(2)}}\chi^{(2)}(\phi) = \qquad (2.12) \\ &= \left[\frac{\alpha^2 e^{-i\beta\phi}}{\alpha^2 + \beta^2} + \frac{\beta^2 e^{i(\beta-1)\phi}}{\alpha^2 + \beta^2}\right] e^{i(-\frac{\Phi}{\Phi_L} \pm k_o)\phi} \begin{pmatrix} 1 \\ 0 \end{pmatrix} + \left[\frac{\alpha\beta e^{-i(\beta-1)\phi}}{\alpha^2 + \beta^2} - \frac{\alpha\beta e^{i\beta\phi}}{\alpha^2 + \beta^2}\right] e^{i(-\frac{\Phi}{\Phi_L} \pm k_o)\phi} \begin{pmatrix} 0 \\ 1 \end{pmatrix} \end{aligned}$$

Hence, the probability of finding the particle in each spin state is given by:

$$P_{up}(\phi) = \left|\frac{\alpha^2 e^{-i\beta\phi}}{\alpha^2 + \beta^2} + \frac{\beta^2 e^{i(\beta-1)\phi}}{\alpha^2 + \beta^2}\right|^2 = \frac{2\beta^2 + 2(\beta-1)\beta\cos(\phi - 2\beta\phi) - 2\beta + 1}{(1-2\beta)^2} \tag{2.13}$$

$$P_{down}(\phi) = \left|\frac{\alpha\beta e^{-i(\beta-1)\phi}}{\alpha^2 + \beta^2} - \frac{\alpha\beta e^{i\beta\phi}}{\alpha^2 + \beta^2}\right|^2 = \frac{4(\beta-1)\beta\sin^2\left(\frac{1}{2}(\phi - 2\beta\phi)\right)}{(1-2\beta)^2} \tag{2.14}$$

In this result, we can see how the probability of finding the particle in one spin or another changes with the angular coordinate ϕ. This allows for the spin to flip from one state to another as the particle is in motion inside the ring. This allows thermoelectric properties to be different for different spin states as there will be different transmission for up and down-electrons.

In Fig.1 we can see how the spin is originally in the up-state but probabilities begin changing sinusoidally as the particle moves. Total spin-flip does not happen though, since $P_{up} > 0$ always.

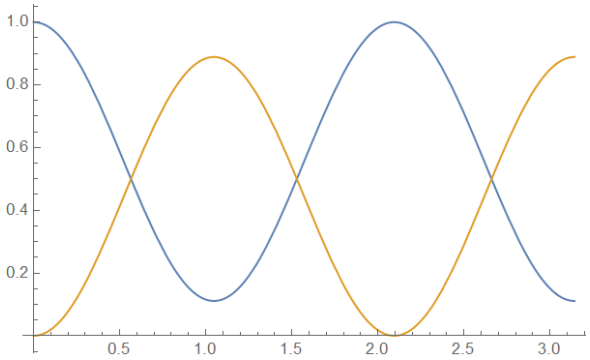

Figure 1: Probability of the particle being in the up (blue) or down (yellow) states versus ϕ with $\beta = 2$.

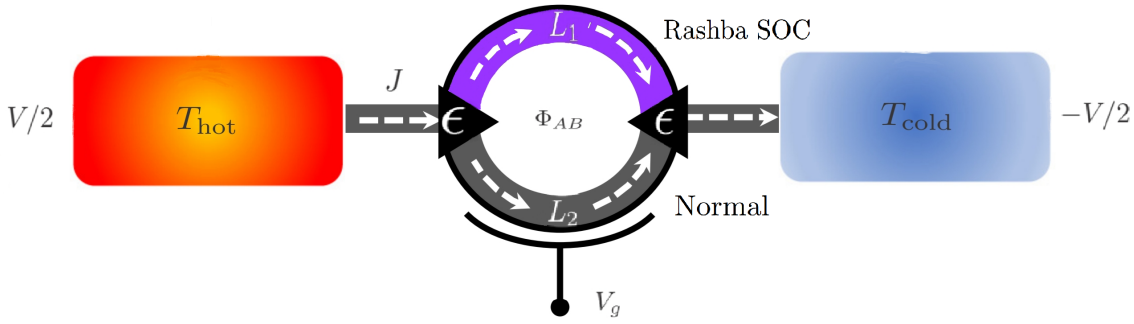

Figure 2: Scheme of the two-terminal Aharonov-Bohm (AB) quantum heat engine. L_1 and L_2 denote the lengths of the arms of the interferometer, with the top arm having Rashba Spin Orbit Coupling, T_{hot} and T_{cold} are the temperatures of the hot and cold reservoirs, Φ_{AB} is the magnetic flux piercing the loop, V_g is the gate voltage, and J is the heat current flowing through the system. Transmission from the leads to the AB ring goes through T junctions, parametrized by ϵ whose value ranges from 0 to 1/2.

2.3 Scattering in a 1D Quantum Ring with AB and SOI

We will use the previous results to find the transmission coefficient of a mesoscopic ring that is connected to two fermionic reservoirs by two leads (Fig 2). Our set-up is the AB interferometer proposed in Ref [13] with the introduction of SOI in one of the arms.

Transmission from the leads to the AB ring is parameterized by the quantity ϵ whose value can range from 0 (i.e. fully disconnected ring) to 1/2 (i.e. fully transmitting junction). The ring is divided into two sections: the top arm of the ring has Rashba Spin Orbit Interaction, while the bottom is coupled to a gate electrode applying an additional gate voltage V_g. The asymmetry in the ring is further increased by having arms of different lengths ($L_1 = L + \delta L$ and $L_2 = L$, being δL the length difference between the arms).

Transmission will depend on energy through the kinematic phase that the electron acquires by travelling along each half of the ring. Electrons moving through the top arm acquire a phase $k_1(\pi+\theta)$, while electrons moving through the bottom arm acquire a phase $k_2(\pi-\theta)$. By linearizing around the Fermi Energy, μ, and taking into account tuning of the Fermi wave vector ($k_\mu \to \tilde{k}_\mu$) and the gate voltage applied to the second arm, the wave number for each of the arms is given by:

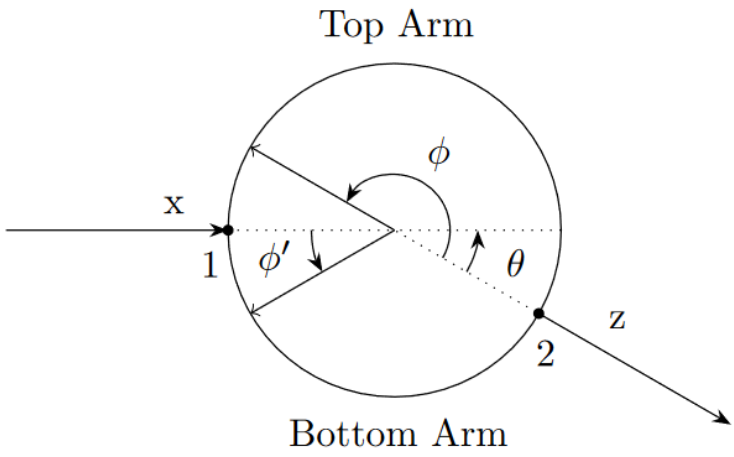

Figure 3: Device geometry and the local coordinates (x, z, ϕ, ϕ') that parameterize different parts of the ring.

$$\frac{k_1}{b}(E) = \tilde{k}_\mu + \frac{E-\mu}{\hbar v_d} \tag{2.15}$$

$$\frac{k_2}{b}(E) = \tilde{k}_\mu + \frac{E-(\mu+eV_g)}{\hbar v_d} \tag{2.16}$$

The left lead is associated to a local coordinate x, with $x = 0$ corresponding to the left junction. The chosen basis of wavefunctions in this region are plane waves of the form $e^{\pm ik_x x}$, with positive wavevectors indicating that the wave is travelling into the ring and negative wavevectors indicating that the wave is travelling out of the ring.

In the same way, the right lead is associated to a local coordinate z, with $z = 0$ corresponding to the right junction. The basis in this region will be planewaves (i.e. $e^{\pm ik_z z}$) with positive wavevectors indicating that the wave is travelling out of the ring and negative wavevectors indicating that the wave is travelling into the ring.

Since the two leads break the symmetry of the problem, we will have to consider separately the top and bottom halves of the ring separately. Length in the top half will be parameterized by an angular coordinate $\phi\ \epsilon[0, \pi + \theta]$ that grows in the anticlockwise direction. $\phi = 0$ corresponds to the right junction, while $\phi = \pi + \theta$ corresponds to the left junction. On the other hand, the local coordinate in the bottom half is $\phi'\ \epsilon[0, \pi - \theta]$, with $\phi' = 0$ corresponding to the left junction and $\phi' = \pi - \theta$ corresponding to the right junction. Hence, ϕ' also grows in the anticlockwise direction. Since we have a circular ring the angle θ will be:

$$\theta = \frac{\delta L}{2L + \delta L}\pi \tag{2.17}$$

To use the scattering matrix formalism, we need to find the incoming and outgoing waves in each of the nodes. To do so we will begin by finding how a wavefunction in the top-half of the ring can be expressed as a function of the eigenstates of its Hamiltonian.

$$\begin{aligned}
\psi_T &= \left(c_1 e^{ik_1\phi} + c_3 e^{-ik_1\phi}\right) e^{i\left(-\Phi/\Phi_L + \Phi_{AC}^{(1)}/2\pi\right)\phi} \chi^{(1)}(\phi) + \left(c_2 e^{ik_1\phi} + c_4 e^{-ik_1\phi}\right) e^{i\left(-\Phi/\Phi_L + \Phi_{AC}^{(2)}/2\pi\right)\phi} \chi^{(2)}(\phi) = \\
&= \frac{\left(c_1 e^{ik_1\phi} + c_3 e^{-ik_1\phi}\right)}{\sqrt{2\left(\omega_o/2\Omega\right)^2 - \Phi_{AC}^{(2)}/2\pi}} e^{i\left(-\Phi/\Phi_L + \Phi_{AC}^{(1)}/2\pi\right)\phi} \begin{pmatrix} -\Phi_{AC}^{(2)}/2\pi \\ -\omega_o/2\Omega \cdot e^{i\phi} \end{pmatrix} + \\
&+ \frac{\left(c_2 e^{ik_1\phi} + c_4 e^{-ik_1\phi}\right)}{\sqrt{2\left(\omega_o/2\Omega\right)^2 - \Phi_{AC}^{(2)}/2\pi}} e^{i\left(-\Phi/\Phi_L + \Phi_{AC}^{(2)}/2\pi\right)\phi} \begin{pmatrix} \omega_o/2\Omega \\ -\Phi_{AC}^{(2)}/2\pi \cdot e^{i\phi} \end{pmatrix}.
\end{aligned} \tag{2.18}$$

This expression can be recasted into a form where the motion of the up and down spin-states is more obvious:

$$
\begin{aligned}
\psi_T \;=\; & \frac{\left[\left(-\Phi_{AC}^{(2)}/2\pi\right) c_1 e^{i\left(\Phi_{AC}^{(1)}/2\pi\right)\phi} + \left(\omega_o/2\Omega\right) c_2 e^{i\left(\Phi_{AC}^{(2)}/2\pi\right)\phi}\right]}{\sqrt{2\left(\omega_o/2\Omega\right)^2 - \Phi_{AC}^{(2)}/2\pi}} e^{i(-\Phi/\Phi_L+k_1)\phi}\begin{pmatrix}1\\0\end{pmatrix} + \\
& + \frac{\left[\left(-\omega_o/2\Omega\right) c_1 e^{i\left(\Phi_{AC}^{(1)}/2\pi+1\right)\phi} + \left(-\Phi_{AC}^{(2)}/2\pi\right) c_2 e^{i\left(\Phi_{AC}^{(2)}/2\pi+1\right)\phi}\right]}{\sqrt{2\left(\omega_o/2\Omega\right)^2 - \Phi_{AC}^{(2)}/2\pi}} e^{i(-\Phi/\Phi_L+k_1)\phi}\begin{pmatrix}0\\1\end{pmatrix} + \\
& + \frac{\left[\left(-\Phi_{AC}^{(2)}/2\pi\right) c_3 e^{i\left(\Phi_{AC}^{(1)}/2\pi\right)\phi} + \left(\omega_o/2\Omega\right) c_4 e^{i\left(\Phi_{AC}^{(2)}/2\pi\right)\phi}\right]}{\sqrt{2\left(\omega_o/2\Omega\right)^2 - \Phi_{AC}^{(2)}/2\pi}} e^{i(-\Phi/\Phi_L-k_1)\phi}\begin{pmatrix}1\\0\end{pmatrix} + \\
& + \frac{\left[\left(-\omega_o/2\Omega\right) c_3 e^{i\left(\Phi_{AC}^{(1)}/2\pi+1\right)\phi} + \left(-\Phi_{AC}^{(2)}/2\pi\right) c_4 e^{i\left(\Phi_{AC}^{(2)}/2\pi+1\right)\phi}\right]}{\sqrt{2\left(\omega_o/2\Omega\right)^2 - \Phi_{AC}^{(2)}/2\pi}} e^{i(-\Phi/\Phi_L-k_1)\phi}\begin{pmatrix}0\\1\end{pmatrix}.
\end{aligned}
\tag{2.19}
$$

The same can be done with the bottom half of the ring. Since we have no SOI, we can use directly the Sz basis and planewaves with wavenumber k_2.

$$
\begin{aligned}
\psi_B \;=\; & c_5 e^{i(-\Phi/\Phi_L+k_2)\phi'}\begin{pmatrix}1\\0\end{pmatrix} + c_6 e^{i(-\Phi/\Phi_L+k_2)\phi'}\begin{pmatrix}0\\1\end{pmatrix} + \\
& + c_7 e^{i(-\Phi/\Phi_L-k_2)\phi'}\begin{pmatrix}1\\0\end{pmatrix} + c_8 e^{i(-\Phi/\Phi_L-k_2)\phi'}\begin{pmatrix}0\\1\end{pmatrix}.
\end{aligned}
\tag{2.20}
$$

To find the reflection and transmission coefficients, we will use the Landauer-Büttiker formalism, where the amplitudes of in-going and outgoing waves at a junction are related linearly through a product with the scattering matrix. Since with SOI, we lose symmetry in the spin, we must take into account separately the amplitudes of wavefunctions for spin up and down. Therefore, we must relate the in-going and out-going waves as:

$$
\begin{pmatrix}\psi_{Lead}^{\uparrow}\\ \psi_{Lead}^{\downarrow}\\ \psi_T^{\uparrow}\\ \psi_T^{\downarrow}\\ \psi_B^{\uparrow}\\ \psi_B^{\downarrow}\end{pmatrix}_{out} = \hat{\$}\begin{pmatrix}\psi_{Lead}^{\uparrow}\\ \psi_{Lead}^{\downarrow}\\ \psi_T^{\uparrow}\\ \psi_T^{\downarrow}\\ \psi_B^{\uparrow}\\ \psi_B^{\downarrow}\end{pmatrix}_{in}
\tag{2.21}
$$

Since we have a symmetrical scattering problem, the scattering matrices for the left and right junctions should be the same and given by [14]:

$$
\hat{\$} = \begin{pmatrix}
-\sqrt{1-2\epsilon} & 0 & \sqrt{\epsilon} & 0 & \sqrt{\epsilon} & 0\\
0 & -\sqrt{1-2\epsilon} & 0 & \sqrt{\epsilon} & 0 & \sqrt{\epsilon}\\
\sqrt{\epsilon} & 0 & a & 0 & b & 0\\
0 & \sqrt{\epsilon} & 0 & a & 0 & b\\
\sqrt{\epsilon} & 0 & b & 0 & a & 0\\
0 & \sqrt{\epsilon} & 0 & b & 0 & a
\end{pmatrix}
\tag{2.22}
$$

where $a = \frac{1}{2}\left(\sqrt{1-2\epsilon}-1\right)$ and $b = \frac{1}{2}\left(\sqrt{1-2\epsilon}+1\right)$.

2.3.1 Scattering on the Left Junction

We will consider that a plane wave of amplitude is incident to the AB ring through the left lead, with $i^{\uparrow}$ being the amplitude of this incident wave with spin up and $i^{\downarrow}$ being the amplitude of the wave with spin down. As a result, there will be a reflected wave in the left lead, with amplitudes $r^{\uparrow}$ and $r^{\downarrow}$ for the corresponding spin states. Meanwhile, on the ring, there will be waves going in

and out of the junction in both halves. Waves in the top half must be evaluated at $\phi = \pi + \theta$ and waves in the bottom half at $\phi' = 0$. The scattering problem on the left junction is then:

$$\begin{pmatrix} r^{\uparrow} \\ r^{\downarrow} \\ \frac{\left[\beta c_3 e^{i(\beta-1)(\pi+\theta)} + \alpha c_4 e^{-i\beta(\pi+\theta)}\right]}{\sqrt{2\alpha^2+\beta}} e^{i(-\Phi/\Phi_L - k_1)(\pi+\theta)} \\ \frac{\left[-\alpha c_3 e^{i\beta(\pi+\theta)} + \beta c_4 e^{-i(\beta-1)(\pi+\theta)}\right]}{\sqrt{2\alpha^2+\beta}} e^{i(-\Phi/\Phi_L - k_1)(\pi+\theta)} \\ c_5 \\ c_6 \end{pmatrix}_{out} = \hat{\mathbb{S}} \begin{pmatrix} i^{\uparrow} \\ i^{\downarrow} \\ \frac{\left[\beta c_1 e^{i(\beta-1)(\pi+\theta)} + \alpha c_2 e^{-i\beta(\pi+\theta)}\right]}{\sqrt{2\alpha^2+\beta}} e^{i(-\Phi/\Phi_L + k_1)(\pi+\theta)} \\ \frac{\left[-\alpha c_1 e^{i\beta(\pi+\theta)} + \beta c_2 e^{-i(\beta-1)(\pi+\theta)}\right]}{\sqrt{2\alpha^2+\beta}} e^{i(-\Phi/\Phi_L + k_1)(\pi+\theta)} \\ c_7 \\ c_8 \end{pmatrix}_{in}, \tag{2.23}$$

where we have introduced $\alpha = \omega_o/2\Omega$ and $\beta = -\Phi^{(2)}_{AC}/2\pi$.

2.3.2 Scattering on the Right Junction

In the right lead, we will consider that there is only the transmitted wave (i.e. there is no wave going into the ring through the right lead) with amplitudes $t^{\uparrow}$ and $t^{\downarrow}$ for the corresponding spin states. Again, in the ring, there will be waves travelling in and out of the junction. Waves in the top half must be evaluated at $\phi = 0$ and waves in the bottom half at $\phi' = \pi - \theta$. Hence, we arrive at the equation for the right junction:

$$\begin{pmatrix} t^{\uparrow} \\ t^{\downarrow} \\ \frac{(\beta c_1 + \alpha c_2)}{\sqrt{2\alpha^2+\beta}} \\ \frac{(-\alpha c_1 + \beta c_2)}{\sqrt{2\alpha^2+\beta}} \\ c_7 e^{i(-\Phi/\Phi_L - k_o)(\pi-\theta)} \\ c_8 e^{i(-\Phi/\Phi_L - k_o)(\pi-\theta)} \end{pmatrix}_{out} = \hat{\mathbb{S}} \begin{pmatrix} 0 \\ 0 \\ \frac{(\beta c_3 + \alpha c_4)}{\sqrt{2\alpha^2+\beta}} \\ \frac{(-\alpha c_3 + \beta c_4)}{\sqrt{2\alpha^2+\beta}} \\ c_5 e^{i(-\Phi/\Phi_L + k_o)(\pi-\theta)} \\ c_6 e^{i(-\Phi/\Phi_L + k_o)(\pi-\theta)} \end{pmatrix}_{in}. \tag{2.24}$$

2.4 Thermoelectric Properties

In our work we try to study the thermoelectric performances in the linear response regime of the Aharanov-Bohm ring in the presence of spin-orbit interaction. The interesting feature of this device is that the transmission contains spin-flip terms as $T_{\uparrow\downarrow}$ and $T_{\downarrow\uparrow}$ in which the second index is the injected spin and the first one is the outgoing spin channel. Therefore, the electrical conductance at zero temperature for $\uparrow$ channel is simply

$$G_{\uparrow} = \frac{e^2}{h} \left(T_{\uparrow\downarrow}(E_F) + T_{\uparrow\uparrow}(E_F)\right) \tag{2.25}$$

Similarly

$$G_{\downarrow} = \frac{e^2}{h} \left(T_{\uparrow\downarrow}(E_F) + T_{\downarrow\downarrow}(E_F)\right) \tag{2.26}$$

In the finite temperature case these expressions have to replaced by the following

$$G_{\sigma} = \sum_{\sigma'} \frac{e^2}{h} \int T_{\sigma\sigma'}(E) \left(-\frac{\partial f(E)}{\partial E}\right) \tag{2.27}$$

The thermoelectrical conductance in the linear regime are

$$L_{\uparrow} = -\frac{e}{hT_0} \int dE(E - E_F) \left(T_{\uparrow\downarrow}(E) + T_{\uparrow\uparrow}(E)\right) \left(\frac{\partial f(E)}{\partial E}\right) \tag{2.28}$$

where in the zero temperature limit (by using the Sommerfeld expansion) one gets

$$L_{\uparrow} = \frac{e\pi^2 k_B^2}{3h} \left(\frac{\partial T_{\uparrow\downarrow}}{\partial E}|_{E=E_F} + \frac{\partial T_{\uparrow\uparrow}}{\partial E}|_{E=E_F}\right) \tag{2.29}$$

Here T_0 is the background or common temperature. Similarly for $\downarrow$ spins

$$L_{\downarrow} = -\frac{e}{hT_0} \int dE(E - E_F)(T_{\downarrow\uparrow}(E) + T_{\downarrow\downarrow}(E)) \left(\frac{\partial f(E)}{\partial E}\right) \tag{2.30}$$

where in the zero temperature limit (by using the Sommerfeld expansion) one gets

$$L_{\downarrow} = \frac{e\pi^2 k_B^2}{3h}\left(\frac{\partial T_{\downarrow\uparrow}}{\partial E}\bigg|_{E=E_F} + \frac{\partial T_{\downarrow\downarrow}}{\partial E}\bigg|_{E=E_F}\right) \tag{2.31}$$

The charge current is given by

$$I_q = (G_{\uparrow} + G{\downarrow})\delta V + \frac{1}{2}(G_{\uparrow} - G_{\downarrow})\Delta V_s + (L_{\uparrow} + L{\downarrow})\delta T \tag{2.32}$$

The spin current is generated due to the spin flip terms in the transmission, its expression is

$$I_s = (G_{\uparrow} - G{\downarrow})\delta V + \frac{1}{2}(G_{\uparrow} + G_{\downarrow})\Delta V_s + (L_{\uparrow} - L{\downarrow})\delta T \tag{2.33}$$

The Seebeck coefficient can be defined in different manners depending on the electric-thermal configuration. Thus we defined the "classic" Seebeck coefficient as

$$S = -\left(\frac{\Delta V}{\Delta T}\right)\bigg|_{I_q=0,\Delta V_s=0} \tag{2.34}$$

This is the voltage generated in the junction in response to a temperature shift. In this case, the analytical expression for S is easy to get as

$$S = \frac{L_{\uparrow} + L_{\downarrow}}{G_{\uparrow} + G_{\downarrow}} \tag{2.35}$$

With this definition and the expressions for the thermoelectric properties, it is clear to see that the Seebeck coefficient strongly depends on the symmetry of the transmission coefficients with respect to the energy (i.e. it vanishes in the symmetric case). Hence, introducing adequate values of gate voltage, spin-orbit interaction and length difference are vital to obtain a better thermoelectric performance.

Applied temperature gradients can also lead to spin accumulations in the attached leads driven by spin Seebeck effects. Then, it is natural to ask whether a local spin-orbit in- teraction leads to different spin occupations. We then calculate the spin bias ΔV_s generated when $I_q = 0$ and $I_s = 0$ but $\Delta T = 0$. In this case we have

$$S_s = -\left(\frac{\Delta V_s}{\Delta T}\right)\bigg|_{I_q=0,I_s=0} \tag{2.36}$$

with an explicit expression in terms of linear conductances as

$$S_s = \frac{L_{\uparrow}}{G_{\uparrow}} - \frac{L_{\downarrow}}{G_{\downarrow}} \tag{2.37}$$

Notice that this result can be achieved if instead one applies the following electrical bias ΔV as

$$\Delta V = -\frac{1}{2}\left(\frac{L_{\uparrow}}{G_{\uparrow}} + \frac{L_{\downarrow}}{G_{\downarrow}}\right)\Delta T \tag{2.38}$$

In the zero temperature limit the spin Seebeck coefficient reads as

$$S_s = \frac{-\pi^2 k_B^2 T_0}{3e}\frac{\partial \ln T_{\uparrow\downarrow}}{\partial E}|_{E=E_F} \tag{2.39}$$

In the linear response regime, thermal conductivity is given by:

$$K = -\frac{1}{hT_0}\int dE(E - E_F)^2\left(T_{\uparrow\downarrow}(E) + T_{\uparrow\uparrow}(E) + T_{\downarrow\uparrow} + T_{\downarrow\downarrow}\right)\left(\frac{\partial f(E)}{\partial E}\right) \tag{2.40}$$

The thermal conductance of the ring can then be calculated as:

$$k_{th} = \left(K - S^2(G_{\uparrow} + G_{\downarrow})T\right) \tag{2.41}$$

3 Results and discussion

Transmission coefficients were calculated by solving the Scattering Problem with Mathematica. All results presented here use the realistic values for the problem parameters present in Table 1, unless it is specified otherwise.

In our results SOI is characterized by the quantity $\eta = \beta - 1 = \Phi^{(1)}_{AC}/2\pi$, with $\eta = 0$ corresponding to $\alpha = 0$.

Table 1: Values of transmissivity, length, asymmetry, gate voltage, magnetic flux, Wave Vector offset, drift velocity and temperature used to obtain most results.

ϵ	0.1
L	$2 \times 10^{-6} m$
$\delta L/L$	0.3
eV_g	$2\pi\mu/5$
Φ/Φ_l	$1/14$
$\tilde{k}_\mu$	$\sqrt{\pi}k_\mu$
v_d	$10^6 m/s$
T	$500mK$

3.1 Energy Dependence of the Transmission Coefficient

To achieve the maximum possible thermopower we have to fix ϵ, the parameter that characterizes the transmission from the leads that connect the fermionic reservoirs to the arms of the ring. In Fig 4 we distinguish between two different cases.

Transmission probability is calculated for full transmissivity (i.e. $\epsilon = 0.5$) represented in yellow for a symmetric device (left) and an asymmetric device (right). In the symmetric scenario, the transmission probability appears to be periodic with energy having a very small amplitude. On the other hand, the asymmetric case exhibits a very non-linear behaviour that has really low values of transmission for energies near the Fermi Level, which at a low temperature is the region responsible for transmission. Thus, full transmissivity will not give us optimal performance in our engine.

When transmission in the T junctions is weak (in our case $\epsilon = 0.1$), represented in blue, electrons must excite the resonances in the ring to be transported, hence the repeated spikes when transmission probability is against energy. Optimal properties will be found when there is a high number of spikes around the Fermi Energy for low values of temperature.

It shall be mentioned that the result for the assymetric case matches perfectly Ref [13].

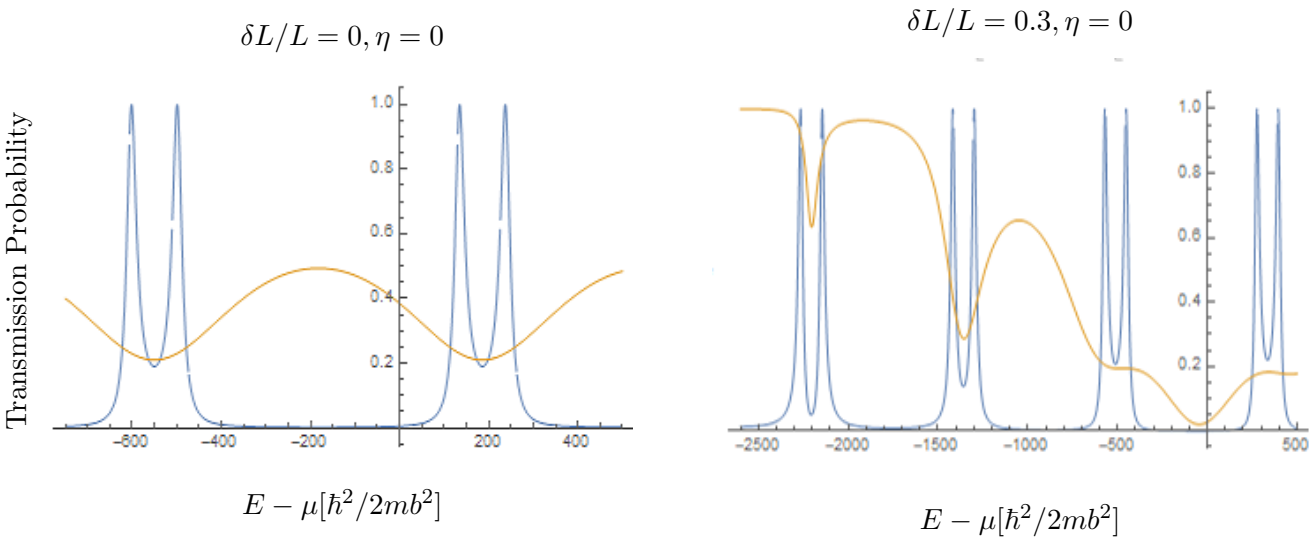

Figure 4: Comparison between the transmission probability versus energy obtained with $\epsilon = 0.1$ (blue) and $\epsilon = 0.5$ (yellow) for a symmetric (left) and asymmetric (right) device.

In our device we have an extra degree of freedom, since we can tune the Rashba Spin Orbit Constant in the top arm by changing the axial electric field. This allows us to obtain different transmission for electrons in different spin states. In Fig 5, we show transmission for ↑-electrons (blue) and ↓-electrons (yellow) for different values of η. The observable difference in the transmission for the two spin-states can allow us to create temperature differences through different concentrations of spins in each fermionic reservioir (Spin-Seebeck Effect) [10].

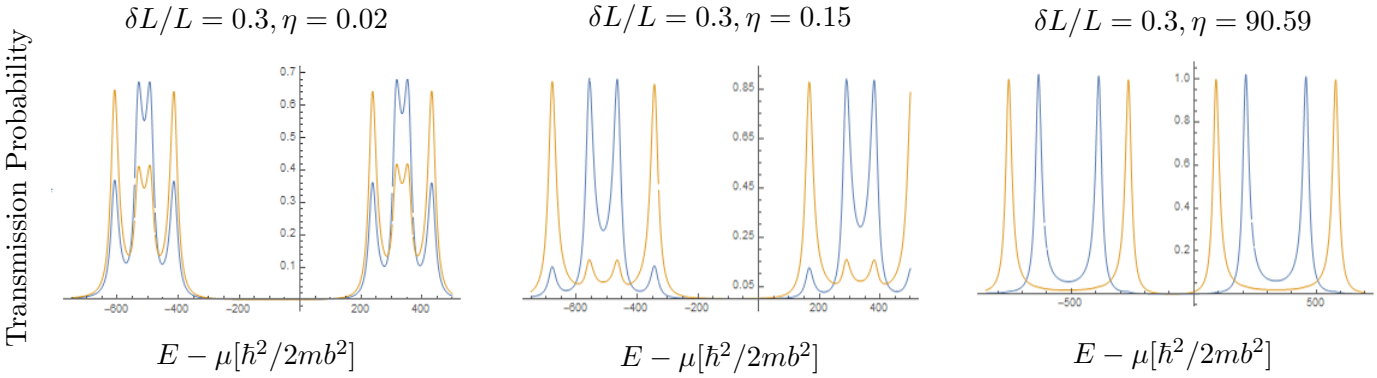

Figure 5: Transmission probability for ↑-electrons $T_\uparrow$ (blue) and ↓-electrons $T_\downarrow$ (yellow) against energy for different values of η.

We shall also investigate what type of behaviour we shall expect for different values of η. In Fig 6 we study how $T_\uparrow$ (blue) and $T_\downarrow$ (yellow) changes as the value η increases for both the usual symmetric and asymmetric devices.

In both cases, we find that for low values of η (top), the behaviour is not periodic, with spike-like peaks. Eventually, for higher values of η (bottom), periodic behaviour arises with the period being equal to $\Delta\eta = 2 - \frac{\delta L}{L+\delta L}$. For the symmetric case we can see that the behaviour appears to be sinusoidal with $T_\uparrow$ and $T_\downarrow$ being 180^o out of phase. Meanwhile, the asymmetric case appears to be more "step-like" with $T_\uparrow$ and $T_\downarrow$ sharing critical points.

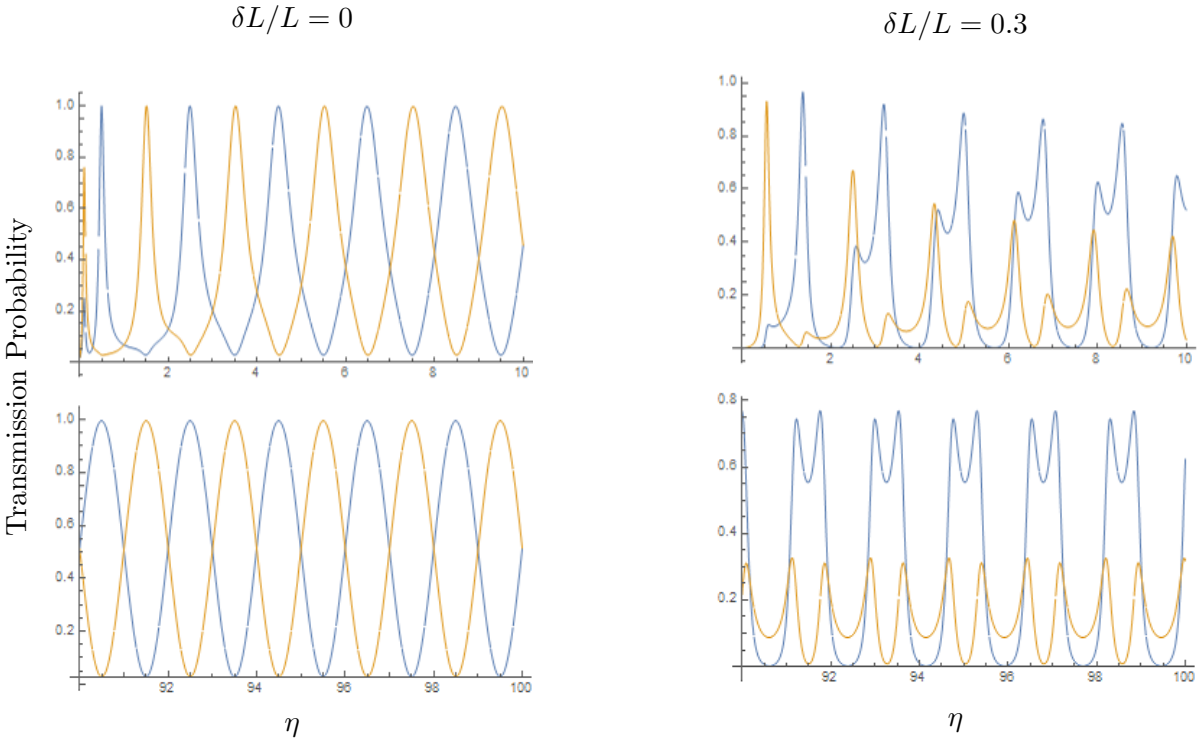

Figure 6: $T_\uparrow$ (blue) and $T_\downarrow$ (yellow) changes as the value η. Distinguishing between low (top) and high (bottom) values of η.

3.2 Charge Thermoelectric Properties

We will now calculate the basic thermoelectric properties to find which parameters of gate voltage, magnetic field, η and assymetry δL allow us to achieve a better thermal performance.

In figures 7 and 8 we show density plots of the electric conductance, thermal conductivity and Seebeck Coefficient versus Φ_{AB} and V_g for the case of no SOI, distinguishing between $\delta L/L = 0$ and $\delta L/L = 0.3$. We can see how in Fig 8 we achieve better thermal conductivity and thermopower, thanks to the additional asymmetry introduced by having a longer top arm.

In these figures we can also observe how the thermal conductivity is not simply proportional to the electric conductance. This means that, unlike for full transmissivity [13], for low values of ϵ the Wiedemann-Franz Law is not satisfied.

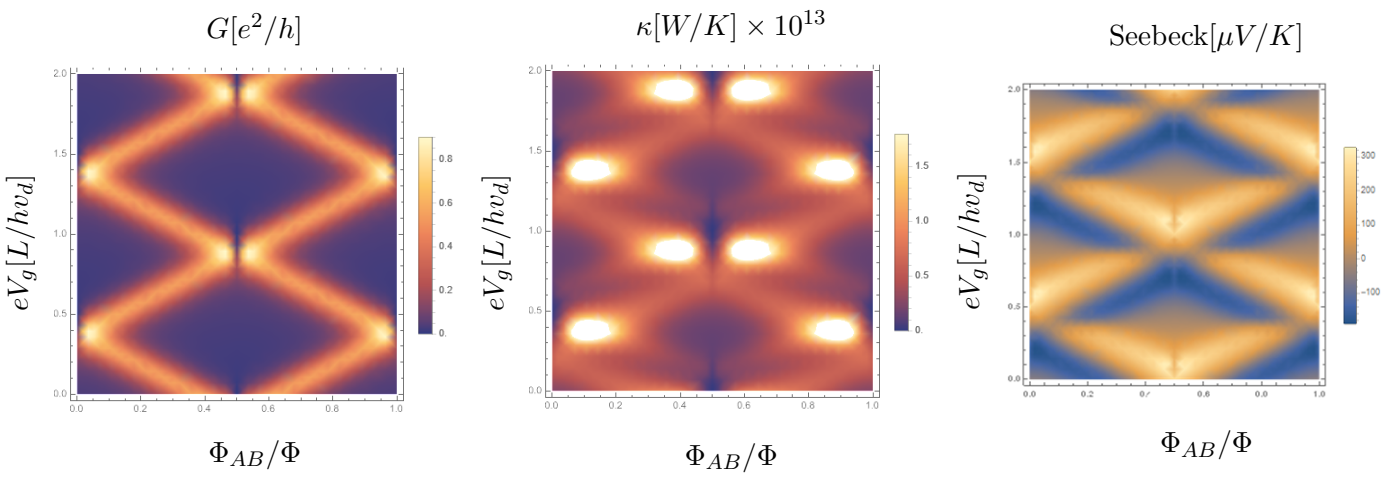

Figure 7: Density plots of the electric conductance, thermal conductivity and Seebeck Coefficient vs magnetic flux Φ_{AB} and gate voltage V_g for $\eta = \beta - 1 = 0$ and $\delta L/L = 0$.

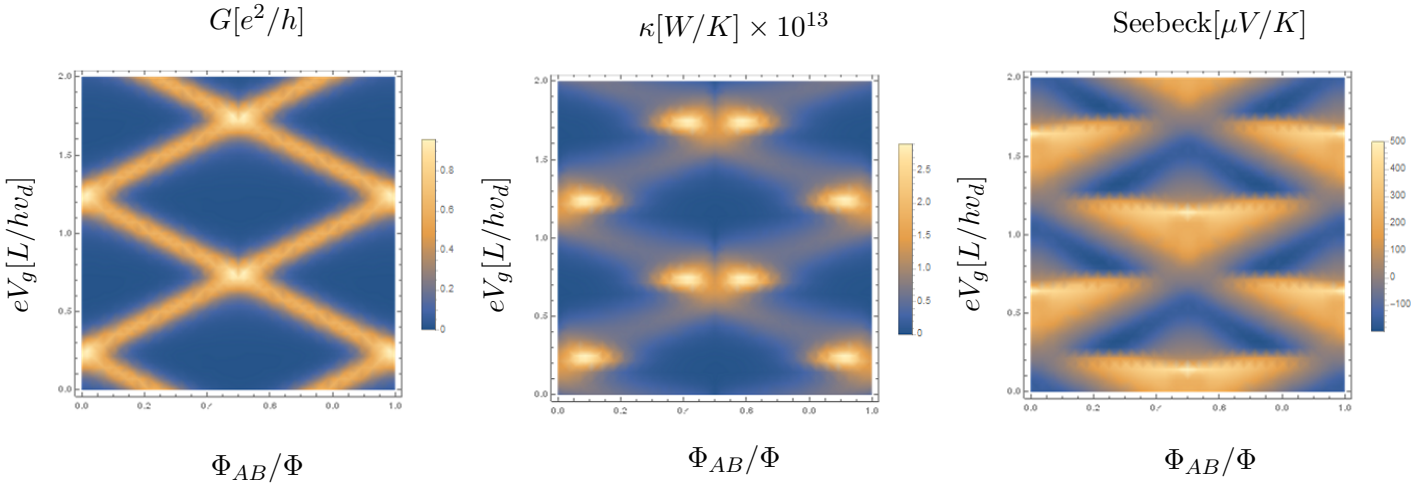

Figure 8: Density plots of the electric conductance, thermal conductivity and Seebeck Coefficient vs magnetic flux Φ_{AB} and gate voltage V_g for $\eta = \beta - 1 = 0$ and $\delta L/L = 0.3$.

In figures 9,10 and 11 we show the same thermoelectric properties but now varying the value of η. In all cases, we can see how the maximum values are achieved for a magnetic flux $\Phi_{AB} = 0$ and $\Phi_{AB} = \Phi_L/2$. We can also see how the maximum values of these quantities decrease and begin to form different periodic patterns.

3.3 Spin Thermoelectric Properties

In Fig 12 we show the density plots of the electric conductance for each spin channel for the case of no SOI. Evidently, we obtain that they are the same and are half of what was found in Fig 8.

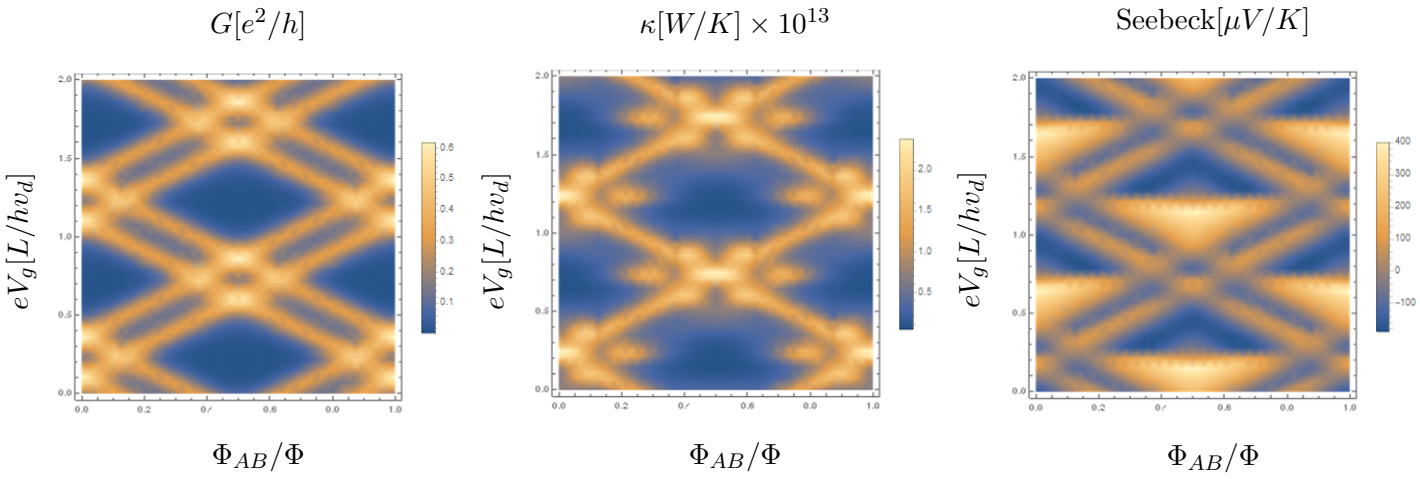

Figure 9: Density plots of the electric conductance, thermal conductivity and Seebeck Coefficient vs magnetic flux Φ_{AB} and gate voltage V_g for $\eta = \beta - 1 = 0.15$ and $\delta L/L = 0.3$.

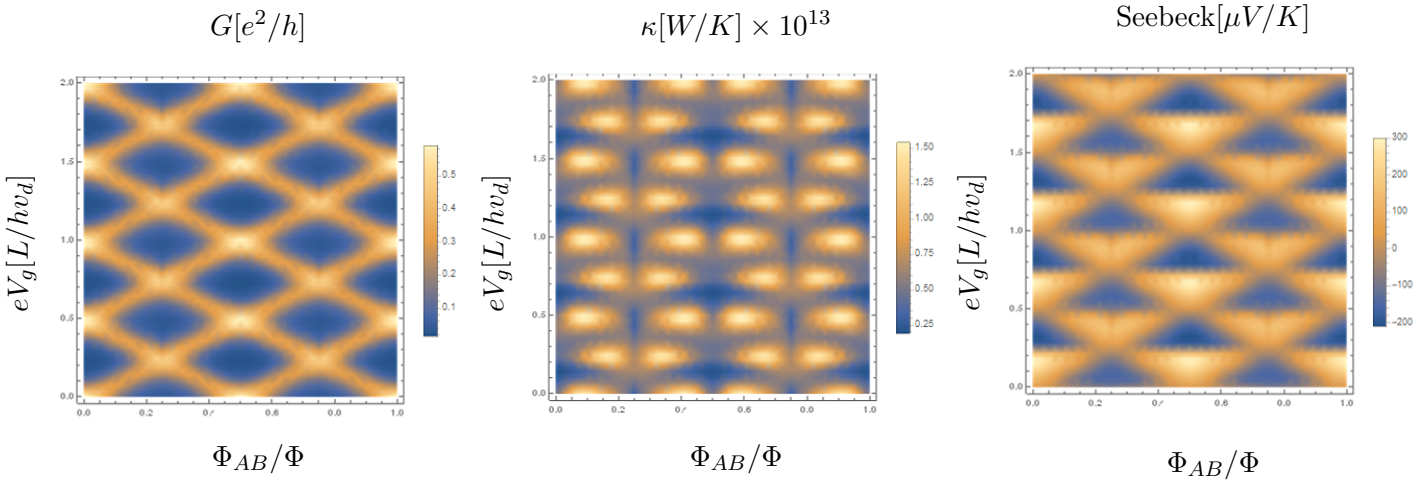

Figure 10: Density plots of the electric conductance, thermal conductivity and Seebeck Coefficient vs magnetic flux Φ_{AB} and gate voltage V_g for $\eta = \beta - 1 = 0.5$ and $\delta L/L = 0.3$.

In figures 13, 14 and 15, we show the density plots of the electric conductance for each spin channel and the Spin-Seebeck Coefficient for different values of η.

As SOI increases, the conductances for each spin become more shifted in terms of the magnetic flux until they acquire a $2\pi\Phi_{AB}/\Phi = \pi/2$ phase difference. This is the explanation on why the charge thermoelectric coefficients decrease their value when having higher values of η.

We can also see that we can obtain a high Spin-Seebeck Coefficient for high values of η, achieving a maximum value of $S_s = 0.4mV/k$ for $\eta = 90.59$ (in the $\eta\epsilon[90, 100]$ range). This result indicates that if we intend to focus on spin-related performances, we must sacrifice thermopower.

3.4 Broken Time-Reversal symmetry

The shift that is experienced in magnetic field for the spin-thermoelectric coefficients is a consequence of having a spin-dependent Hamiltonian, which breaks time-reversal symmetry under a magnetic field (i.e. $J_\sigma(B) \neq J_\sigma(-B)$). In Fig.16 we plot the spin thermal conductances $J_\uparrow$, $J_\downarrow$ and $J_\downarrow$ for a reversed magnetic field. In the figure, it can be seen that, as a result of SOI in the ring, we end up obtaining that $J_\uparrow(B) = J_\downarrow(-B)$. This result is especially interesting since time-reversal symmetry breaking allows heat engines to reach Carnot Efficiency for smaller values of the ZT coefficient [15].

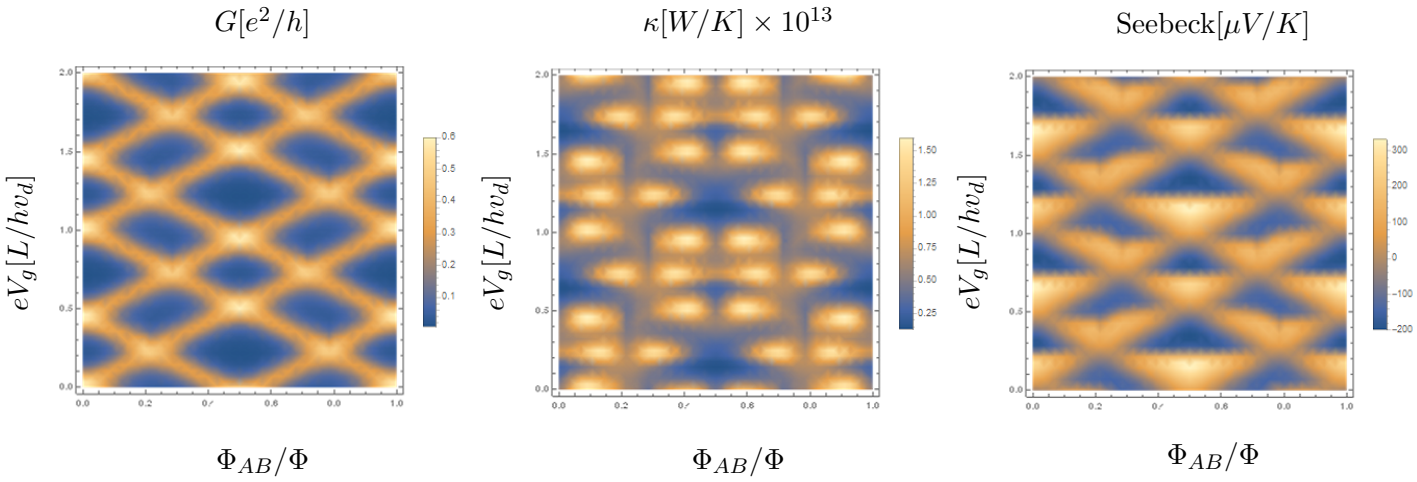

Figure 11: Density plots of the electric conductance, thermal conductivity and Seebeck Coefficient vs magnetic flux Φ_{AB} and gate voltage V_g for $\eta = \beta - 1 = 90.59$ and $\delta L/L = 0.3$.

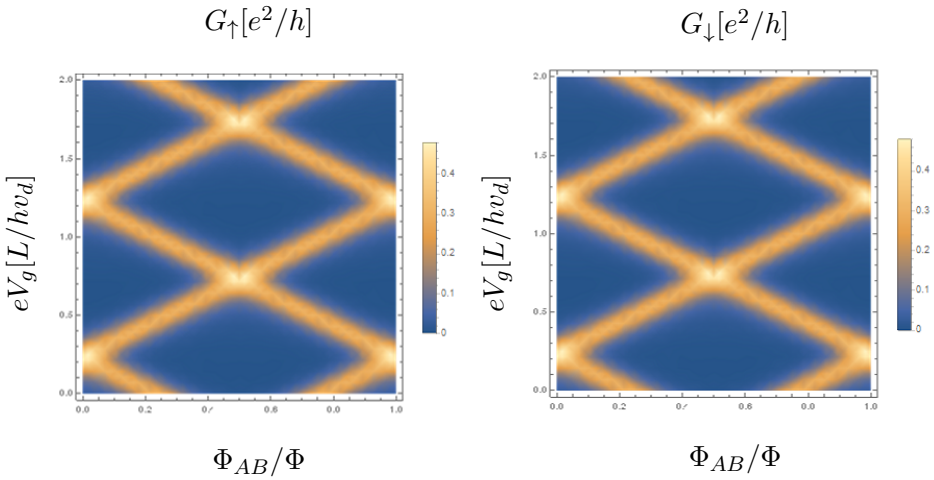

Figure 12: Density plots of the electric conductance for each spin channel versus magnetic flux Φ_{AB} and gate voltage V_g for $\eta = \beta - 1 = 0$ and $\delta L/L = 0.3$.

4 Conclusions

In summary, we have proposed and analyzed a phase- coherent mesoscopic heat engine based on a Aharonov-Bohm quantum interferometer, that includes Rashba SOI in one of its arms. The system can provide sizable thermoelectric response and Spin-Seebeck Coefficient. Under conditions which are easily accessible from the experimental point of view, the heat engine is able to yield full phase and electrostatic control of thermal and electric conductance as well as of its spin equivalents. Furthermore, the breaking of time reversal symmetry opens up the possibility of achieving a thermal machine with very high efficiency. Thus, we have checked that the AB interferometer, is the archetypal quantum platform for the realization of unique phase-tunable heat engines and quantum thermal machines operating at low temperatures [13] and the great range of possibilities that are opened when introducing the spin-degree of freedom which is intrinsic to the quantum realm.

Acknowledgments

This work would not have been possible without the help of my supervisors Rosa López and Misha Moskalets, with whom I have had the honor of working.

This work was supported by the SURF@IFISC fellowship.

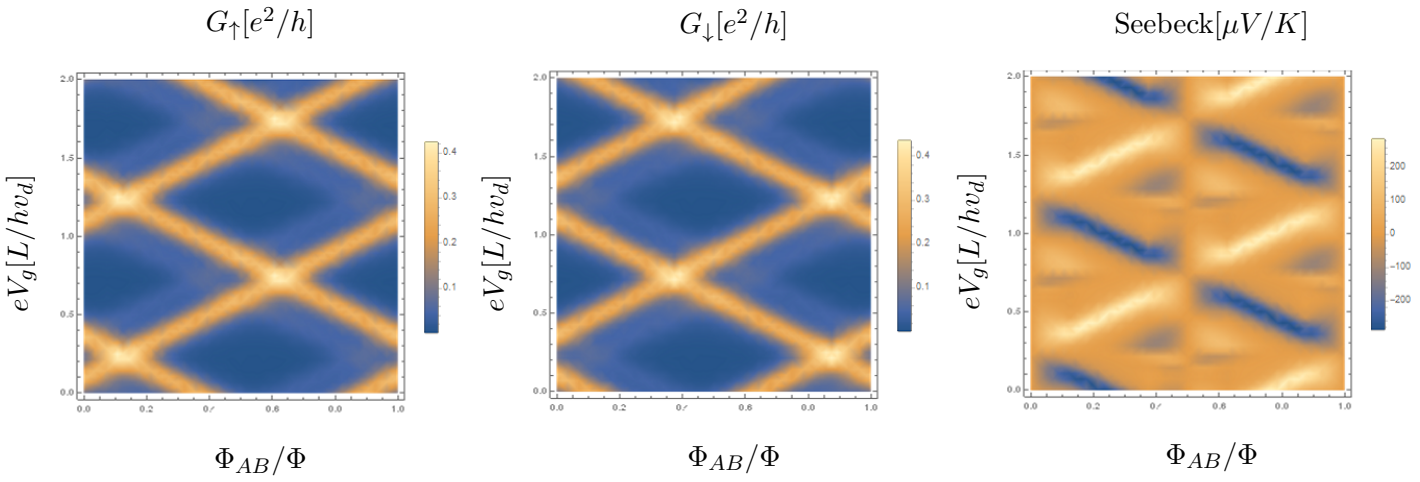

Figure 13: Density plots of the electric conductance for each spin channel and the Spin Seebeck Coefficient versus magnetic flux Φ_{AB} and gate voltage V_g for $\eta = \beta - 1 = 0.15$ and $\delta L/L = 0.3$.

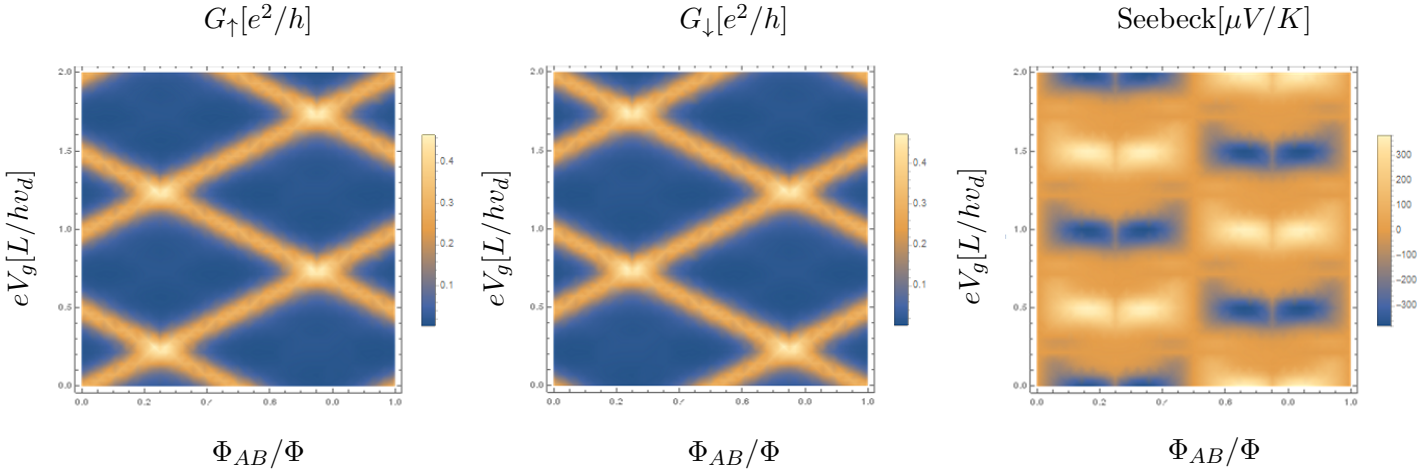

Figure 14: Density plots of the electric conductance for each spin channel and the Spin Seebeck Coefficient versus magnetic flux Φ_{AB} and gate voltage V_g for $\eta = \beta - 1 = 0.5$ and $\delta L/L = 0.3$.

A Aharonov-Bohm Effect in a 1D Quantum Ring

The set-up under study is that of a particle confined in a circle of radius b in the XY plane. An infinitely long solenoid of radius $a < b$ is placed along the z-axis, producing a uniform magnetic field B in the region satisfying $r < a$, while maintaining the region of $r > a$ free of field.
The magnetic flux outside the solenoid, where B=0, can be found as:

$$\Phi = \iint_S \vec{B} \cdot d\vec{S} = \pi a^2 B \tag{A.1}$$

Knowing that the magnetic field can be written in terms of the vector potential $\vec{A}$, as $\vec{B} = \vec{\nabla} \times \vec{A}$. We can use Stokes' theorem to give the vector potential in terms of the magnetic flux.

$$\Phi = \iint_S \vec{B} \cdot d\vec{S} = \oint_{\partial S} \vec{A} \cdot d\vec{l} = 2\pi b A_\phi \tag{A.2}$$

Therefore, our vector potential takes the form $\vec{A} = \frac{\Phi}{2\pi b}\hat{\phi}$. It should be noted that this potential is within the Coulomb's Gauge (i.e. $\vec{\nabla} \cdot \vec{A} = 0$).

A.1 Solution of the Time Independent Schrödinger's Equation

Given that there is no time-dependence in the Hamiltonian of the system, we can use separation of variables, to arrive to the following eigenvalue equation.

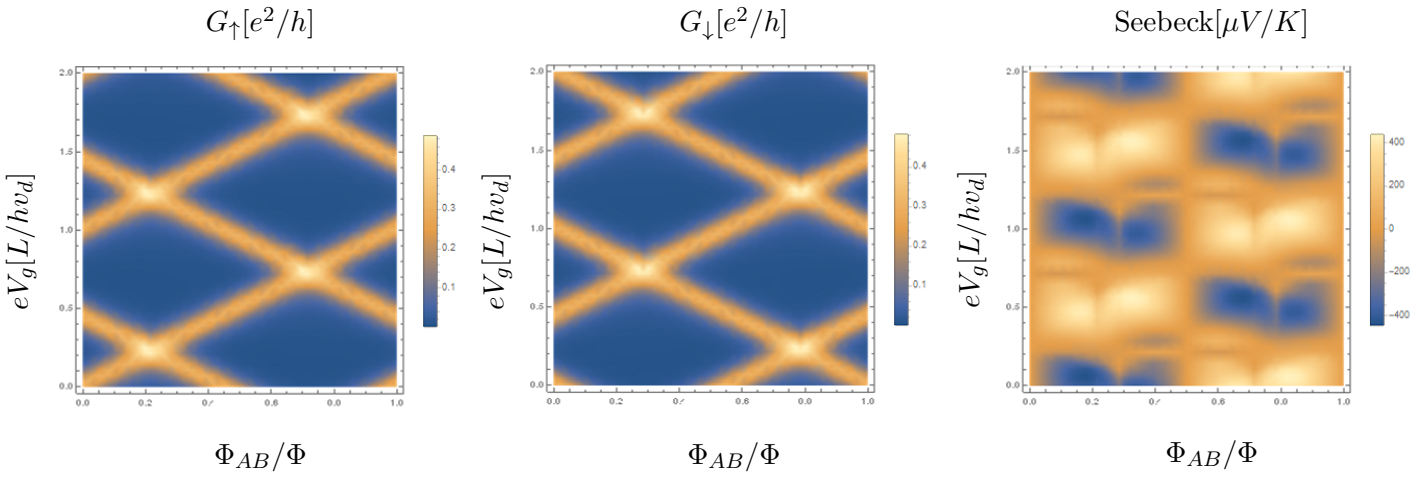

Figure 15: Density plots of the electric conductance for each spin channel and the Spin Seebeck Coefficient versus magnetic flux Φ_{AB} and gate voltage V_g for $\eta = \beta - 1 = 90.59$ and $\delta L/L = 0.3$.

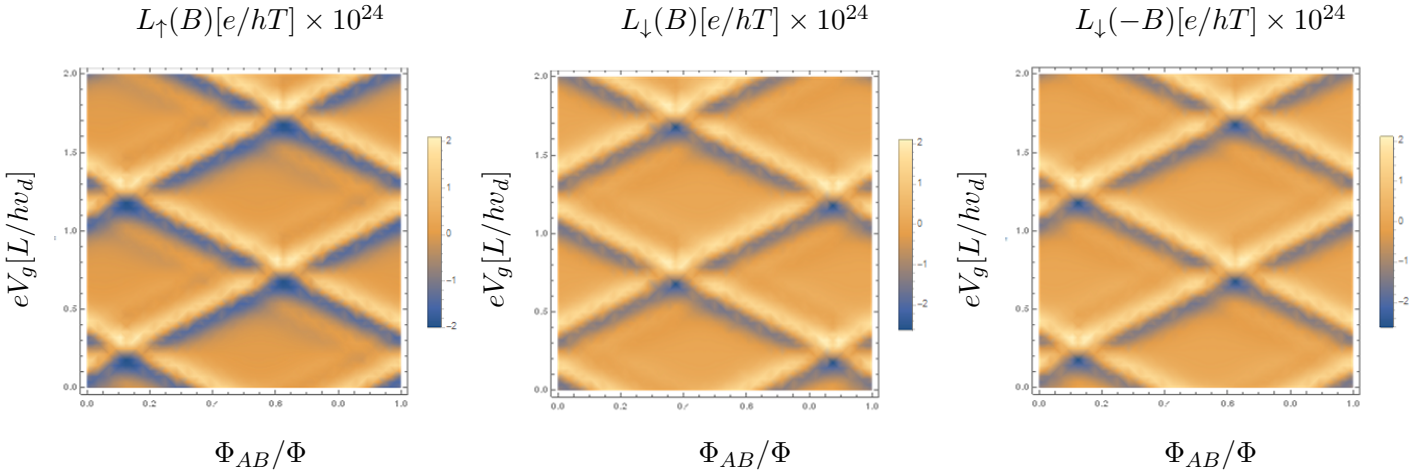

Figure 16: Density plots of the thermal conductance for each spin channel versus magnetic flux Φ_{AB} and gate voltage V_g for $\eta = \beta - 1 = 0.15$ and $\delta L/L = 0.3$.

$$\hat{H}\psi = E\psi \tag{A.3}$$

Introducing the canonical momentum for an electron, $\vec{\pi} = \vec{p} + \frac{e}{c}\vec{A}$, the equation to solve is:

$$\left[p^2 + \left(\frac{e}{c}\right)^2 A^2 + 2\frac{e}{c}\vec{A}\cdot\vec{p}\right]\psi = 2mE\psi \tag{A.4}$$

Due to the geometry of the problem, the momentum operator will take the form $\vec{p} = \frac{\hbar}{ib}\frac{\partial}{\partial\phi}\hat{\phi}$. Substitution in the above equation of the momentum and vector potential reads:

$$\left[-\frac{\hbar^2}{b^2}\frac{d^2}{d\phi^2} + \left(\frac{e}{c}\right)^2\left(\frac{\Phi}{2\pi b}\right)^2 - 2i\frac{e}{c}\frac{\Phi}{2\pi b}\frac{\hbar}{b}\frac{d}{d\phi}\right]\psi = 2mE\psi \tag{A.5}$$

After some careful manipulation we can arrive to the following equality:

$$\frac{d^2\psi}{d\phi^2} + 2i\frac{\Phi}{\Phi_L}\frac{d\psi}{d\phi} + C\psi = 0 \tag{A.6}$$

where we have introduced the quantum flux $\Phi_L = \frac{2\pi\hbar c}{e}$, the constant $C = \left(\frac{E}{E_{rot}} - \frac{\Phi}{\Phi_L^2}\right)$ and the energy corresponding to the first rotational mode $E_{rot} = \frac{\hbar^2}{2mb^2}$.
A second order linear ODE like (A.6) can be solved by introducing wavefunctions of the form $\psi(\phi) = Ae^{ik\phi}$, leading to the following equation for the modes:

$$k^2 + 2\frac{\Phi}{\Phi_L}k - C = 0 \tag{A.7}$$

Thus,

$$k = -\frac{\Phi}{\Phi_L} \pm \sqrt{\frac{E}{E_{rot}}} \tag{A.8}$$

A further constraint can be obtained for the wavevectors by imposing periodic boundary conditions.

$$\psi(\phi) = Ae^{ik\phi} = \psi(\phi + 2\pi) = Ae^{ik\phi}e^{i2\pi k} \tag{A.9}$$

which means that k must be an integer. That is $k = n = 0, \pm 1, \pm 2, ...$
As a consequence of (A.8) and (A.9), we will have discrete energy levels of the form:

$$E_n = E_{rot}\left(n + \frac{\Phi}{\Phi_L}\right)^2 = \frac{\hbar^2}{2mb^2}\left(n + \frac{\Phi}{\Phi_L}\right)^2 \tag{A.10}$$

In the case of no magnetic field, (A.10) allows us to recover the usual energy levels for a particle rotating in a circle $E_n = \frac{\hbar^2 n^2}{2mb^2}$.

A.2 Orthogonality of Eigenstates

We will now prove that the basis for our wave function is orthogonal, which is an important result knowing that the Hamiltonian is a hermitian operator and as such, should have mutually orthogonal eigenstates. In our geometry, orthogonality of a basis takes the following form:

$$\int_0^{2\pi} \psi^*_{n'}(\phi)\psi_n(\phi)bd\phi = 0 \tag{A.11}$$

where $\psi_{n'}$ and $\psi_n(\phi)$ are different elements of our basis $\{\psi_n(\phi)\} = \{e^{in\phi}\}$.
By introducing the elements of our basis into equation A.11 and expanding the exponentials in terms of sines and cosines we get:

$$\begin{aligned} \int_0^{2\pi} e^{i(n-n')\phi}bd\phi &= \int_0^{2\pi} \{cos\left[i(n-n')\phi\right] + isin\left[i(n-n')\phi\right]\}bd\phi = \\ &= \left\{\frac{sin\left[i(n-n')\phi\right]}{n-n'} - i\frac{cos\left[i(n-n')\phi\right]}{n-n'}\right\}_{\phi=0}^{\phi=2\pi} = 0 \end{aligned} \tag{A.12}$$

where we have used the above result that the wavenumbers must be intergers (i.e. $n = 0, \pm 1 \pm 2, ...$).

A.3 Aharonov Bohm Phase Shift

The Time Dependent Schrödinger Equation for an electron in a region of $\vec{A} \neq 0$ and $\vec{B} = 0$ is:

$$i\hbar\frac{d\Psi}{dt} = \hat{H}\Psi = \left[\frac{1}{2m}\left(\frac{\hbar}{i}\vec{\nabla} + \frac{e}{c}\vec{A}\right)^2\right]\Psi \tag{A.13}$$

It is a well known result that the solution of equation (A.13), is given by the solution for no magnetic field Ψ_O times a phase factor containing the vector potential $\vec{A}$.

$$\Psi = \Psi_O e^{ig(r)} \tag{A.14}$$

where

$$g(r) = -\frac{e}{\hbar c}\int_{\vec{rO}}^{\vec{r}} \vec{A}\cdot\vec{dr} \tag{A.15}$$

To prove this result we will first apply the canonical momentum operator to the wavefunction.

$$\begin{aligned} \vec{\pi}\Psi &= \left(\frac{\hbar}{i}\vec{\nabla} + \frac{e}{c}\vec{A}\right)\Psi = \frac{\hbar}{i}\vec{\nabla}(\Psi_O)e^{ig(r)} + \frac{\hbar}{i}\Psi_O\vec{\nabla}(e^{ig(r)}) + \frac{e}{c}\vec{A}\Psi \\ &= \frac{\hbar}{i}\vec{\nabla}(\Psi_O)e^{ig(r)} + \frac{\hbar}{i}\Psi_O e^{ig(r)}(-\frac{e}{c})\vec{A} + \frac{e}{c}\vec{A}\Psi = \frac{\hbar}{i}\vec{\nabla}(\Psi_O)e^{ig(r)} \end{aligned} \tag{A.16}$$

Hence, equation (A.13) can be expressed as:

$$i\hbar\frac{d\Psi}{dt} = i\hbar\frac{d\Psi_O}{dt}e^{ig(r)} = -\frac{\hbar^2}{2m}\nabla^2(\Psi_O)e^{ig(r)} \tag{A.17}$$

Removing the common terms at both sides of the equality, we indeed find that Ψ_O satisfies the Schrödinger Equation for $\vec{A} = 0$

$$i\hbar\frac{d\Psi_O}{dt} = -\frac{\hbar^2}{2m}\nabla^2(\Psi_O) \tag{A.18}$$

which implies that the addition of a non-zero vector potential only results in a phase difference with the unperturbed wavefunction.
Now, the question that arises is if we can arrive to the same conclusion with the result from the previous section, knowing that the wavefunction must be expressed as.

$$\Psi = \sum_{\{E\}} A(E)e^{-i\frac{E}{\hbar}t}e^{ik(E)\phi} \tag{A.19}$$

We will begin by looking at the expression for the wavenumber in terms of the energy (A.8)

$$k = -\frac{\Phi}{\Phi_L} \pm \sqrt{\frac{E}{E_{rot}}} = -\frac{\Phi}{\Phi_L} \pm k_O(E) \tag{A.20}$$

where $k_O(E) = \sqrt{\frac{E}{E_{rot}}}$ would be the wavenumber associated to an electron with the same energy in the case of no magnetic field. Combination of the two previous expressions yields:

$$\Psi = \sum_{\{E\}} A(E)e^{-i\frac{E}{\hbar}t}e^{ik(E)\phi} = e^{-i\frac{\Phi}{\Phi_L}\phi}\sum_{\{E\}} C_1(E)e^{-i\frac{E}{\hbar}t}e^{ik_O(E)\phi} + C_2(E)e^{-i\frac{E}{\hbar}t}e^{-ik_O(E)\phi} \tag{A.21}$$

Here, we can see how our expansion is the expansion in the case of no magnetic field plus an additional phase factor.
This phase term can be expressed in the following way:

$$e^{-i\frac{\Phi}{\Phi_L}\phi} = e^{-i\frac{e}{2\pi\hbar c}(2\pi b A_\phi)\phi} = e^{-i\frac{e}{\hbar c}\int_0^\phi A_\phi b d\phi} = e^{i\frac{(-e)}{\hbar c}\int_0^\phi A_\phi b d\phi} \tag{A.22}$$

This is precisely the phase shift that you would find using equation A.15 putting as reference $\phi = 0$.

B Aharonov Bohm effect in a 1D Quantum Ring with Spin-Orbit Interaction

In the presence of Spin-Orbit Interaction and a constant vector potential with only angular component, the Hamiltonian of a one-dimensional ring of radius b is given by [11]:

$$\hat{H} = \frac{\hbar^2}{2mb^2}\left(-i\frac{\partial}{\partial\phi} + \frac{\Phi}{\Phi_L}\right)^2 + \frac{\alpha}{b}\left(\sigma_x cos(\phi) + \sigma_y sin(\phi)\right)\left(-i\frac{\partial}{\partial\phi} + \frac{\Phi}{\Phi_L}\right) - i\frac{\alpha}{2b}\left(\sigma_y cos(\phi) - \sigma_x sin(\phi)\right) \tag{B.1}$$

where Φ is the magnetic flux given by (A.1), $\Phi_L = \frac{2\pi\hbar c}{e}$ is the quantum flux, α is the Rashba SO constant and σ_x and σ_y are the Pauli matrices.
We can further simplify a bit our expression by introducing the parameters $E_{rot} = \frac{\hbar^2}{2mb^2}$ and $\omega_{so} = \frac{\alpha}{\hbar b}$ and the Pauli matrices in cylindrical coordinates $\sigma_r = \sigma_x cos(\phi) + \sigma_y sin(\phi)$ and $\sigma_\phi = \sigma_y cos(\phi) - \sigma_x sin(\phi)$.

$$\hat{H} = E_{rot}\left(-i\frac{\partial}{\partial\phi} + \frac{\Phi}{\Phi_L}\right)^2 + \hbar\omega_{so}\sigma_r\left(-i\frac{\partial}{\partial\phi} + \frac{\Phi}{\Phi_L}\right) - i\frac{\hbar\omega_{so}}{2}\sigma_\phi \tag{B.2}$$

We will now try to simplify the expression for the Hamiltonian. First, we can note that the Pauli matrices are related by $\sigma_\phi = \partial\sigma_r/\partial\phi$. This allows us to right-hand side terms as:

$$\begin{aligned}\hbar\omega_{so}\sigma_r\left(-i\frac{\partial}{\partial\phi} + \frac{\Phi}{\Phi_L}\right) - i\frac{\hbar\omega_{so}}{2}\sigma_\phi &= \hbar\omega_{so}\sigma_r\left(-i\frac{\partial}{\partial\phi} + \frac{\Phi}{\Phi_L}\right) - i\frac{\hbar\omega_{so}}{2}\frac{\partial\sigma_r}{\partial\phi} \\ &= \frac{\hbar\omega_{so}}{2}\sigma_r\left(-i\frac{\partial}{\partial\phi} + \frac{\Phi}{\Phi_L}\right) + \frac{\hbar\omega_{so}}{2}\left(-i\frac{\partial}{\partial\phi} + \frac{\Phi}{\Phi_L}\right)\sigma_r\end{aligned} \tag{B.3}$$

Taking into account that $\sigma_r^2 = \sigma_x^2 cos^2(\phi) + \sigma_y^2 sin^2(\phi) = \hat{\mathbb{I}} cos^2(\phi) + \hat{\mathbb{I}} sin^2(\phi) = \hat{\mathbb{I}}$, we can rewrite (B.2) into

$$\hat{H} = E_{rot}\left(-i\frac{\partial}{\partial\phi} + \frac{\Phi}{\Phi_L} + \frac{\omega_{so}}{2\Omega}\sigma_r\right)^2 \tag{B.4}$$

where we have introduced the parameter $\Omega = E_{rot}/\hbar$ and neglected an additive constant $\frac{\hbar\omega_{so}^2}{2\Omega}$ since it carries no physical meaning.

B.1 Diagonalization of the Hamiltonian

Given our Hamiltonian (B.4), we can find the energies and eigenstates by diagonalizing the corresponding matrix. We will follow a procedure similar to the one that can be found in Ref. [12] in the case of no magnetic flux. Since our Hamiltonian is the square of an operator, we can simplify the problem by diagonalizing that operator.

The eigenvalue problem to solve is then:

$$\left(-i\frac{\partial}{\partial\phi} + \frac{\Phi}{\Phi_L} + \frac{\omega_{so}}{2\Omega}\sigma_r\right)\psi(\phi) = \lambda\psi(\phi) \tag{B.5}$$

where the eigenvalues relate to the energies as $E = E_{rot}\lambda^2$.

Introducing solutions of the form

$$\psi(\phi) = e^{ik\phi}\chi(\phi) = e^{ik\phi}\begin{pmatrix} a \\ be^{i\phi}\end{pmatrix}, \tag{B.6}$$

we obtain

$$\left(-i\frac{\partial}{\partial\phi} + \frac{\omega_{so}}{2\Omega}\sigma_r\right)\chi(\phi) = \left(\lambda - k - \frac{\Phi}{\Phi_L}\right)\chi(\phi). \tag{B.7}$$

We can further simplify the eigenvalue problem by introducing $\sigma_r = \begin{pmatrix} 0 & e^{-i\phi} \\ e^{i\phi} & 0\end{pmatrix}$(in the S_Z basis) and take a look at the result of (B.7).

$$-i\frac{\partial}{\partial\phi}\chi(\phi) + \frac{\omega_{so}}{2\Omega}\sigma_r\chi(\phi) = \begin{pmatrix} \frac{\omega_{so}}{2\Omega}b \\ \left(\frac{\omega_{so}}{2\Omega}a + b\right)e^{i\phi}\end{pmatrix} = \left(\lambda - k - \frac{\Phi}{\Phi_L}\right)\begin{pmatrix} a \\ be^{i\phi}\end{pmatrix} \tag{B.8}$$

From (B.8) we can construct our final eigenvalue equation:

$$\begin{pmatrix} 0 & \frac{\omega_{so}}{2\Omega} \\ \frac{\omega_{so}}{2\Omega} & 1\end{pmatrix}\begin{pmatrix} a \\ b\end{pmatrix} = \left(\lambda - k - \frac{\Phi}{\Phi_L}\right)\begin{pmatrix} a \\ b\end{pmatrix} = \epsilon\begin{pmatrix} a \\ b\end{pmatrix} \tag{B.9}$$

The eigenvalues of the above equation are $\epsilon = \frac{1}{2} + (-1)^\mu\sqrt{\frac{1}{4} + \frac{\omega_{so}^2}{4\Omega^2}} = -\Phi_{AC}^\mu/2\pi$, where $\mu = 1, 2$ and Φ_{AC} is the Aharanov-Casher phase. The normalized eigenvectors u_μ of the equation are $u_1 = \frac{1}{\sqrt{2(\omega_{so}/2\Omega)^2 - \Phi_{AC}^{(2)}/2\pi}}\begin{pmatrix} -\Phi_{AC}^{(2)}/2\pi \\ -\omega_{so}/2\Omega\end{pmatrix}$ and $u_2 = \frac{1}{\sqrt{2(\omega_{so}/2\Omega)^2 - \Phi_{AC}^{(2)}/2\pi}}\begin{pmatrix} \omega_{so}/2\Omega \\ -\Phi_{AC}^{(2)}/2\pi\end{pmatrix}$.

In summary, we find that our energies are given by

$$E(k) = E_{rot}\left(k + \frac{\Phi}{\Phi_L} - \frac{\Phi_{AC}^\mu}{2\pi}\right)^2 \tag{B.10}$$

with the wavenumber being related to the energies as

$$k^{(\mu)} = -\frac{\Phi}{\Phi_L} + \frac{\Phi_{AC}^\mu}{2\pi} \pm \sqrt{\frac{E}{E_{rot}}}. \tag{B.11}$$

The eigenstates of the system end up looking as $\psi(\phi) = e^{ik\phi}\chi^{(\mu)}(\phi)$ with the $\chi^{(\mu)}$ being spinors that in the S_z basis take the form

$$\chi^{(1)}(\phi) = \frac{1}{\sqrt{2\left(\omega_{so}/2\Omega\right)^2 - \Phi_{AC}^{(2)}/2\pi}}\begin{pmatrix} -\Phi_{AC}^{(2)}/2\pi \\ -\omega_{so}/2\Omega\cdot e^{i\phi}\end{pmatrix} \tag{B.12}$$

$$\chi^{(2)}(\phi) = \frac{1}{\sqrt{2\left(\omega_{so}/2\Omega\right)^2 - \Phi_{AC}^{(2)}/2\pi}}\begin{pmatrix} \omega_{so}/2\Omega \\ -\Phi_{AC}^{(2)}/2\pi\cdot e^{i\phi}\end{pmatrix}. \tag{B.13}$$

we shall also indicate that (B.11) indicates that SOI adds an additional phase with displacement in the same way as the Aharonov-Bohm Effect.

References

[1] R. S. Whitney, R. Sanchez, and J. Splettstoesser, in Thermodynamics in the Quantum Regime, edited by F. Binder, L. A. Correa, C. Gogolin, J. Anders, and G. Adesso (Springer, Switzerland, 2018), pp. 175–206.

[2] F. Giazotto and M. J. Martinez-Perez, Appl. Phys. Lett. 101, 102601 (2012).

[3] Giazotto, F., Heikkilä, T. T., Luukanen, A., Savin, A. M. Pekola, J. P. Opportunities for mesoscopics in thermometry and refrigeration: Physics and applications. Rev. Mod. Phys. 78, 217–274 (2006).

[4] H. van Houten, L. W. Molenkamp, and C. W. J. Beenakker, Semicond. Sci. Technol. 7, 215 (1992).

[5] R. S. Whitney, Phys. Rev. Lett. 112, 130601 (2014); Phys. Rev. B 91, 115425 (2015).

[6] Y. Aharonov and D. Bohm, Phys. Rev. 115, 485 (1959).

[7] Manchon, A., Koo, H. C., Nitta, J., Frolov, S. M. Duine, R. A. New perspectives for Rashba spin–orbit coupling. Nat. Mater. 14, 871–882 (2015).

[8] Chowrira B, Kandpal L, Lamblin M, Ngassam F, Kouakou CA, Zafar T, Mertz D, Vileno B, Kieber C, Versini G, Gobaut B, Joly L, Ferté T, Monteblanco E, Bahouka A, Bernard R, Mohapatra S, Prima Garcia H, Elidrissi S, Gavara M, Sternitzky E, Da Costa V, Hehn M, Montaigne F, Choueikani F, Ohresser P, Lacour D, Weber W, Boukari S, Alouani M, Bowen M. Quantum Advantage in a Molecular Spintronic Engine that Harvests Thermal Fluctuation Energy. Adv Mater. 2022 Dec;34(49):e2206688. doi: 10.1002/adma.202206688. Epub 2022 Oct 31. PMID: 36177716.

[9] Seeking Maxwell's Demon in a non-reciprocal quantum ring, Aram Manaselyan, Wenchen Luo, Daniel Braak, Tapash Chakraborty, Scientific Reports 9, 9244 (2019).

[10] Uchida, K. et al. Observation of the spin Seebeck effect. Nature 455, 778–781 (2008).

[11] F.E. Meijer, A.F. Morpurgo and T.M. Klapwijk, Phys. Rev. B 66, 033107 (2002).

[12] B. Molnár, F. M. Peeters, and P. Vasilopoulos, Phys. Rev. B 69, 155335 (2004).

[13] G. Haack and F. Giazotto, Phys. Rev. B 100, 235442 (2019).

[14] M. Büttiker, Y. Imry, and M. Ya. Azbel, Phys. Rev. A 30, (1982).

[15] Keiji Saito, Giuliano Benenti, Giulio Casati, and Tomaž Prosen, Phys. Rev. B 84, 201306(R) (2018).

Power grid stability in scenarios of large VRES penetration

Agostina Iozzi Acosta, María Martínez Barbeito, Pere Colet Rafecas
Instituto de Física Interdisciplinar y Sistemas Complejos, IFISC (CSIC-UIB)
Campus Universitat de les Illes Balears, E-07122 Palma de Mallorca, Spain

Abstract

This article pretends to bring light to the penetration of variable renewable energy sources into a power grid. By studying the frequency dynamics, we are able to determine the power grid' stability, therefore, we can prevent blackouts and line failures from happening. The central objective of this work is to implement a battery into the power grid to control frequency fluctuations. We modeled the power grid as a set of nodes (generators and consumers) interacting via links (power transmission lines) and chose Gran Canaria as our case study. Once we had simulated different scenarios and played with different parameters, we finally found the most suitable battery for Gran Canaria's power grid, able to reduce frequency fluctuations.

1 Introduction

Since electricity has become essential to guarantee the well-being and commodities of our modern societies, understanding how power grids work and being able to predict their stability (balance between consumption and generation at any time) is key to ensuring their good function. Despite that, one of humanity's purposes is to achieve decarbonization, due to the escalating climate change. To do so without losing the advantages of electricity, variable renewable energy sources (VRES) must be part of the solution.

Although VRES are the greatest option we currently have, they entail two significant drawbacks. Because they are subject to uncontrollable factors (e.g., weather conditions), they are intermittent and unpredictable (unlike conventional power plants, which are controllable energy sources), which jeopardizes the power grid' stability. This correlation is because networks have to operate around a given reference frequency to be stable (50 Hz in Europe). Stable grid operation is also characterized by the randomness of the load and, due to the lack of large-scale storage capacity, production has to be adjusted to the demand continuously and in real-time. As a result, when consumption increases, the frequency of the network decreases, forcing the generators to raise their output, and vice versa. Hence, we can understand frequency fluctuations as a measure of the difference between supply and demand, i.e., the instability of the grid. As we will see, these fluctuations can be induced by the load and/or the generation variations (power imbalances).

The second downside is the practically null inertia of the VRES, considering wind and sunlight as the two major energy sources. Because conventional power plants provide inertia and control frequency dynamics, they help to reduce the amplitude of frequency fluctuations, unlike VRES, which can even bring them up at different timescales, making it harder to match the production to the consumption. Consequently, this affects the global flexibility of the grid and decreases its reliability.

Being clear that any unbalance in the network may cause a blackout or a line failure, this essay aims to apply a storage strategy to palliate the possible inconveniences that may arise when introducing a larger share of VRES in high-voltage power grids. We will consider only two of them: solar and wind, focusing on the latter, due to the characteristics of the studied system, Gran Canaria (Spain), which has abundant wind power generation available all year. Other reasons to choose this island as our case study are its relatively small size and energy independence, given that it is not connected to any mainland.

2 Theoretical model

High-voltage power grids are networks of interacting conventional power plants, VRES, and substations (consumers) connected via power transmission lines, and we represent them as networks of interacting nodes connected via links. All nodes can be viewed as nonlinear oscillators that operate synchronously at the same frequency. We consider devices below the substation level as aggregated loads. To normalize frequency to zero, we choose a reference frame rotating to the reference frequency of the network. We always assume that the voltage is kept within legal limits.

Because conventional power plants are powered by synchronous generators (large rotating masses), they have mechanical inertia and can store kinetic energy. This available energy can help to stabilize the grid, slowing down frequency dynamics and dampening fluctuations. If the production exceeds the consumption, the rotating masses absorb the energy surplus and rotate faster (at a higher frequency). Conversely, if the supply does not cover the demand, the rotating masses provide energy and rotate slower (at a lower frequency). Again, we notice that frequency is a good indicator of the stability of the network.

To model the dynamic behaviour of conventional generators taking into account their inertial characteristics, we use the definition of angular velocity and the swing equation, shown in Eq. (2.1), where the subscript $_i$ refers to the node's number.

$$\dot{\theta}_i = \omega_i \ , \qquad \dot{\omega}_i = \frac{\omega_R^2}{2 \cdot \hat{H}_i \cdot (\omega_i + \omega_R)} (P_i^m - P_i^e) \ , \tag{2.1}$$

where θ_i is the voltage phase, ω_i, the angular frequency, ω_R, the reference frequency, $\hat{H}_i$, the inertia constant, P_i^m, the supplied mechanical power and P_i^e, the electrical power. The inertia constant is the product of the inertia per unit power, H_i, and the nominal power generation, P_i^G, i.e., $\hat{H}_i = H_i P_i^G$. Note that the swing equation is nonlinear in ω_i. Even if the rotating mass speed does not vary significantly from synchronous speed (transient state), i.e., $\omega_i + \omega_R \simeq \omega_R$, this non-linearity does not disappear if frequency control mechanisms (see Eq. (2.2)) are implemented.

If the exchange of kinetic energy with the rotating masses does not compensate for frequency deviations (from its nominal value), power plants rely on two control mechanisms that act at different timescales. The primary control (left expression in Eq. (2.2)) can stop the frequency drift within a few seconds, to stabilise its value to the reference frequency progressively. Subsequently, the secondary control (right expression in Eq. (2.2)) restores frequency to its nominal value within a few minutes.

$$\dot{P_i^m} = \frac{1}{\tau_i} \left[P_i^s - P_i^m - \frac{P_i^c}{R_i} \frac{\omega_i}{\omega_R} \right] \ , \qquad \dot{P_i^s} = -\kappa_i \frac{\omega_i}{\omega_R} - \frac{1}{\tau_i^{ref}} (P_i^s - P_i^{ref}) \ , \tag{2.2}$$

where τ_i is the turbine time constant, P_i^s, the spinning reserve power, R_i, the governor speed regulation parameter, P_i^c, the primary control power, κ_i, the integral controller gain, τ_i^{ref}, the timescale of the forcing and P_i^{ref}, the reference power. The first term of the secondary control expression ensures that the total generation covers the demand, but does not impose any condition on which fraction of generation corresponds to which plant. To break this indeterminacy, we have to add the second term, which forces plants to operate close to a given set point, P_i^{ref}, on a scale of several minutes, τ_i^{ref}. Accordingly, power interchanges are satisfied because we are able to establish a reference power for each plant based on the demand. Furthermore, generation dispatch data is assimilated into the model. If we set $P_i^{ref} = 0$, the power output of that plant is null, however, it still contributes to the global inertia and control capacity of the system. To completely shut down a power plant, we would also have to impose $P_i^c/R_i = 0$, $\kappa_i = 0$, and the inertia constant to be that of a consumer node (see next paragraph).

Consumers correspond to substations, which include the attached load from lower grid levels. Even though they do not have generation or mechanisms of frequency control, they may present some residual inertia (very low compared to the power plants'). Along these lines, we can model consumers using the conventional generators' equations, but setting $P_i^m = 0$ and the inertia constant to be $\hat{H}_i^{\,C}$:

$$\dot{\theta}_i = \omega_i \ , \qquad \dot{\omega}_i = \frac{\omega_R^2}{2 \cdot \hat{H}_i^{\,C} \cdot (\omega_i + \omega_R)} (-P_i^e) \ . \tag{2.3}$$

Regardless of the node type, the electric power is given by Eq. (2.4).

$$P_i^e = \left(1 + D_i \frac{\omega_i}{\omega_R}\right) P_i^d + \sum_j \hat{B}_{ij} \cdot sin(\theta_i - \theta_j) - P_i^{VRES} \ , \qquad \text{where } \hat{B}_{ij} = \frac{V_{ij}^2}{Z_{ij}}. \tag{2.4}$$

Seeing that equivalent loads include all types of devices, their demand can be frequency and voltage-dependent. Nonetheless, since we consider that the voltage is kept constant, there is no such dependency. To account for the frequency dependency, we introduce D_i as the percent change in load divided by the percent change in frequency. Considering that our loads can correspond to residential, commercial, or industrial consumers and that we do not know the load distribution across substations, we estimate that $D_i = 1$. In consequence, if the frequency decreases (and conventional plants do not entirely correct this unbalance by increasing their production), the loads reduce their demand, and vice versa. A great approach to describe the power demand dynamics, P_i^d, as shown in [1], is to plot the power spectrum of frequency measurements recorded at different timescales, given that frequency is a reflection of the demand-generation balance. It is concluded that frequency fluctuations (thus, demand) have a power spectrum characteristic of an Ornstein-Uhlenbeck (OU) noise, which is a correlated stochastic process that follows Eq. 2.5.

$$P_i^d(t) = P_i^{dd}(t)(1 + \epsilon_{ou}\xi_{ou}(t)) \ , \tag{2.5}$$

where P^{dd} is the actual demand data provided by the grid operator at the scale of minutes, which we interpolate and use as the demand's base profile. We incorporate the faster stochastic changes, ξ_{ou}, with an amplitude ϵ_{ou}. This process has a zero mean $<\xi_{ou}(t)> = 0$ and a correlation $<\xi_{ou}(t)\xi_{ou}(t')> = \frac{1}{2\tau_{ou}} e^{-\frac{|t-t'|}{\tau_{ou}}}$, being τ_{ou} the correlation time.

In order to understand what represents the second addend of the left expression in Eq. 2.4, we have to focus only on high-voltage transmission lines. That implies working within the lossless line approximation (resistance is smaller than reactance) and neglecting voltage fluctuations. This term represents the power transmitted from node i to its neighboring nodes j. $\hat{B}_{ij}$ is the susceptance parameter of the line that connects node i to node j, V_{ij} is the voltage of the line, and Z_{ij} is the impedance of the line, estimated by the line's longitude.

Given that VRES generation technologies connect to the grid via power electronic inverters effectively, their power, P_i^{VRES}, can be described as a frequency- and voltage-independent negative demand, because of their negligible inertia.

When it comes to integrating a battery into the network, it can be understood as a primary control with an additional term to avoid large deviations of the charge of the battery, Q, from the charge set point, Q_{SP}:

$$\frac{dP_b}{dt} = \frac{1}{\tau_b}\Big[\gamma\,(Q - Q_{SP}) - P_b - \alpha\omega\Big] \ , \qquad \frac{dQ}{dt} = -P_b \ , \tag{2.6}$$

where Q can solely oscillate between zero and the capacity of the battery, C (boundaries included), and the absolute power provided by the battery, $|P_b|$, has to be lower or equal to $P_{b,max} = 2C$, which means it can discharge or charge at a rate equivalent to twice its capacity per hour. Even though the battery can emulate the plants' frequency control mechanisms, we impose that its response time, τ_b, has to be smaller than that of conventional primary control, so it acts faster. Additionally, γ controls the charge fluctuations by adjusting the strength of the forcing towards Q_{SP} and α determines the strength of the reaction to frequency deviations. To guarantee that the restrictions of Q and P_b are met, first, we calculate $\bar{Q} = Q(t) - P_b(t)dt$, where dt is the integration time step. At that point, we proceed depending on the value of $\bar{Q}$:

- If $0 \leq \bar{Q} \leq Q_{max}$, then $Q(t + dt) = \bar{Q}$ and P_b is given by Eq. 2.6.
- If $\bar{Q} < 0$, then $Q(t + dt) = 0$ and the battery delivers the power allowed by the remaining battery energy $P_b(t + dt) = Q(t)/dt$.
- If $\bar{Q} > Q_{max}$, then $Q(t + dt) = Q_{max}$ and $P_b(t + dt) = (Q(t) - Q_{max})/dt$.

Because batteries age unavoidably and their performance decreases over time, we estimate battery wear based on the number of cycles per day. The number of equivalent charge-discharge cycles over some time t, n_{cycles}, can be estimated as:

$$n_{cycles} = \frac{E_b}{E_{b,1cycle}} , \qquad \text{where } E_b(t) = \int_0^t |P_b(s)|ds , \tag{2.7}$$

where E_b is the absolute value of the energy interchanged by the battery accumulated over time and $E_{b,1cycle} = 2C$ is the energy in a full charge and discharge cycle.

This model can be used to simulate grid dynamics over extended periods of time and of grids of any size and any generation technologies, with the one condition that there is enough inertia to disregard sub-second timescale dynamics.

3 Results and discussion

The program used to create the simulations, written by María Martínez and Pere Colet, integrates power grid dynamics using a first-order semi-implicit Euler method and taking advantage of the sparse structure of the grid. We obtain Gaussian random numbers with the Box-Muller algorithm and use the same set of numbers for every simulation, in order to be able to compare them. To implement the battery equations in the grid, we use a first-order explicit Euler method.

Dispatch data has also been provided by María Martínez and Pere Colet. Dispatch files were created using 10-minute power data from *Red Eléctrica de España* for Gran Canaria. Each of them contains the load per node, the operation set point (and its timescale) of each generating group, and the power provided by renewables. All simulations are of the day 07/02/2019.

Regarding constant parameters, we consider the reference frequency, ω_R, equal to $2\pi f_R$, where $f_R = 50$ Hz because of Europe's regulations, and the charge set point, to be the 60% of the maximum charge. For other global parameters, see the next table.

Parameter	**Value**
Nodes	29
Power stations	6
Transmission lines	39
VRES	6
Integration time step (s)	0.2
D	1
τ_{ou} (s)	60
ϵ_{ou}	0.15
$\hat{H}^{consumers}$ (MWs)	10^{-4}

Table 1: Values of the global constant parameters used in all simulations.

Once we have briefly stated how the program works, we present which approach we have taken. First of all, to comprehend the huge potential of VRES, we simulate ten different cases of wind power generation. Secondly, we aim to contrast the effectiveness and durability of two size-different batteries, to figure out which one is more convenient. As soon as we have concluded the proper battery' size, we try to determine the most adequate value of α, considering the battery's limitations. Finally, with the right value of α, we adjust γ to enhance the battery's performance.

To better interpret the simulations, we also compute the complementary cumulative distribution of the absolute frequency deviations, $|f|$. To do so, first, we reorder the data from the smallest to the largest and evaluate the rank of the frequency deviations as $R(|f_k|) = 1-(k-1)/(N-1)$, being N the number of data points. That way, $R(|f|)$ measures the probability of having a frequency fluctuation of size larger than $|f|$. In addition, we calculate the standard deviation and the rate of change of frequency (RoCoF). The last one is calculated by making the difference between two consecutive values of frequency and dividing by the time step that separates them (in our case, a one-second time interval). RoCoF quantifies the faster behavior of the frequency.

3.1 Wind power

In this section, we represent ten different cases of wind power generation of the same day. To do so, we multiply the actual wind power generation of that day by numbers between one and ten. It is worth mentioning that, although the plots shown correspond to simulations without battery, integrating it would not modify them.

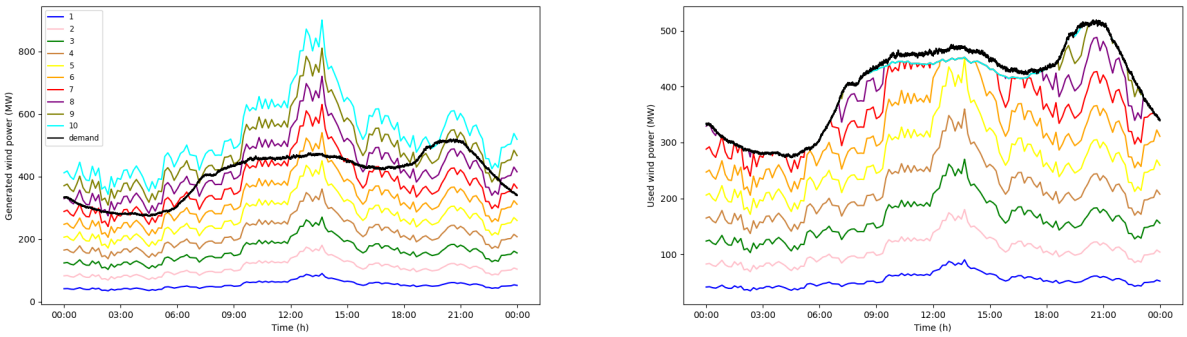

Figure 1: The left plot corresponds to the generated wind power and the right plot, to the used wind power, both of the same day. The numbers in the legend of the left plot indicate the multiplicative factor applied to wind generation. This legend is used for both plots.

As we can observe in the two images, as we augment wind power generation, a bigger fraction of the demand is covered by it, being able to almost satisfy it (seven-or-more-times cases). Starting at that simulation, the energy excess (not used to meet the demand) has to be discarded if it cannot be stored in a battery.

3.2 Size determination

To ascertain the most suitable battery, we compare two size-different ones by plotting how well they reduce frequency fluctuations and how much their power and charge vary in three α-different scenarios. From now on, each time we plot frequency fluctuations, we will do it against the frequency fluctuations obtained without battery (in color blue) and with two dotted lines at ± 0.15 Hz that indicate the statutory limits. In the case of charge plots, they will have a dotted line to designate the corresponding Q_{SP} value. That being said, the battery's parameters used are given in the next table. Just to situate us, notice that the small and big batteries correspond to batteries of maximum charges of 1000 kWh and 10000 kWh, respectively (an electric car uses a battery with a maximum charge between 40 to 100 kWh).

Battery's parameters	**Small**	**Big**
Q_{max} (MWs)	3600	36000
$P_{b,max}$ (MW)	2	20
τ_b (s)	0.2	0.2
γ (Hz)	0.002	0.002
Q_{SP} (MWs)	2160	21600
α (MWs)	0.5//2.5//4.5	0.5//2.5//4.5

Table 2: Values of the battery's parameters used in this section.

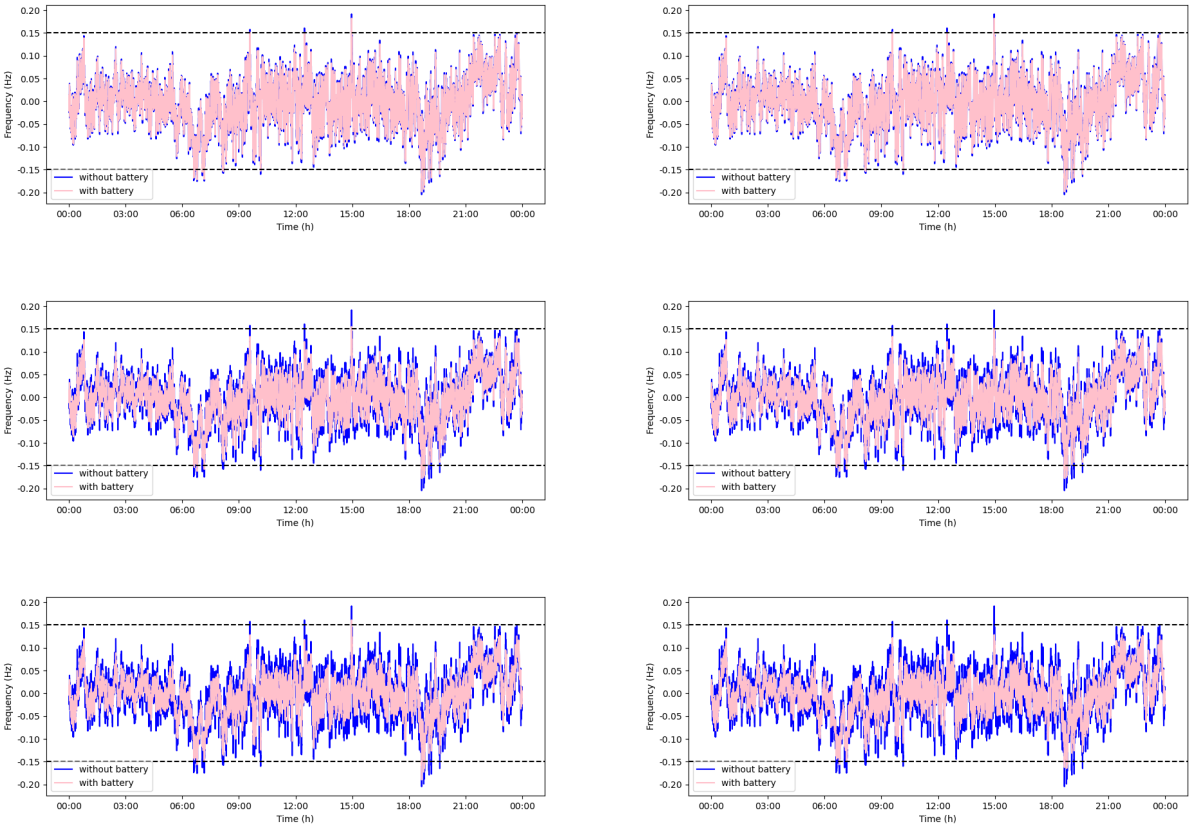

Figure 2: Frequency fluctuations with the small battery (left) and with the big battery (right), both of the same day. The first line of plots corresponds to the $\alpha = 0.5$ MWs simulations, the second line, to the $\alpha = 2.5$ MWs ones, and the third line, to the $\alpha = 4.5$ MWs ones.

In both situations, with the small and the big battery, we clearly perceive an improvement in frequency fluctuations as we keep increasing the value of α. Nevertheless, we can also appreciate that these frequency deviations are smaller in the bigger battery case, especially when $\alpha = 4.5$ MWs. However, we still have two battery properties to analyse.

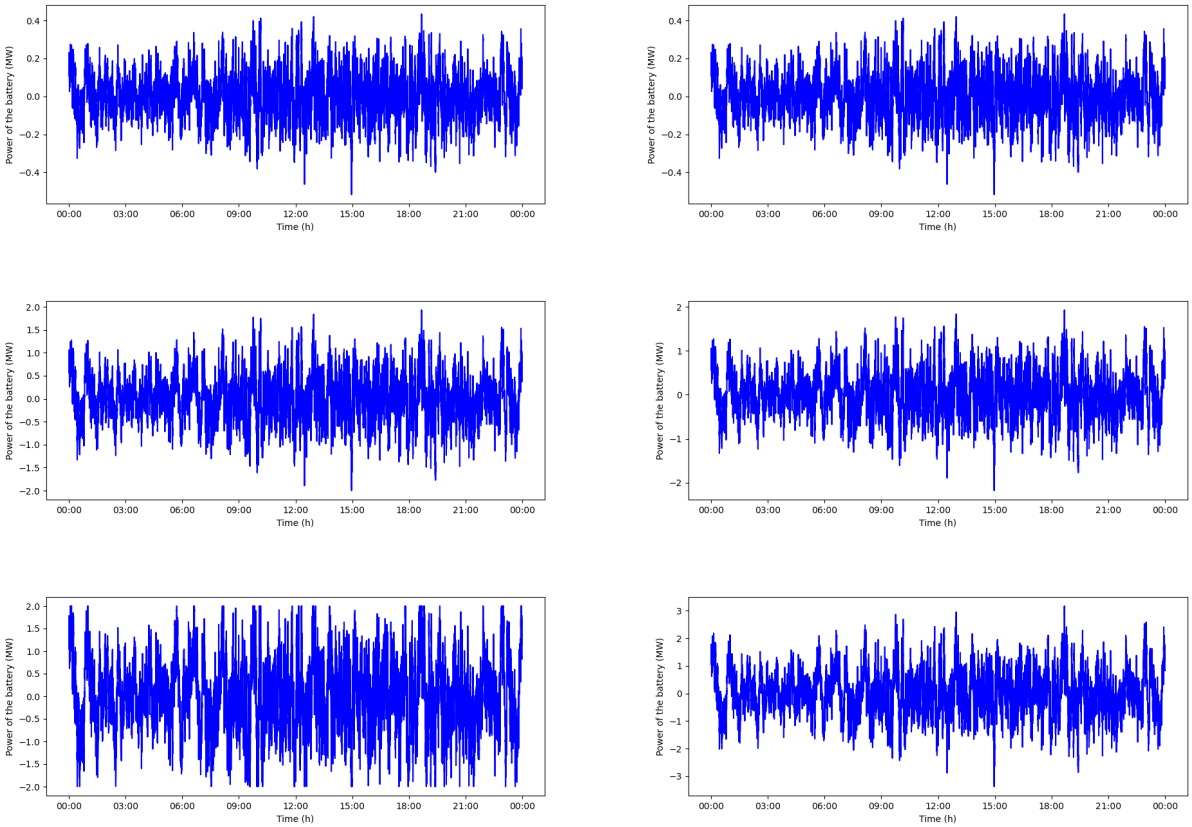

Figure 3: Instant power provided by the small battery (left) and by the big battery (right), both of the same day. The first line of plots corresponds to the $\alpha = 0.5$ MWs simulations, the second line, to the $\alpha = 2.5$ MWs ones, and the third line, to the $\alpha = 4.5$ MWs ones.

In tune with what we have learned from the frequency plots, we can barely notice differences between the performance of the two batteries in the first line of plots. Nonetheless, once we start to raise the value of α, we see that the small battery begins to work at its full capacity, reaching values of its instant power equal to its maximum power (2 MW), which causes the battery to age faster. On the contrary, the big battery never reaches its maximum power (20 MW) and its instant power oscillates within the 15% of it, which can help ensure its correct function.

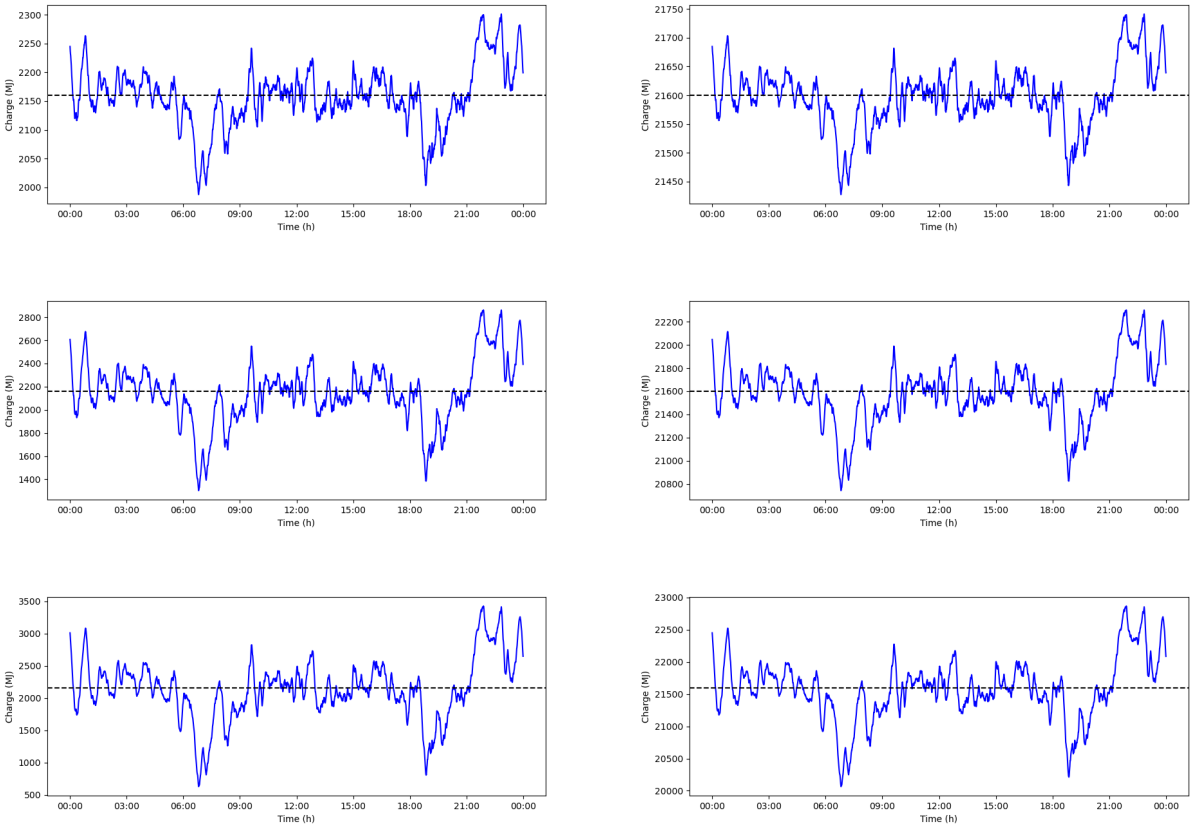

Figure 4: Instant charge of the small battery (left) and of the big battery (right), both of the same day. The first line of plots corresponds to the $\alpha = 0.5$ MWs simulations, the second line, to the $\alpha = 2.5$ MWs ones, and the third line, to the $\alpha = 4.5$ MWs ones.

Again, we observe the same behaviour we have seen so far. In the first line of plots, both batteries work similarly, whereas, when increasing α, the smaller battery charges and discharges almost completely (at some point, its charge is the 33% of its Q_{SP}) and the charge of the bigger one hardly oscillates (8%) around its Q_{SP}. Lastly, we look over the number of cycles each battery has completed in each case.

α (MWs)	Small	Big
0.5	22053	2206
2.5	93116	9422
4.5	146437	15049

Table 3: Number of cycles of the battery in each simulation.

Noticing that the number of cycles the small battery completes is ten times the bigger one' in all cases and considering all the plots shown above, we conclude that the big battery is the right choice. Although the reductions of the frequency fluctuations are nearly equal, the agings of the batteries are very different. The smaller battery would not last long, given all these peaks in its instant power and charge that damage it.

3.3 α determination

Now that we have settled the size of the battery, it is time to find out the most fitting value of α. In order to achieve that, we plot the frequency standard deviation, the rank of the absolute value of the frequency, and the RoCoF, aside from plotting the frequency fluctuations and the battery's power and charge. All these three new magnitudes are plotted against the without-battery simulation for

reference. The battery's parameters used in this section are all the same as the big one's except for α, which varies. The values of α are given in the next table.

Battery	α **(MWs)**
01	0.5
02	2.5
03	4.5
04	15.0
05	30.0
06	40.0
07	50.0

Table 4: Values of α used in our simulations.

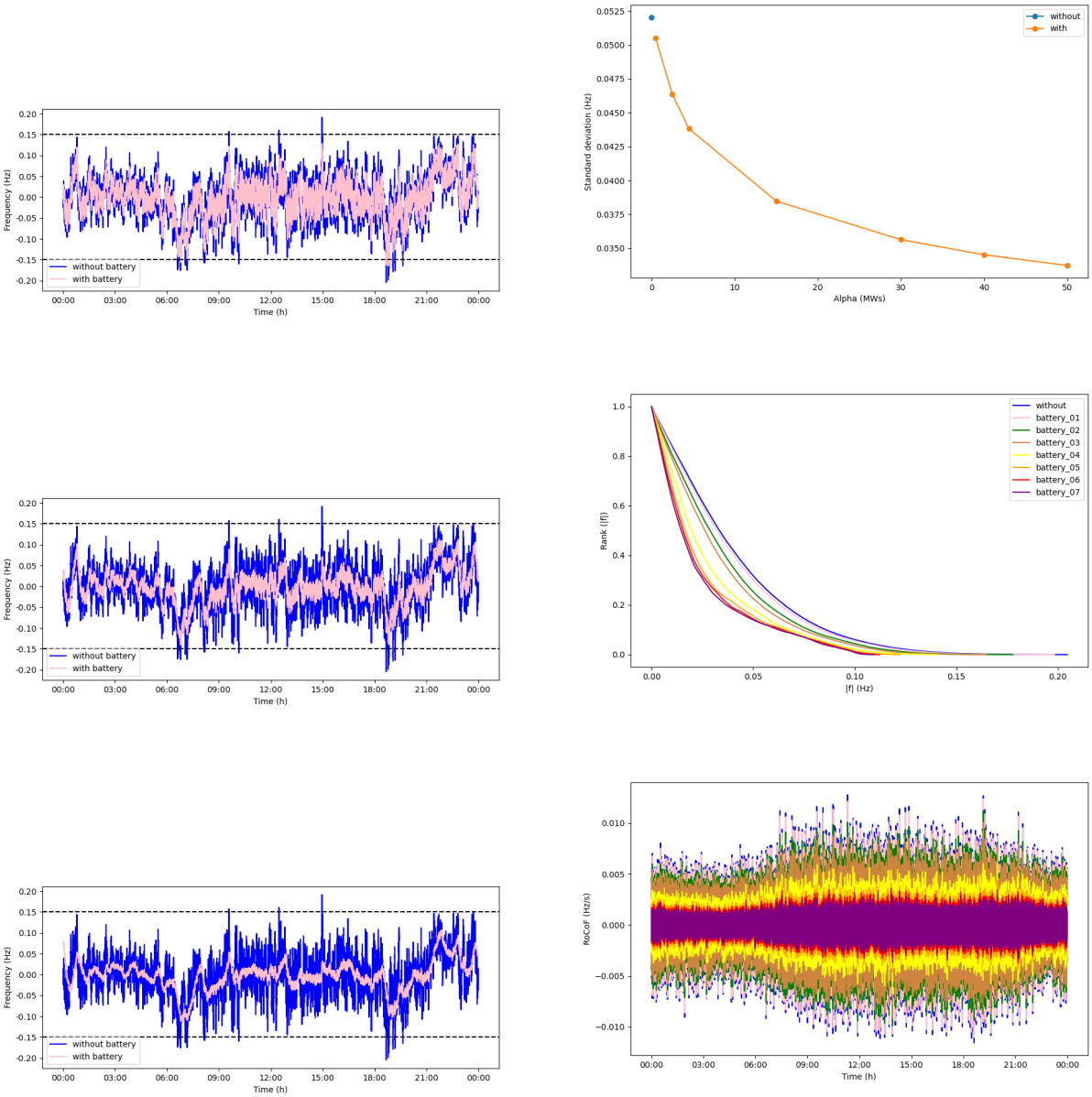

Figure 5: Frequency fluctuations (left) and standard deviation, rank, and RoCoF (right), all of the same day. The frequency fluctuations plots correspond to the cases $\alpha = 4.5$ MWs, $\alpha = 15.0$ MWs, and $\alpha = 40.0$ MWs, in order of appearance. The legend for the RoCoF plot is the same as the rank's.

Given that α is a parameter that depends on the grid' size, augmenting its value can help reduce the frequency fluctuations. That is exactly what we observe in all the plots above. Starting at values of $\alpha = 15.0$ MWs, the rapid frequency fluctuations have already vanished.

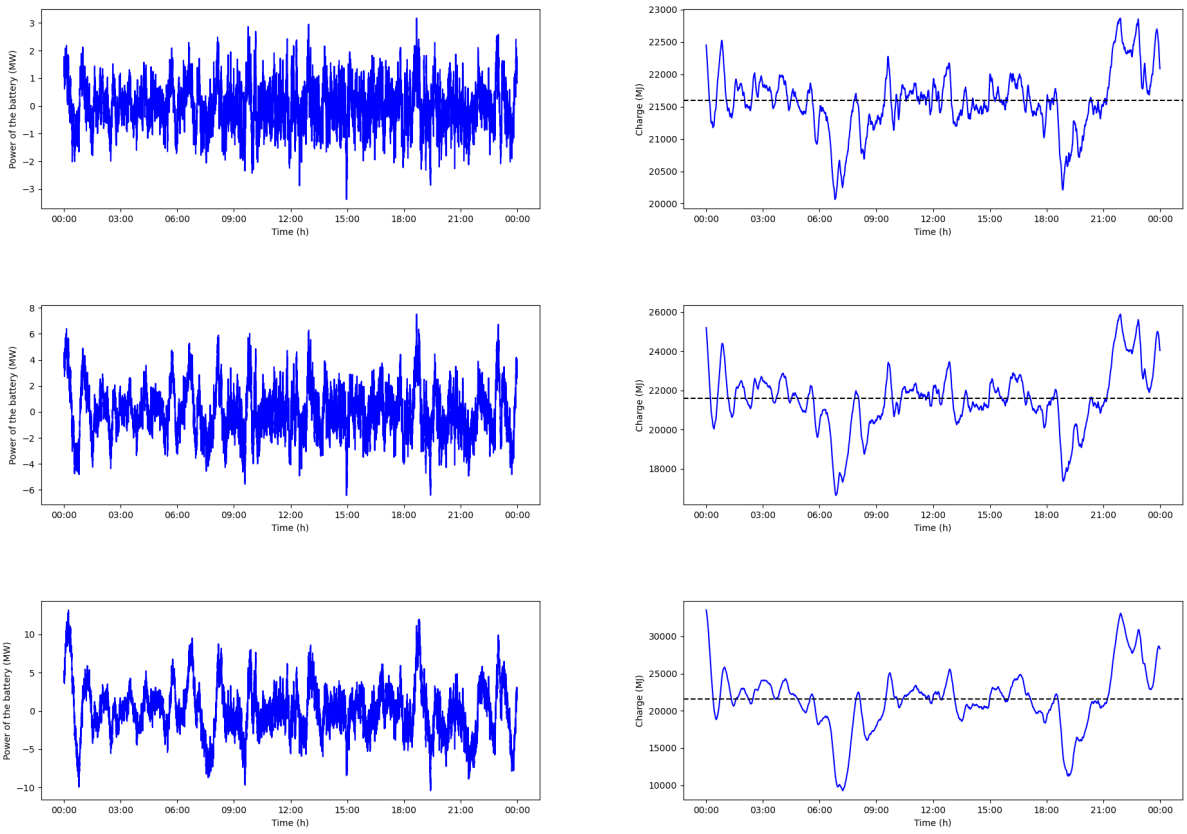

Figure 6: Instant power (left) and instant charge (right), both of the same day. The first line of plots corresponds to the $\alpha = 4.5$ MWs simulations, the second line, to the $\alpha = 15.0$ MWs ones, and the third line, to the $\alpha = 40.0$ MWs ones.

Even considering what we have said in the last paragraph, we now learn that, from $\alpha = 15.0$ MWs, the battery charges and discharges a great fraction of its Q_{SP} (54% in the last case shown), damaging itself, and, therefore, the fittest value for α is 4.5 MWs (only charges and discharges an 8% of its Q_{SP}). That is because it is adequate for decreasing the frequency fluctuations while not causing the battery to age so quickly. Another indicator of this characteristic is that the number of cycles the battery goes through increases with the value of α, as shown below.

α **(MWs)**	**Big**
0.5	2206
2.5	9422
4.5	15049
15.0	34688
30.0	51653
40.0	59476
50.0	65312

Table 5: Number of cycles of the battery in each simulation.

3.4 γ determination

Once we have determined the size of the battery and the value of α, we have to figure out the proper value of γ. In order to achieve that, we plot the frequency standard deviation, the rank of the absolute value of the frequency, and the RoCoF, aside from plotting the frequency fluctuations and the battery's power and charge. The battery's parameters used in this section are all the same as the big one's ($\alpha = 4.5$ MWs) except for γ, which varies. The values of γ used are shown below.

Battery	γ **(10^{-3} Hz)**
01	0.02
02	0.20
03	2.00
04	20.00
05	50.00
06	200.00
07	500.00

Table 6: Values of γ used in our simulations.

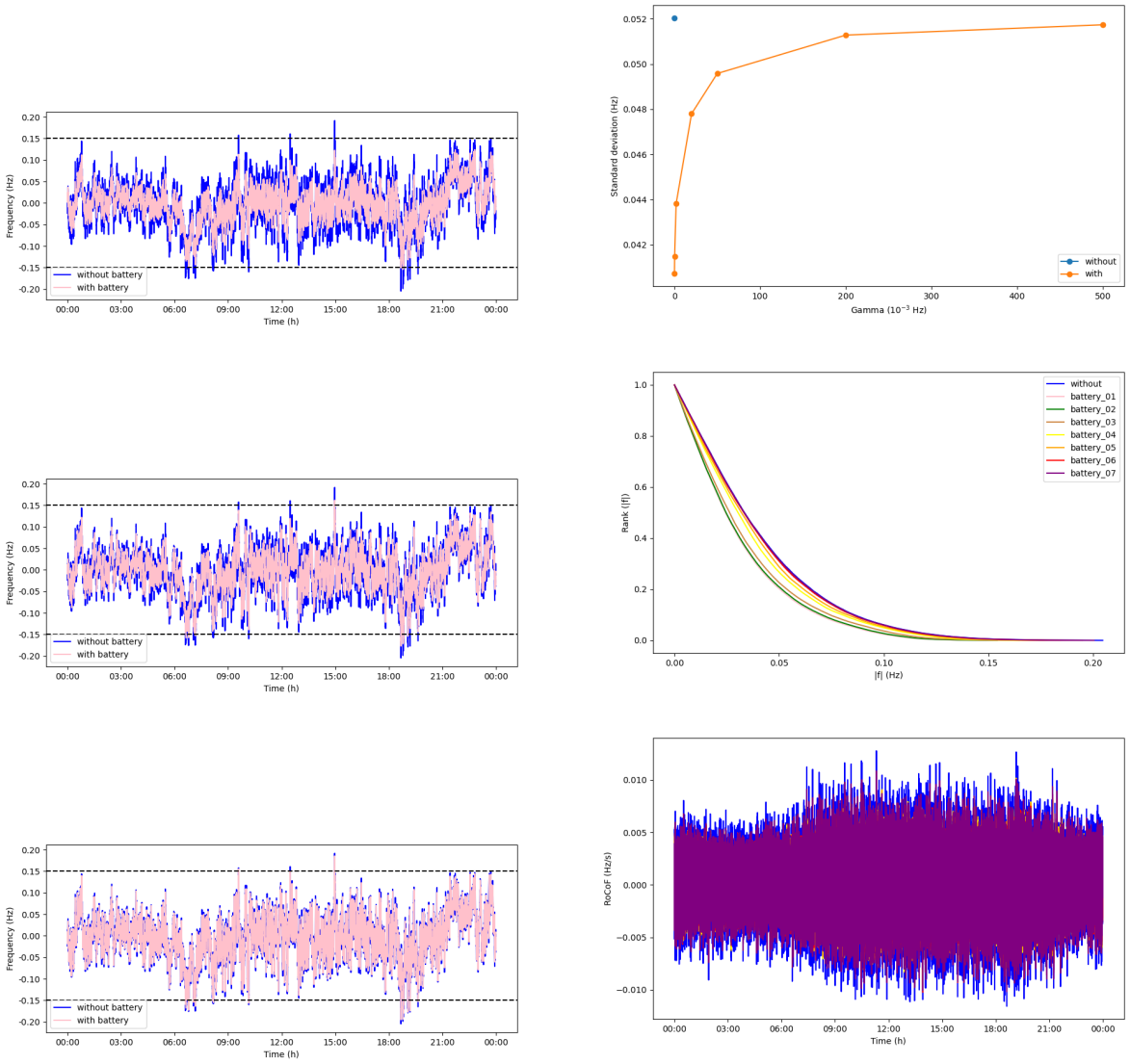

Figure 7: Frequency fluctuations (left) and standard deviation, rank, and RoCoF (right), all of the same day. The frequency fluctuations plots correspond to the cases $\gamma = 0.0002$ Hz, $\gamma = 0.02$ Hz, and $\gamma = 0.2$ Hz, in order of appearance. The legend for the RoCoF plot is the same as the rank's.

Opposed to what happens with α, augmenting γ increases the frequency fluctuations, as we see in all the plots above (this is why the plotting of battery 07 covers the others). As a result, we go after a smaller value of γ.

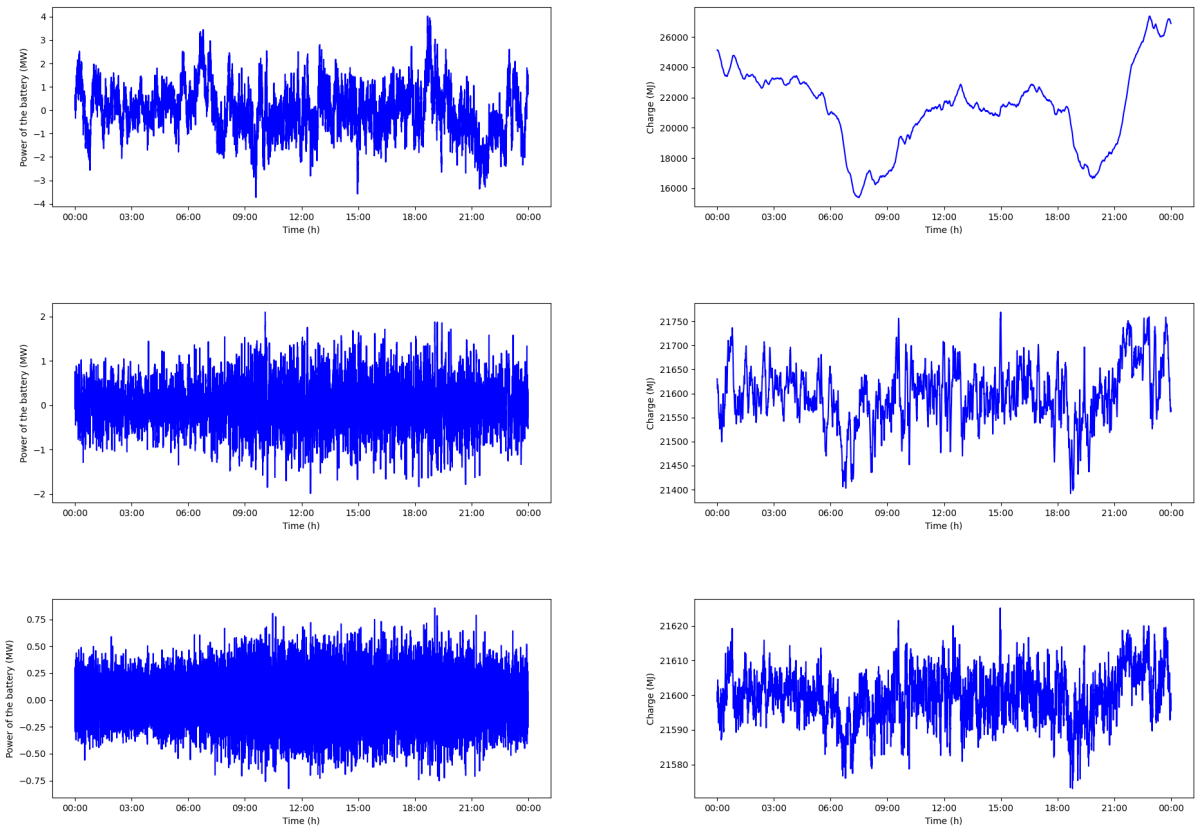

Figure 8: Instant power (left) and instant charge (right), both of the same day. The first line of plots corresponds to the $\gamma = 0.0002$ Hz simulations, the second line, to the $\gamma = 0.02$ Hz ones, and the third line, to the $\gamma = 0.2$ Hz ones.

Nevertheless, as we observe in the plots above, a smaller value of γ (first line of plots) implies bigger charges and discharges of the battery (26% in this case). In spite of this, bigger values of γ do not help to take profit of the battery, seeing that, in those cases, it never reaches a 10% of the maximum power. Another indicator of this characteristic is that the number of cycles the battery goes through decreases with the value of γ, as shown below. Consequently, the most befitting value of γ is 0.002 Hz.

γ (10^{-3} **Hz**)	**Big**
0.02	20764
0.20	19040
2.00	15049
20.00	9169
50.00	6802
200.00	3545
500.00	2011

Table 7: Number of cycles of the battery in each simulation.

To summarize, we show the final parameters of the battery in the next table.

Battery's parameters	Big
Q_{max} (MWs)	36000
$P_{b,max}$ (MW)	20
τ_b (s)	0.2
γ (Hz)	0.002
Q_{SP} (MWs)	21600
α (MWs)	4.5

Table 8: Values of the final battery's parameters.

3.5 Battery's effectiveness

To conclude this search for the most appropriate battery, we calculate the standard deviation of frequency fluctuations for the ten different wind power scenarios simulated before, without and with battery.

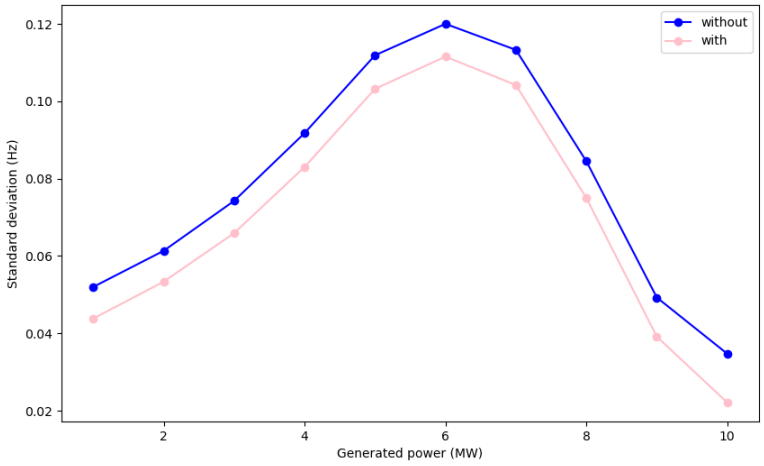

Figure 9: Standard deviation of frequency fluctuations for increasing wind power generation.

We can easily notice that, regardless of the generated wind power, the battery always succeeds in reducing the frequency fluctuations, as we expected.

4 Conclusions

With all the ongoing VRES research efforts, we have been able to offer useful insights on the topic by modeling the power grid with realistic representations and using real data. Furthermore, we have simulated different cases and learned from them to understand the theoretical model better. Finally, we have found an adequate battery for Gran Canaria's power grid that can help reduce frequency fluctuations.

The power grid, continuously adapting to meet the changing demand needs, has to be accurately modeled and simulated in very different scenarios. Some of them could involve: transmission line stress, closing of conventional generators, increasing photovoltaic generation, a grid connected to the mainland, large inter-area power imbalances...

Other approaches in order to balance VRES fluctuations instead of storage control are the integration of demand-side technologies with smart charging, energy efficiency measures, and potential infrastructure upgrades.

Acknowledgments

Acknowledge support and useful discussions with my both supervisors María Martínez Barbeito and Pere Colet Rafecas.

This work was supported by the SURF@IFISC fellowship.

References

[1] M. Martínez-Barbeito. *Power grid dynamics and stability with a high penetration of renewable energies.* To be published. (2024).

[2] M. Martínez-Barbeito, D. Gomila, and P. Colet, *Dynamical model for power grid frequency fluctuations: Application to islands with high penetration of wind generation.* IEEE Transactions on Sustainable Energy, vol. 14, no. 3, pp. 1436–1445 (2023).

Entanglement classification with quantum reservoir computing

Ernest Staffetti Cruañas, Gianluca Giorgi, Ricard Ravell
Instituto de Física Interdisciplinar y Sistemas Complejos, IFISC (CSIC-UIB)
Campus Universitat de les Illes Balears, E-07122 Palma de Mallorca, Spain

Abstract

Reservoir Computing constitutes a cost-efficient alternative to Recurrent Neural Networks that has been shown to work well for tasks such as time series prediction. In recent times, the use of quantum systems as reservoirs has allowed to efficiently solve purely quantum tasks with this machine learning scheme. One of these tasks is entanglement classification. In this work, we use a spin network as a reservoir, and study how it performs at classifying the entanglement of two-qubit states. In particular, we pay special attention to the impact of the internal memory of the reservoir in the accuracy of the classification for different families of states.

1 Introduction

The basic idea of Reservoir Computing (RC) is to replace the deep hidden layers in a Recurrent Neural Network (RNN) with a complex physical system that automatically processes the input information through its evolution, without the need to optimize any weights. This system is called reservoir. Although this approach doesn't work for every machine learning task, it has been shown to function really well for time series prediction. The advantage lies in the training process, which is reduced to solving a linear system of equations to find the optimal weights for the output layer, as opposed to the computationally demanding backpropagation methods used in RNNs.

The RC scheme consists of three basic layers. First, an input layer, where the information is encoded into some degrees of freedom of the reservoir. Then, the reservoir layer, where the information is processed via the natural evolution of a physical system. If the system consists of multiple nodes, its evolution in time will naturally include recursion, which is the key element that allows RNN to retain information about multiple past inputs. That is, the reservoir will have memory, which explains its usefulness in time series prediction. Additionally, the reservoir should have the following three properties [4]:

- Non-linear processing: the reservoir should transform the input non-linearly.
- Separability: different inputs should be processed to different outputs.
- Fading memory: the performance of the algorithm should be independent of the initial conditions of the reservoir, that is, its state before inserting the input. Thus, the reservoir should only have short-term memory, forgetting about its long-past states.

Finally, we have an output layer, where some quantities x_i of the reservoir are measured. The final output, Y, of the scheme is usually obtained as a linear combination of these quantities. The weights of this linear combination are contained in a matrix of coefficients, W. During the training step, we modify W using linear regression so that the outputs of the scheme match the desired values. This training procedure is very simple and efficient compared to the usual RNN backpropagation strategy.

RC can be performed using a wide range of physical systems as reservoirs. The ultimate goal is to choose a system that will map the input into a much bigger state space, allowing the machine to clearly separate the information, distinguish between different inputs, and learn effectively as a consequence. Quantum systems satisfy this requirement particularly well, as the dimension of the Hilbert space of a system of N spin particles grows exponentially with the number of them. For spin-1/2 particles, this is 2^N. The fact that the degrees of freedom of a quantum reservoir increase exponentially with its size means that this type of reservoir will require less nodes in order to outperform other reservoir systems. Besides that, quantum reservoirs allow to solve both classical

and purely quantum tasks, as they can take quantum states as inputs. The goal of this project is to study the application of Quantum Reservoir Computing (QRC) to classifying the entanglement of a two-qubit quantum state. The code developed can be found in the following repository: `https://github.com/estaffet/QRC_entanglement_classification.git`

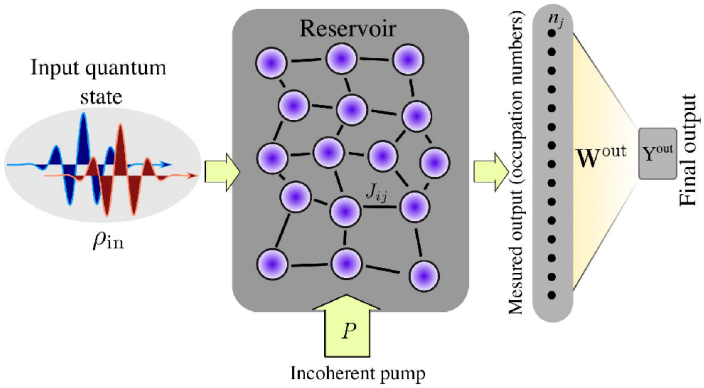

Figure 1: Quantum Reservoir Computing scheme. Taken from [2].

2 Theoretical model

2.1 Ising model

It has been shown that fully-connected transverse-field Ising lattices work well as quantum reservoirs. These are described by the following Hamiltonian [3]:

$$H = \sum_{i,j} J_{ij} X_i X_j + h \sum_i Z_i \,, \tag{2.1}$$

where X_i and Z_i represent the spin operators along the x and z directions, respectively, for the i-th spin of the lattice. For spin-1/2 particles, these operators are the Pauli matrices. The coupling matrix $(J)_{ij}$ is random, and allows for interactions between any pair of spins, as opposed to the usual nearest neighbour approximation. Its entries are randomly drawn from the uniform distribution in the interval [0,1].

Let's first discuss the common use case of time series prediction. If we wanted to analyze a sequence $u = (u_0, u_1, \ldots, u_k, \ldots)$, at each time step $t = k\Delta t$ (with $k = 1, 2, 3, \ldots$) the state of the first node in the lattice would be replaced by $|\psi_k\rangle = \sqrt{1-u_k}\,|0\rangle + \sqrt{u_k}\,|1\rangle$. This is achieved by taking the partial trace over all spins except the first one. Between each time step, the reservoir is left to evolve naturally. In this way, the state of the reservoir at the k-th step will be influenced by all the previous elements in the sequence. Thus, the reservoir processes the entire sequence simultaneously, keeping memory of its past states, which explains its usefulness in time series predictions [1].

In our present case, the target task is not temporal, meaning that the memory of the dynamical system is not required in principle. The input data will be two-qubit quantum states, and the targets will either be binary classification labels (entangled/separable) or some numerical entanglement measure that characterizes the states. This type of scheme is known as Extreme Learning Machine (ELM). However, inspired by the time series prediction protocol, it is plausible that reinserting the same input multiple times at different time steps might improve the performance of this classification algorithm, especially for complex quantum states. For the purpose of evaluating the impact of input reinsertion, we will start working with Werner states. These are two-qubit states that are parametrized by a single parameter. For this reason, its classification in the training process should be simple enough for the reservoir to not need reinsertion. Then, we will study more complex families of two qubit-states, dependent on more than one parameter. The goal is to analyize if reinsertion improves classification in these cases, and determine the optimal number of reinsertions.

2.2 Approach

First, the reservoir is initialized to a random state, ρ_0. Then, we take the partial trace over all spins except the first two, and inject the input state, ρ_{input}, there. Explicitly, the reservoir is left in the following state:

$$\rho = \rho_{input} \otimes \mathrm{Tr}_{1,2}\{\rho_0\}\,. \tag{2.2}$$

where the notation Tr_x indicates the partial trace over all spins except those in the subindex. Next, the reservoir is left to evolve for a time Δt following the dynamics of the Hamiltonian, obtaining:

$$\rho(\Delta t) = e^{-iH\Delta t}[\rho_{input} \otimes \mathrm{Tr}_{1,2}\{\rho_0\}]e^{iH\Delta t}\,. \tag{2.3}$$

After this time interval, we extract some data from the reservoir by measuring different observables O_j over each spin:

$$x_j = \mathrm{Tr}[O_j\rho(\Delta t)]\,. \tag{2.4}$$

This data is then linearly combined with weights w_i to produce the final scalar output. These weights are optimized in the training step to best match the desired outputs for the set of training inputs. In our case, we measured X_i, Y_i and Z_i over each of the spins. In practice, in the training step we repeat the mentioned process with multiple inputs, building a matrix of observables:

$$X = \begin{pmatrix} \mathrm{Tr}[O_1\rho^{(1)}(\Delta t)] & \mathrm{Tr}[O_2\rho^{(1)}(\Delta t)] & \dots & \mathrm{Tr}[O_k\rho^{(1)}(\Delta t)] & 1 \\ \mathrm{Tr}[O_1\rho^{(2)}(\Delta t)] & \mathrm{Tr}[O_2\rho^{(2)}(\Delta t)] & \dots & \mathrm{Tr}[O_k\rho^{(2)}(\Delta t)] & 1 \\ \vdots & \ddots & \dots & \vdots & \vdots \\ \mathrm{Tr}[O_1\rho^{(M)}(\Delta t)] & \mathrm{Tr}[O_2\rho^{(M)}(\Delta t)] & \dots & \mathrm{Tr}[O_k\rho^{(M)}(\Delta t)] & 1 \end{pmatrix}, \tag{2.5}$$

where the superscript that ranges from 1 to M labels the different input states used for training. Additionally, an extra column has been included in the matrix to account for the independent term of the linear regression:

$$Y = XW \tag{2.6}$$

where Y are the targets of the training step, and W is a vector of weights.

If we wanted to reinsert the input, we would repeat the previous steps iteratively by taking the partial trace at the end of each evolution interval, and end up with the following state:

$$\rho(k\Delta t) = e^{-iH\Delta t}[\rho_{input} \otimes \mathrm{Tr}_{1,2}\{\rho((k-1)\Delta t)\}]e^{iH\Delta t}\,. \tag{2.7}$$

3 Results and discussion

3.1 Werner states

The first goal was to classify the entanglement of uniparametric 2-qubit states known as Werner states. These are given by the following expression:

$$\rho_W(\lambda) = \lambda\left|\psi^-\right\rangle\left\langle\psi^-\right| + \frac{1-\lambda}{4}\ \mathbb{1}, \tag{3.1}$$

where

$$\left|\psi^-\right\rangle = \frac{1}{\sqrt{2}}(|01\rangle - |10\rangle) \tag{3.2}$$

is a Bell state (maximally entangled), and $\lambda \in [-1/3, 1]$. These states are separable for $\lambda \leq 1/3$ and entangled for $\lambda > 1/3$. Since this family of states depends on a single parameter, one insertion of the input should be enough for the reservoir to classify them correctly. In fact, since this task should be fairly easy for a quantum reservoir, the goal was to predict directly the value of the parameter λ given an input Werner state. The following figure shows the predictions in the training and testing steps. Since the estimation is almost perfect, the target and predicted values overlap in the graphs.

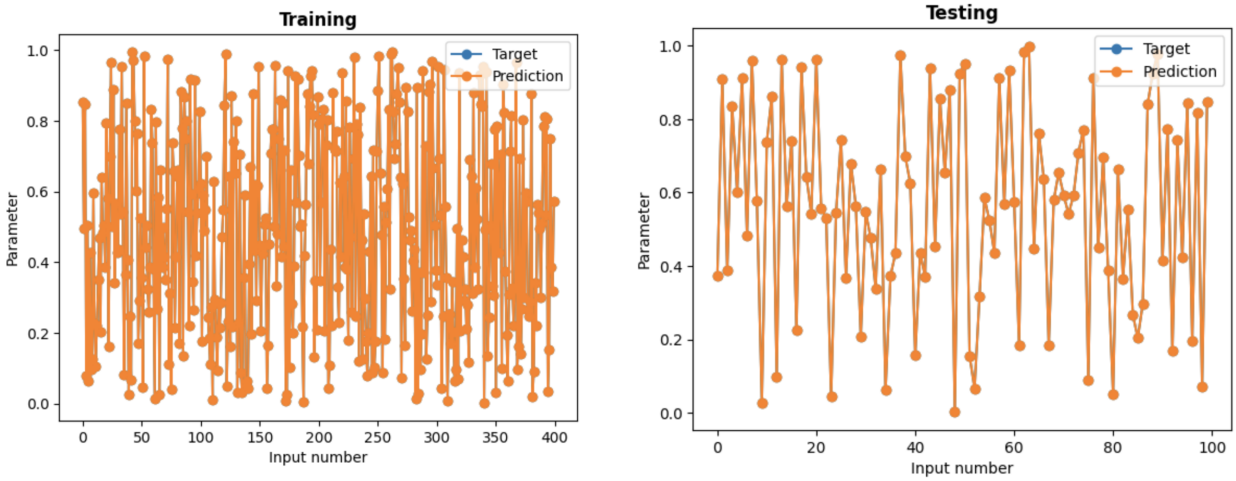

Figure 2: Training and testing stages for Werner states.

The prediction is really good, with a MSE[1] of 10^{-19}. To obtain this result, we have used a reservoir of $N = 6$ spins.

3.2 Cross states

After this first example, we move on to more complex 2-qubit states. Instead of one parameter, we now define the so called cross-states, which depend on 3 independent parameters. Their general density matrix is:

$$\rho_C = \begin{pmatrix} p & 0 & 0 & c_1 \\ 0 & q & c_2 & 0 \\ 0 & c_2 & q & 0 \\ c_1 & 0 & 0 & p \end{pmatrix}, \quad \text{with } p + q = 1, c_1 \leq |p|, c_2 \leq |q|. \tag{3.3}$$

The last two conditions on the non-diagonal elements come from the general requirement ($\rho_{14} \leq \sqrt{\rho_{11}\rho_{44}}$ and $\rho_{23} \leq \sqrt{\rho_{22}\rho_{33}}$) for the density matrix to represent a physical state.

In this case, it will be necessary to insert the input multiple times to obtain accurate results. That is, instead of measuring the reservoir after the first evolution, we take the partial trace again over all spins but the first two, and reinsert the input on the first two qubits. Then we let the reservoir evolve again, and repeat this process as many times as necessary.

3.2.1 Entanglement metrics

In order to characterize the level of entanglement of a bipartite system like ours, we use two different metrics: concurrence and negativity, both defined for a two-qubit state ρ [5].

- **Concurrence.** Defined as:

$$C(\rho) := \max(0, \lambda_1 - \lambda_2 - \lambda_3 - \lambda_4), \tag{3.4}$$

where $\lambda_1, \ldots, \lambda_4$ are the eigenvalues, in decreasing order, of the following Hermitian matrix:

$$R = \sqrt{\sqrt{\rho}\tilde{\rho}\sqrt{\rho}}, \tag{3.5}$$

and

$$\tilde{\rho} = (\sigma_y \otimes \sigma_y)\rho^*(\sigma_y \otimes \sigma_y). \tag{3.6}$$

[1]Computed over a set of 100 input states in the testing phase by comparing the difference between their actual λ parameter and the prediction.

- **Negativity.** Defined as the absolute sum of the negative eigenvalues of the partially transposed density matrix:

$$\mathcal{N}(\rho) = \sum_i \frac{|\lambda_i| - \lambda_i}{2} \tag{3.7}$$

If the negativity is 0, the state is separable. On the other hand, for entangled states it is < 0.

The classification task was seen to work much better when using negativity as a metric, so in this report we will not comment the results obtained with the concurrence. We want to classify the states in entangled or separable, without predicting directly any entanglement metric or parameter. For this purpose, we train the reservoir by assigning the vector $Y = [1, 0]$ to separable states, and $Y = [0, 1]$ to entangled states. In the testing phase, the reservoir will provide as output a 2D vector. If the first element of this vector is larger than the other, the input state is classified as separable. Otherwise, it is considered to be entangled.

3.2.2 Results

The next figures show the evolution of the classification accuracy as the number of input reinsertions is increased. We see that inserting the input multiple times in fact improves the performance of the algorithm, which makes no mistakes with 3 iterations. This has been seen to be the tendency for this family of two-qubit states. Figure 6 shows the performance of the algorithm when asked to predict the negativity of the input states directly, with 3 input insertions. The MSE in this case is of the order of 10^{-3}.

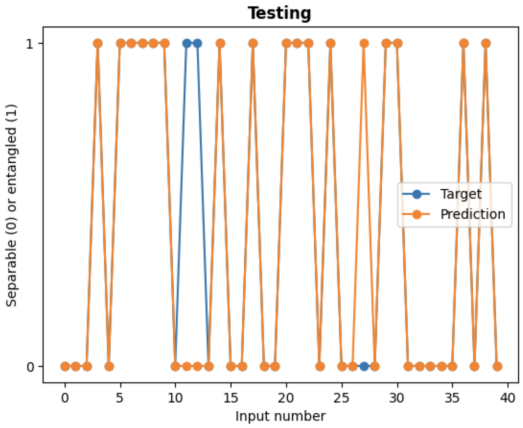

Figure 3: 1 iteration: 3 mistakes.

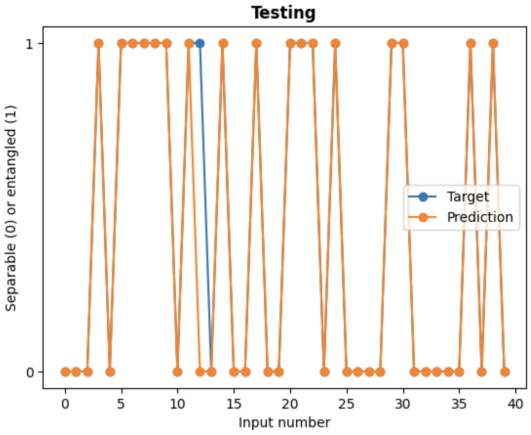

Figure 4: 2 iterations: 1 mistake.

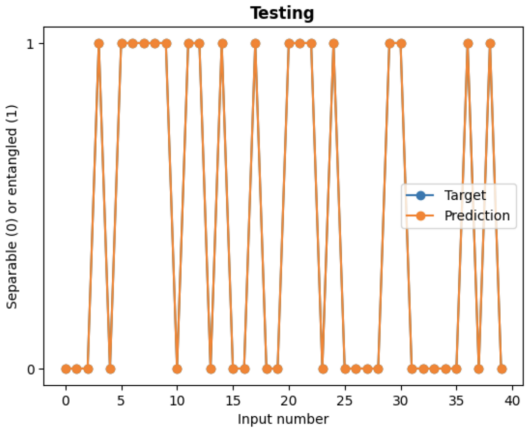

Figure 5: 3 iterations: no mistakes.

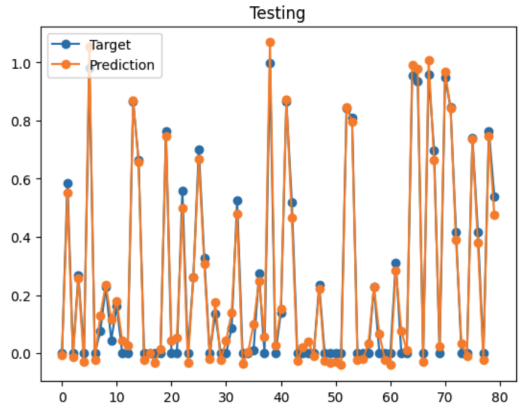

Figure 6: Prediction of negativity for 3 iterations.

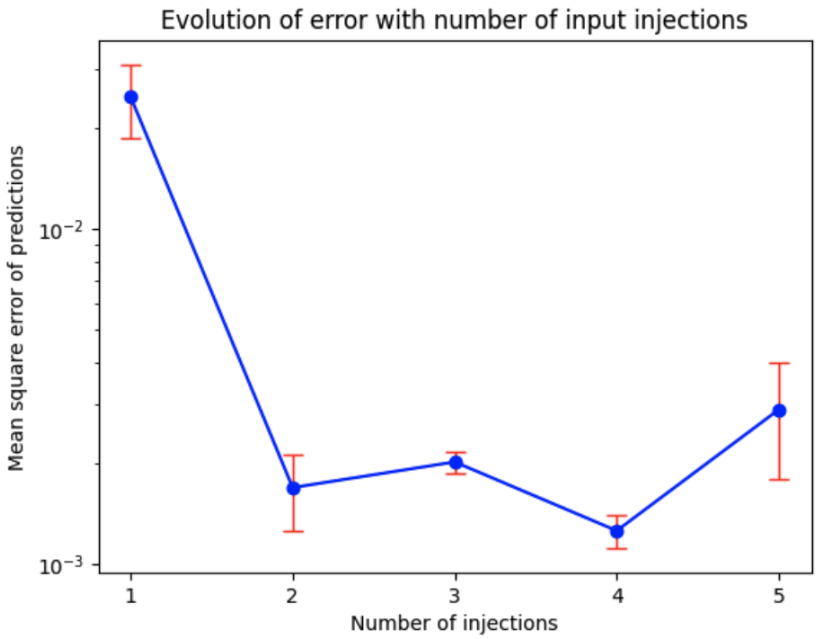

Figure 7: Evolution of error with number of inputs.

In order to generalize the previous observations, we perform a statistical average of the MSE for the negativity prediction over multiple random seeds (which modifies the coupling matrix of the Hamiltonian, and thus the structure of the reservoir lattice). Figure 7 shows the evolution of this average with the number of input reinsertions. As seen previously, reinserting the input improves the performance, 4 times being the optimal number. Beyond this number, the MSE seems to increase.

4 Conclusions

This work has shown that the memory of the reservoir turns out to be useful for classification tasks which are not temporal in nature. This is true at least for the entanglement classification task under study. Further work could consist in analyzing the performance of this scheme with other families of quantum states, in order to generalize the conclusions achieved thus far. It has also become clear that the metric used to quantify entanglement plays an important role in the accuracy of the classification. It would also be interesting to study which properties make a metric stand out, and if this advantage depends on the underlying quantum system of the reservoir. Additionally, not much attention was paid to the hyperparameters associated to the Ising lattice, like the intensity of the transverse magnetic field or the range of values of the elements in the coupling matrix. A more thorough inspection could have found values for which the algorithm worked better.

Acknowledgments

This work was supported by the SURF@IFISC fellowship. Thanks to Gianluca and Ricard for their attention and guidance. Thanks also to my internship mates for the insightful discussions.

References

[1] Keisuke Fujii and Kohei Nakajima. Harnessing disordered-ensemble quantum dynamics for machine learning. *Physical Review Applied*, 8(2), August 2017.

[2] Sanjib Ghosh, Andrzej Opala, Michał Matuszewski, Tomasz Paterek, and Timothy C. H. Liew. Quantum reservoir processing. *npj Quantum Information*, 5(1), April 2019.

[3] Rodrigo Martínez-Peña, Gian Luca Giorgi, Johannes Nokkala, Miguel C. Soriano, and Roberta Zambrini. Dynamical phase transitions in quantum reservoir computing. *Physical Review Letters*, 127(10), August 2021.

[4] Pere Mujal, Rodrigo Martínez-Peña, Johannes Nokkala, Jorge García-Beni, Gian Luca Giorgi, Miguel C. Soriano, and Roberta Zambrini. Opportunities in quantum reservoir computing and extreme learning machines. *Advanced Quantum Technologies*, 4(8), June 2021.

[5] William K. Wootters. Entanglement of formation of an arbitrary state of two qubits. *Physical Review Letters*, 80(10):2245–2248, March 1998.

Spatiotemporal Dynamics: Applications to vegetation population dynamics

Andreu Fiol, Damià Gomila and Daniel Ruiz-Reynés
Instituto de Física Interdisciplinar y Sistemas Complejos, IFISC (CSIC-UIB)
Campus Universitat de les Illes Balears, E-07122 Palma de Mallorca, Spain

Abstract

Inhomogeneities in vegetation meadows, like fairy rings, appear spontaneously in all kinds of enviroments and they provide vital information about the ecosystem's health. Monitoring them allows us to identify growth and risk factors. These patterns, that appear both in drylands and underseas, can have many different triggers like soil composition, animal or human intervention or water-biomass feedback.
Spatial heterogeneity and patterns are also present in Posidonia oceanica meadows in the Mediterranean sea. This seagrass is a key element of the Mediterranean ecosystem. Identifying posidonia's dynamics is essential to preserve the marine environment.
Our objective is to explore if the same dynamics between sulfide accumulation in the sediment and seagrass growth used by Ruiz-Reynés et al. to describe rings of posidonia that propagate through bare soil can result in the opposite pattern: arcs of bare soil propagating through an homogeneous meadow that have been observed in the Balearic coasts.
In this work we analyze how the system's behavior changes with the active removal of sulfides due to vegetation presence, which has not been studied before.

1 Introduction

Posidonia oceanica is a species of seagrass that is of particular interest due to it's abundance in the Mediterranean ecosystems. it has a big impact in the environment's health as large meadows of posidonia fix the values of CO2, produce large quantities of oxygen and protect the soil as well as the fish that live around it, accumulating large quantities of biomass. It is commonly used as a marker to determine the state and health of marine ecosystems. It occupies a portion of the Mediterranean under sea, growing both in large homogeneous meadows or forming varied heterogeneous patterns in different regions.

When under favorable conditions, vegetation tends to occupy all available space, forming large homogeneous meadows. However, once we add spatial-extended negative feedback in the equation like toxic sediment, resource limitation, human intervention or animal grazing, inhomogeneities can emerge spontaneously forming a wide variety of particular patterns like fairy circles in the Namibian desert, which Juergens associated with the intervention of termites [3], other fairy circles in Australia associated with a different biomass-water feedback [4], or vegetation labyrinths in northern Negev.

These dynamics are vital, providing a smooth transition between the homogeneous meadow and a bare landscape, allowing for intermediate states when not all conditions are favorable to the vegetation's development, for example, fairy circles in the Namibian desert can survive through many decades of drought. So, in understanding them, we can assess the ecosystem's health and functioning, identify the factors that allow for vegetation growth as well as risk factors that could endanger it.
Due to their complexity and sensibility to many conditions like temperature, precipitation, soil composition or animal participation, these systems can have a very sensible equilibrium that could disappear with a minor change in the environment. That is why it is so important to understand and monitor these systems. Even more now that climate change is rising the temperature and producing changes at a global scale. The total disappearance of vegetation would be catastrophic for their ecosystem.

Though this patterns are mostly known in deserts and drylands, where they have been studied extensively, similar patterns appear underseas in seagrass meadows, although a different mechanism must be considered other than the competition for water that drives these dynamics in drylands. Among these patterns, there are fairy circles, which have been observed in the Corsican coast (Mediterranean sea) in meadows of Posidonia oceanica [5] [6], or ring-like pulses of posidonia propagating through bare soil in the coasts of the balearic islands (Fig. 1).
A recent study by Ruiz-Reynés et al. has shown that the spatiotemporal dynamics of these rings is associated to excitable dynamics resulting from the interaction between seagrass growth and sulfide accumulation in the sediment [1].

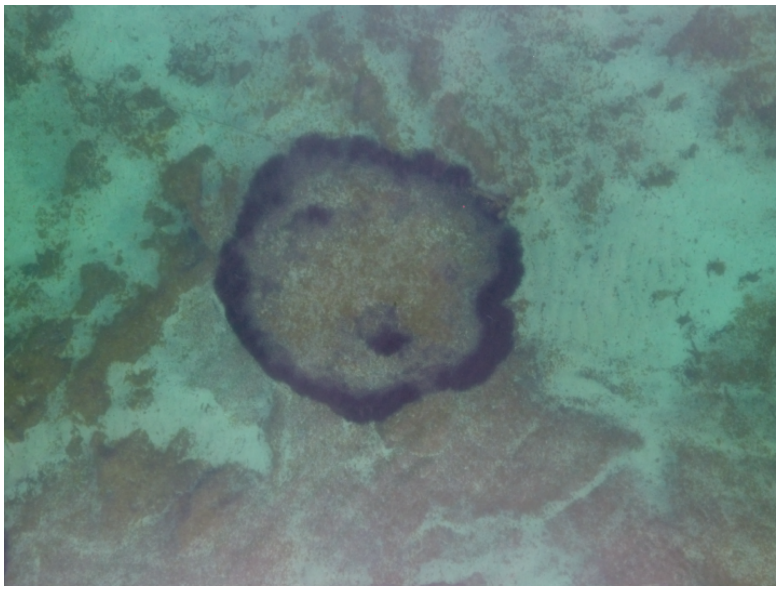

Figure 1: Excitable ring. High-resolution 2021 drone image of an excitable ring of Posidonia oceanica in the Pollença bay. [1]

Hydrogen sulfides are toxic to seagrass. As the plant absorbs them, they inhibit growth and increase mortality. However they are closely connected as they are the main byproduct of bacteria in seagrass sediment: when the plant dies and decomposes, sulfides are generated. However as the plant grows it also absorbs sulfides, reducing its concentration. Under the right conditions, which typically require high input of organic matter, mathematical modelling predicts the emergence of the aforementioned excitable behaviour.
Consider the formation of a patch of seagrass. It's center saturates and, as the concentration of sulfides raises, the plant decays and starts to die outward form the center. However, as the center of the region dies, its perimeter also grows towards the surrounding soil, which is less rich in sulfides, resulting in a ring of vegetation that grows radially [1].

This project emerges from the results obtained by Ruiz-Reynés et al., successfully relating the dynamics of these propagating rings of posidonia with the interaction between seagrass growth and sulfide concentration.
The idea we explore in this project is that a similar coupled mechanism can form the inverted pattern: arcs of bare soil that propagate through an homogeneous meadow of seagrass. These patterns have also been observed along the Balearic coasts (Fig. 2).
We use the same mathematical model to describe the interaction between seagrass and sulfides to see if excitability compatible with the propagating arcs is related to the active removal of sulfides due to vegetation. The effects of this term have not been analyzed before and in this work we see that when this term is largely increased, it allows for the inverted patterns we where searching for. These arcs would account for a patch of vegetation that transitionally vanishes into bare soil before it grows again, stabilizing in an homogeneous state.

Figure 2: Arcs of bare soil in an homogeneous meadow of Posidonia oceanica. Satellite image from Google Maps of the Pollença bay.

2 Theoretical model

The theoretical model used to describe the dynamics of the vegetation density is composed of two coupled partial differential equations describing the time evolution of vegetation density and sulfide concentration [1]:

$$\partial_t n = (\omega_b - \omega_d(n,S))n + d_0\nabla^2 n + d_1(n\nabla^2 n + |\nabla n|^2) \tag{2.1}$$

$$\partial_t S = c_s\omega_d(n,S)n + P_s - \delta_s S - \delta_0 nS + D_s\nabla^2 S \tag{2.2}$$

Where ω_b is the branching rate, $\delta_s + \delta_0 n$ is the removal rate of sulfides, P_s is the external input of sulfides (which is assumed constant) and ω_d is the mortality rate as a function of the vegetation density and the sulfide concentration:

$$\omega_d(n,S) = \omega_{d0} - \frac{\omega_{d0} an}{1+an} + bn^2 + \gamma S \tag{2.3}$$

ω_{d0} is the intrinsic mortality rate of the plant, γ is the sensibility of the plant to sulfides, bn^2 is a saturation term for large values of density and $\frac{\omega_{d0}an}{1+an}$ is a facilitative, self-saturating term: it grows linearly with n until it saturates to the value of ω_{d0} for large values of density.

For simplicity, spatial terms were not considered in this work ($d_0, d_1, D_s = 0$) so the resulting system is composed of two coupled, first-order differential equations, with nine parameters remaining. In this project we focused on how the model's stability changes with the intrinsic mortality rate, ω_{d0}, and how the active removal of sulfides due to vegetation, δ_0, affects the dynamical regimes.

2.1 Stability analysis and bifurcation theory were used to determine the different dynamical regimes of the system

Fixed points are those where the system remains constant. They can be stable, when the system evolves towards the fixed point and tends to stay there. Or they can be unstable, meaning that the system will evolve away from those points at the smallest perturbation [2].
The fixed points, which would account for a steady solution where the vegetation density has a constant value, can be found by solving the equations $\partial_t n^* = 0$, for which we have $\omega_d(n^*, S^*) = \omega_d^* = \omega_b$, and $\partial_t S^* = 0$. Keeping in mind that the bare soil solution, $n = 0$, is always a fixed point, independent of the parameters, the other fixed points are given by:

$$\omega_{d0} = \left(\omega_b - bn^{*2} - \gamma\frac{c_s\omega_b n^* + P_s}{\delta_0 n^* + \delta_s}\right)(1 + an^*) \tag{2.4}$$

Where we used that $S^* = \frac{c_s n^*\omega_b + P_s}{\delta_0 n^* + \delta_s}$, which can be derived from $\partial_t S^* = 0$.
Notice that this equation gives us the inverse expression of the bifurcation diagram, $\omega_{d0}(n^*)$, but we cannot isolate the fixed points, $n^*(\omega_{d0})$. However, we can solve it numerically by simply using an array of values of n^*, calculating the respective ω_{d0} and then plotting the parameter in the X axis instead of the Y axis.

To study the stability of these fixed points, we study the respective eigenvalues using linear stability analysis: considering a pertorbation of the type $n = n^* + \delta n$ and $S = S^* + \delta S$, doing a first order aproximation around the fixed point (Taylor expansion) we get the linear system [2]:

$$\begin{cases} \partial_t \delta n = (\omega_b - \omega_d^* + \frac{\omega_{d0} a n^*}{(1+an^*)^2} - 2bn^{*2})\delta n - \gamma n^* \delta S \\ \partial_t \delta S = [c_s(\omega_d^* + 2bn^* - \frac{\omega_{d0} a n^*}{(1+an^*)^2}) - \delta_0 S^*]\delta n + (c_s \gamma n^* - \delta_s - \delta_0 n^*)\delta S \end{cases} \tag{2.5}$$

Which we can diagonalize to find the eigenvalues:
For the bare soil solution ($n^* = 0$):

$$\begin{cases} \lambda_+ = \omega_b - \omega_{d0} - \frac{\gamma P_s}{\delta_s} \\ \lambda_- = -\delta_s \end{cases} \tag{2.6}$$

So we find that $n^* = 0$ is an unstable point for $\omega_{d0} < \omega_d - \frac{\gamma P_s}{\delta_s}$ (it's eigenvalues have opposite sign) whilst $n^* = 0$ is a stable point otherwise (both eigenvalues become negative).
For $n^* \neq 0$ the eigenvalues have a much more complex expression that depends on all parameters and has to be solved numerically.

Bifurcations are points of special importance, as they often indicate the presence of a threshold between two different behaviours. The bifurcations that are relevant to us are:

1. **Saddle node bifurcation**: two fixed points merge and then disappear. We determined it by finding the zeros of the derivative of Eq. (2.4) respect to n^*.
2. **Transcritical bifurcation**: two fixed points collide and change stability. To find it we imposed $n^* = 0$ to Eq. (2.4), by which we got $\omega_{d0} = \omega_b - \gamma \frac{P_s}{\delta_s}$. Notice that, according to it's definition, this bifurcation marks the change in stability of $n^* = 0$ Eq. (2.6).
3. **Hopf bifurcation**: when the eigenvalues around a fixed point are complex conjugates, the system evolves in a spiral around said fixed point. If the real part of the eigenvalues is negative, the spiral converges into the fixed point (the fixed point is stable). However, if the real part of the eigenvalues is positive, the spiral converges into a stable orbit around the fixed point: if we start the evolution of the system outside the orbit it will spiral inward until it steadies in the orbit; however, if we give an initial condition inside the orbit, it will spiral outwards to the orbit, so the fixed point becomes unstable.
   This means the Hopf bifurcation can be determined by finding the zeros of the real part of both eigenvalues (when they are complex conjugates) [2].

2.2 Numerical methods

To find the fixed points and bifurcations, the equations have been solved numerically using methods like bisection or Newton-Raphson, using Fortran90 as the programming language.
To compute the evolution of the system we used a Runge-Kutta4 method to solve the coupled differential equations (2.1) and (2.2) (without spatial terms). A step of between $h = 0.1year$ and $h = 1year$ has been used, depending on the accuracy needed for the concrete regime, The initial conditions have been chosen based on streamline diagrams and the bifurcation diagrams obtained.

During the one month stay of the fellowship, we focused on studying the ODE system, while the spatial terms will be added in the future to compute the final, complete simulations. The idea is to run spatiotemporal simulations using a pseudo-spectral method to compare the evolution predicted by the model with images of the arcs seen in the Balearic coasts (Fig. 2) to see if there is correlation.

3 Results and discussion

To distinguish the different regimes in the theoretical model, we plotted the bifurcation diagram using Eq. (2.4) with the parameters used by Ruiz-Reynes et al, which were measured in the posidonia meadows of Pollença bay [1].
The parameters are: $\omega_b = 0.6y^{-1}$, $a = 15.0cm^2y^{-1}$, $b = 6.67cm^4y^{-1}$, $c_s = 30.6\mu Mcm^2$, $P_s = 1.13\mu My^{-1}$, $\delta_s = 0.036y^{-1}$, $\delta_0 = 0.06cm^2y^{-1}$, $\gamma = 6.54 \cdot 10^{-3}\mu M^{-1}y^{-1}$.
Plotting the corresponding eigenvalues gave us an idea of the stability of the fixed points and the types of bifurcations (Fig. 3).

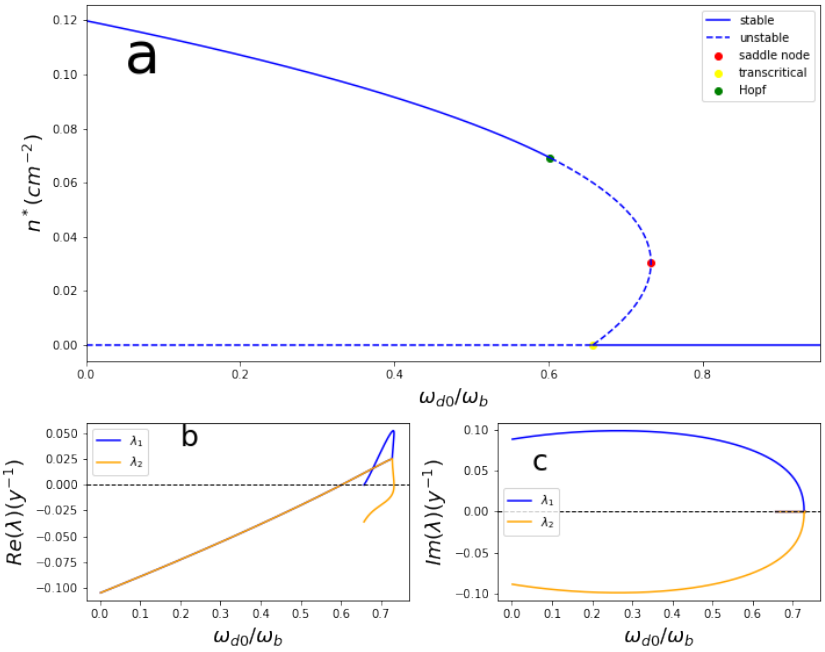

Figure 3: Panel a: bifurcation diagram showing the fixed points of the system (stationary values of vegetation density, n^*, as a function of mortality rate, ω_{d0}. The solid line accounts for the stable fixed points whilst the dotted line represents the unstable points. The green point marks a Hopf bifurcation; the red dot marks a saddle node bifurcation and the yellow point marks a transcritical bifurcation. Panel b: real part of the eigenvalues. Panel c: imaginary part of the eigenvalues.

In Fig. 3 we can see that, for mortality rate below the Hopf bifurcation there is only one stable point, with complex conjugate eigenvalues. That means the system will evolve towards the fixed point in a spiral (Fig. 4a). As a result, for low mortality we will have large, homogeneous meadows of vegetation.
For mortality values between the Hopf bifurcation and the saddle node bifurcation we can see that the real part of the eigenvalues becomes positive, meaning that the stable point becomes a stable orbit around said point (Fig. 4b). This would result in an oscillatory regime driven by the negative feedback between sulfides and vegetation: density would grow to a maximum point; then, the sulfide concentration would be high enough that plants would start to die, the vegetation density would decrease while sulfides dissipate until the sulfide concentration is low enough for vegetation to grow again.
The saddle node bifurcation can be identified where one of the eigenvalues becomes zero. For values of mortality above the saddle node plants can not grow and $n^* = 0$ becomes the only stable solution, meaning that vast plains without vegetation are the only possible outcome.
In the transcritical bifurcation, again we have that one of the eigenvalues disappears. This bifurcation marks a change in stability of the bare soil solution: for low mortality, $n^* = 0$ is unstable, meaning that vegetation will easily appear and grow to the stable value. For mortality above the transcritical solution, however, bistability appears. There are two possible stable solutions: the bare soil solution and the oscillatory regime.
The unstable branch below the saddle node bifurcation establishes which stable solution will be found: when above the unstable branch, we should find the stable oscillatory solution; whereas when below the unstable branch, the vegetation density would inevitably decline to zero.

The most interesting phenomenon that we can find in this system occurs when oscillations and bistability coincide. And only if the stable orbit of the oscillatory regime grows below the unstable branch. When this happens excitability emerges. In this case, given an initial condition around the upper fixed point, the system will grow spiraling away from the fixed point, hoping to reach the stable orbit. However, as it happens, it would cross the unstable solution and then decay inevitably to zero (Fig. 4c).
In this scenario, vegetation would grow until saturation, where it would start to decay. However, unlike the stable oscillatory solution, it would not reach the point where it can grow again, and so

it would disappear.
Recently, Dr. Ruiz-Reynés et al. have shown that this excitable dynamics are compatible with rings of posidonia that radially expand in space in the Balearic coast [1].

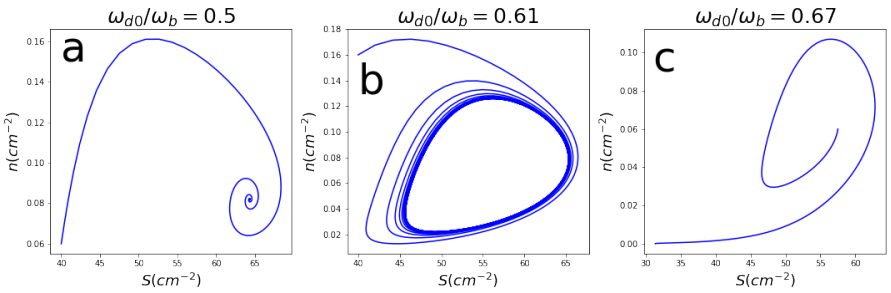

Figure 4: Evolution of the system for different values of ω_{d0}. We plotted the vegetation density, n, as a function of the sulfide concentration, S. Panel a: $\omega_{d0}/\omega_b = 0.5$, homogeneous regime. The systems evolves in an inward spiral towards the stable point, where it will remain constant. Panel b: $\omega_{d0}/\omega_b = 0.61$, oscillatory regime. The system stabilizes in an orbit around the now unstable point. Panel c: $\omega_{d0}/\omega_b = 0.67$, excitable regime. We can see how the system spirals away from the fixed point before decaying to zero.

For a more complete understanding of the system, we also studied how the diagram changes with the sensitivity to sulfides, γ, (Fig. 5).
We see that if γ is increased, the saddle node disappears (and so there is no more bistability nor excitability) and a second Hopf bifurcation appears. This means that the stable oscillations are confined in between both points.
If the sensitivity to sulfides is low, the oscillatory regime disappears and we have two stable points. We can also note that excitability happens in a very thin region of the diagram, for a very concrete set of parameters.

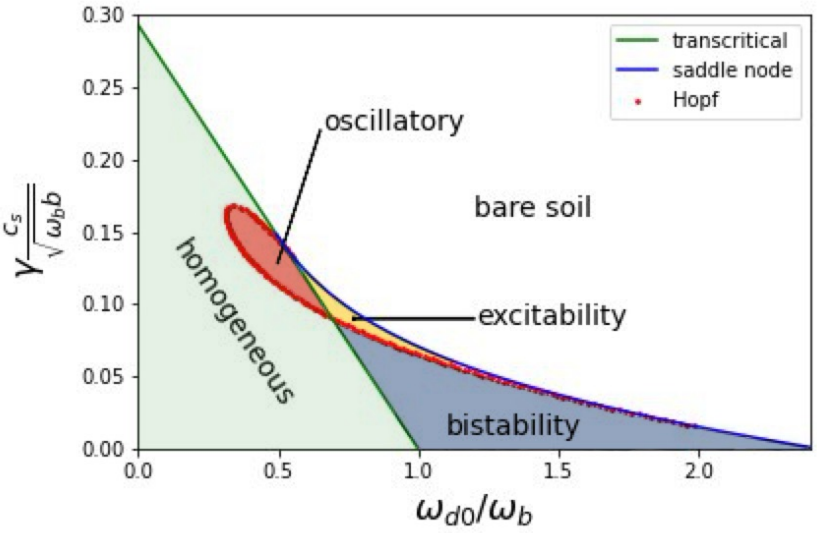

Figure 5: Phase diagram of the system with mortality, ω_{d0}, and sensitivity to sulides, γ, (dimensionless) as control parameters. The green line represents the transcritical bifurcation, the Hopf bifurcations are represented by the red line and the saddle node bifurcations by the blue line.
In the green shaded area, the only steady solution is an homogeneous meadow of vegetation. The red shaded area marks the oscillatory regime. For large mortality but low sensitivity, in the blue area, there are two stable solutions: the homogeneous meadow and the bare soil solution. In the white area vegetation can not grow due to the large mortality and sensitivity to sulfides, so bare soil is the only stable solution. The yellow area marks the excitable regime.

Seeing that the excitable regime of the model is compatible with the propagating pulses of posidonia observed in Pollença bay, we hoped that a similar mechanism would give an explanation for the opposite pattern: a pulse of bare soil propagating through a large meadow of posidonia.
So we searched a new set of parameters that would allow for a lower branch of fixed points from which the vegetation could oscillate around zero before shooting up to a stable point of larger density.
To do so, we varied all parameters until we found a second saddle node, then adjusted them to enlarge the bistability zone. The set of parameters found is:

$$\begin{cases} \omega_b = 1.0y^{-1} & a = 19.0cm^2y^{-1} \\ b = 1.6666667cm^4y^{-1} & c_s = 90\mu Mcm^2 \\ P_s = 0.4\mu My^{-1} & \delta_s = 0.036y^{-1} \\ \delta_0 = 3.2cm^2y^{-1} & \end{cases} \tag{3.1}$$

Notice that the most notable change is in δ_0, which has been augmented 50 times. This term corresponds to the elimination of sulfides due to vegetation presence.
The corresponding phase diagram is shown in Fig. 6

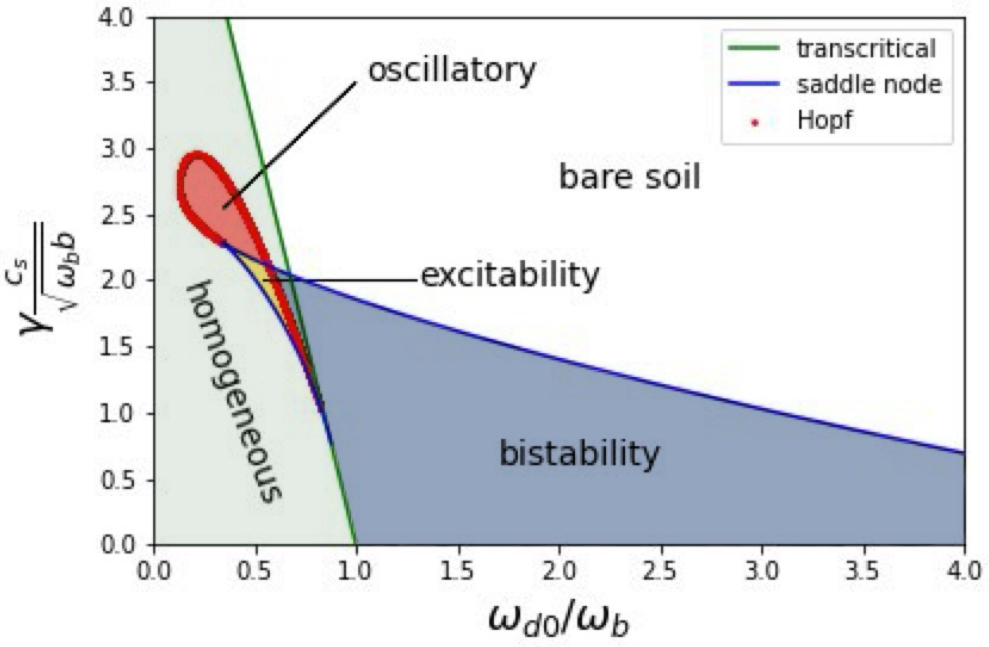

Figure 6: Phase diagram of the system for the newfound parameters. A second saddle node appears which merges with the transcritical bifurcation as sensitivity decreases. The excitable regime is now before the transcritical bifurcation, between the new saddle node bifurcation and the Hopf bifurcation.

Next, we study how the system behaves for different sensitivities.

For high values of γ, we see that the saddle nodes disappear, that means there will only be one stable solution for the system to reach. There is also a small region with two Hopf bifurcations. Between them, the fixed point becomes unstable and so a stable orbit solution appears (Fig. 7). However, the lack of bistability does not allow for excitability to happen.

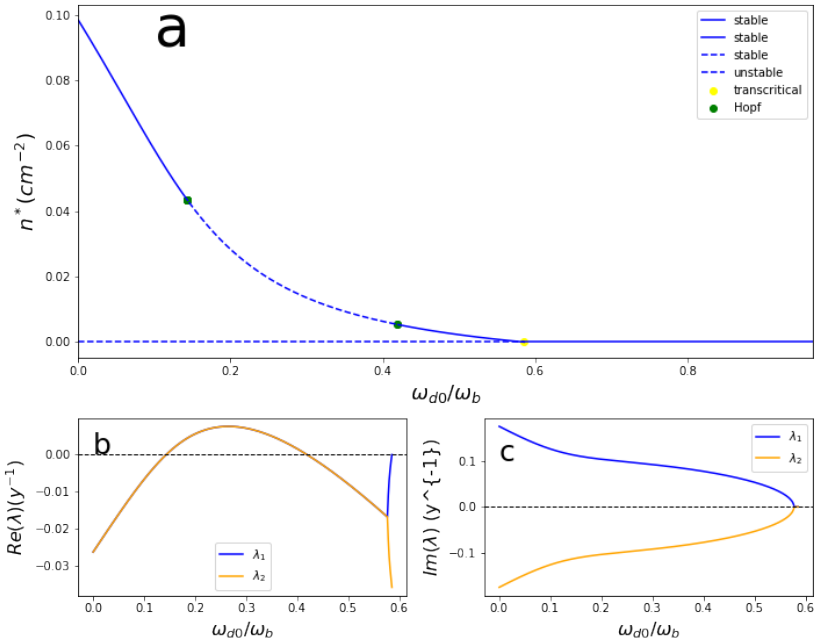

Figure 7: Panel a: bifurcation diagram for the newfound parameters with $\gamma\frac{c_s}{\omega_b b} = 2.6$. There is no bistability nor saddle node bifurcations, only an oscillatory regime of stable orbits between the two Hopf bifurcations. Panel b: real part of the eigenvalues. Panel c: imaginary part of the eigenvalues.

For low sensitivities, one saddle node remains (there still is bistability), while the other one merges with the transcritical bifurcation. We get a bifurcation diagram similar to the one found for the initial parameters, with the exception that now there are no Hopf bifurcations (Fig. 8). As a result there will not be stable orbits that could have resulted in excitability.

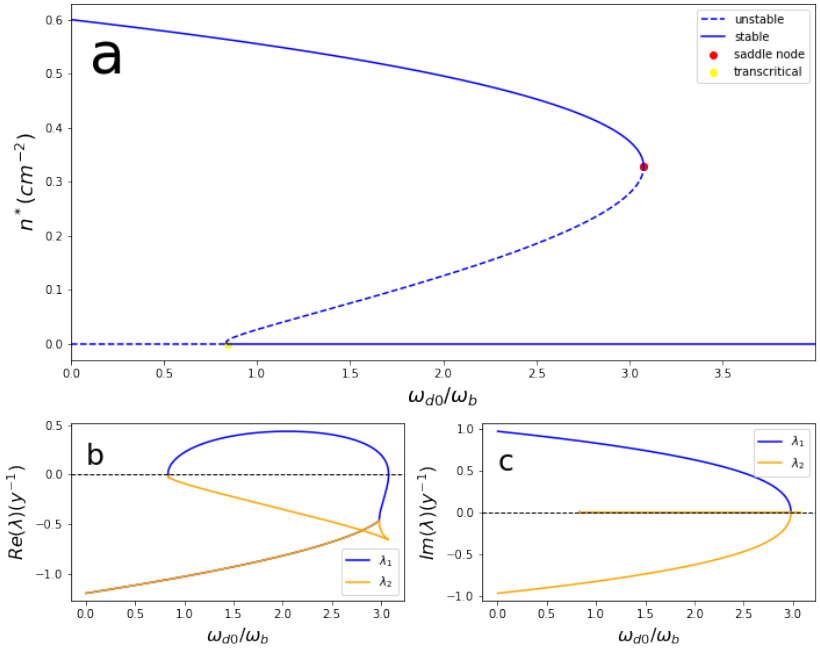

Figure 8: Panel a: bifurcation diagram for the newfound parameters with $\gamma\frac{c_s}{\omega_b b} = 1.0$. We can see that, although there is bistability, there are no Hopf bifurcations that could result in an oscillatory regime, meaning that excitability cannot happen. Panel b: real part of the eigenvalues. Panel c: imaginary part of the eigenvalues.

The most interesting regime of the phase diagram, however, is for $\gamma\frac{c_s}{\omega_b b} \in [1.5, 2.1]$, where the

bifurcation diagram shows multiple folds, as shown by Fig. 9. Comparing with the old parameters (Fig. 3) we see that the Hopf bifurcation has moved from the upper stable points to the new branch of lower fixed points. Notice also that before the oscillations appeared to the right of the Hopf bifurcation (positive eigenvalues), while now they can be found to its left.
In the zone between the lower saddle node and the Hopf bifurcation, we encounter an inverse excitability, which is what we where looking for. In this new regime, the oscillations appear below the unstable branch. So given an initial condition around the lower fixed point, it will spiral away from it looking for the stable orbit. However, it will grow over the unstable branch and then shoot up directly to the stable point above.
This should result in a patch of vegetation that decays momentarily to zero as it does a loop around the fixed point just before shooting up to the upper stable point in a spiral, as shown in Fig. 10.
This new behaviour should be a result of the now larger removal rate of sulfides, δ_0. As the patch of vegetation saturates and decays, sulfides now dissipate much quicker, allowing for a comeback of the vegetation where it can grow stronger.

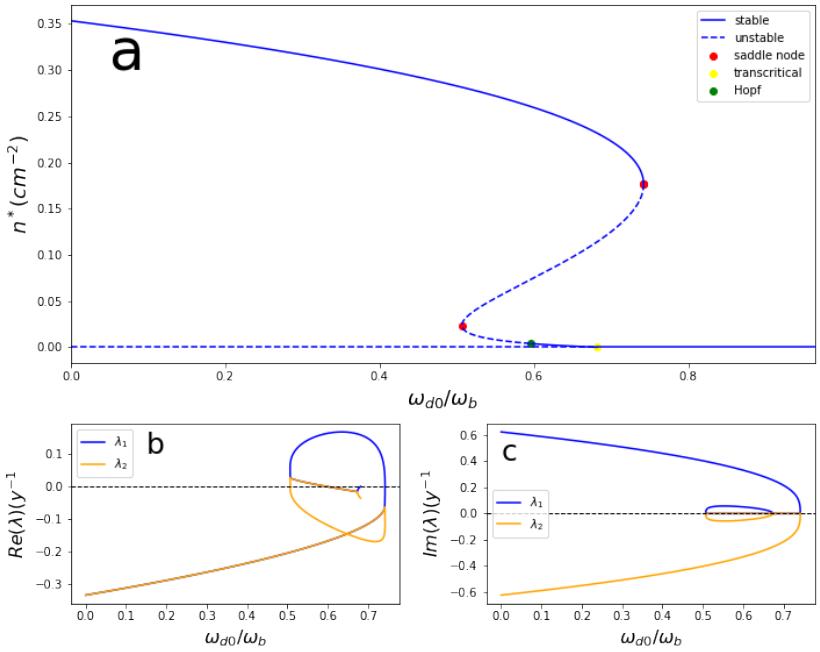

Figure 9: Panel a: bifurcation diagram for the newfound parameters with $\gamma\frac{c_s}{\omega_b b} = 2.0$. Panel b: real part of the eigenvalues. Panel c: imaginary part of the eigenvalues.

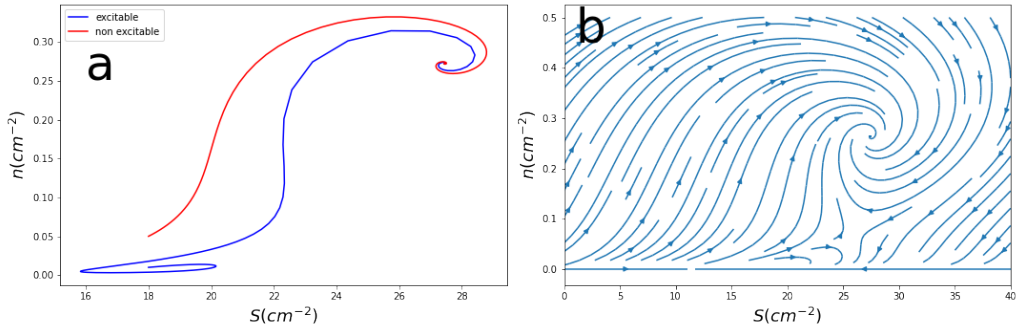

Figure 10: Panel a: evolution of the system for $\omega_{d0}/\omega_b = 0.585$. In blue the evolution followed in the excitable regime, with initial conditions below the unstable branch ($n_0 = 0.01cm^{-2}$ and $S_0 = 18cm^{-2}$), and in red the evolution of the system with initial conditions above the unstable branch ($n_0 = 0.05cm^{-2}$ and $S_0 = 18cm^{-2}$). Panel b: streamlines for $\omega_{d0}/\omega_b = 0.585$ where we can see the tendencies followed by the system in each region.

4 Conclusions

The theoretical results obtained in this work show a change in the behaviour of the coupled mechanics of sulfides and vegetation. As the removal rate of sulfides, δ_0, is largely augmented from the values that have shown compatibility with the propagating rings of posidonia [1], the dynamics of the system change slightly:
For large sensitivity to sulfides, the populated solution decays quickly as mortality raises, passing through an oscillatory regime (Fig 7).
For lower sensitivities, the stable points for the populated region do not exhibit oscillations anymore. However, for the appropriate sensitivity to sulfides, a new branch of stable oscillations appears for low densities and intermediate mortality. This region combines all necessary features for excitability to emerge: oscillations close to an unstable point and a bistable regime opposite to the one associated with the propagating rings: instead of a patch of vegetation that grows from an unpopulated area before decaying to zero again (which results in the propagating rings), the new regime that we have found should be consistent with a patch of vegetation initially populated that, after a small perturbation, decays to bare soil before reaching populated stability.
We hope that this newfound regime will be compatible with the propagating arcs of bare soil observed in the Balearic coasts.

In this work we have proven that the theoretical model studied exhibits a new kind of excitability for the right parameters.
The next step will be to add the spatial terms to the equations and run spatiotemporal simulations to see if the behaviour predicted by the model is compatible with the excitable arcs observed in nature.

Acknowledgments

First, I would like to thank my tutors, Drs. Damià Gomila and Daniel Ruiz-Reynés for their trust and guidance throughout all the project and their willingness to keep working on this project after the summer program ended.
I would also like to thank Dr. Manuel Matias, the coordinator of the program, for his confidence in me and his aid in any trouble I had during the program.
Finally, a special thanks to my colleagues of the fellowship with whom, throughout the stay, I built a good friendship and shared many interesting talks, both about our work and outside the research.

This work was supported by the SURF@IFISC fellowship.

References

[1] D Ruiz-Reynés, E Mayol, T Sintes , I E Hendriks, E Hernández-García, C M Duarte, N Marbà, and D Gomila. Self-organized sulfide-driven traveling pulses shape seagrass meadows (2023). https://doi.org/10.1073/pnas.2216024120

[2] Steven H Strogatz. Nonlinear dynamics and chaos (2015).

[3] N Juerguens. The Biological Underpinnings of Namib Desert Fairy Circles (2013). https://www.science.org/doi/abs/10.1126/science.1222999

[4] S Getzin et al. Discovery of fairy circles in Australia supports self-organization theory (2016). https://www.pnas.org/doi/abs/10.1073/pnas.1522130113

[5] D Ruiz-Reynés, D Gomila, T Sintes E Hernandez-Garcia, N Marbà, C M Duarte. Fairy circle landscapes under the sea (2017). https://www.science.org/doi/full/10.1126/sciadv.1603262

[6] V Pasqualini, C Pergent-Martini, G Pergent. Environmental impact identification along the Corsican coast (Mediterranean sea) using image processing (1999) https://www.sciencedirect.com/science/article/pii/S0304377099000480?casa_token=3SIXAxGSyJIAAAAA:AvN-6n5WdzblckOWMTMwHKko9FGc6R2s-Fyi65t-o2Yzu5XK0lnwoJgt6dHoUSX0Q0DID4fZcA